DISSERTAÇÃO

Non Gaussian Fluctuations
in the Cosmic Microwave Background Radiation

Valmir Pereira de Moraes Filho

Brasília, Março de 2019

UNIVERSIDADE DE BRASÍLIA

INSTITUTO DE FÍSICA

UNIVERSIDADE DE BRASÍLIA

Instituto de Física

DISSERTAÇÃO

Non Gaussian Fluctuations
in the Cosmic Microwave Background Radiation

Valmir Pereira de Moraes Filho

Dissertação submetida ao Instituto de Física

como requisito parcial para obtenção

do grau de Mestre em Física

Banca Examinadora

Prof. Dr. Ivan Soares Ferreira
Orientador e Presidente da Banca

———————————————————

Prof. Dr. Daniel Mueller
Avaliador, IF/UnB

———————————————————

Profa. Dra. Mariana Penna Lima Vitenti
Avaliador, Membro Externo, IF/UnB

———————————————————

FICHA CATALOGRÁFICA

REFERÊNCIA BIBLIOGRÁFICA

MORAES FILHO, V. (2019). *Non Gaussian Fluctuations in the Cosmic Microwave Background Radiation*. Dissertação, Instituto de Física, Universidade de Brasília, Brasília, DF, 82 p.

CESSÃO DE DIREITOS

Valmir Pereira de Moraes Filho

Instituto de Física - IFD

Universidade de Brasília (UnB)

Campus Darcy Ribeiro

CEP 70919-970 - Brasília - DF - Brasil

Agradecimentos

ABSTRACT

The temperature fluctuations of the Cosmic Microwave Background (CMB) validates the ΛCDM with incredible precision and has opened a door to the physics of the early universe. These perturbations are likely due to an inflationary phase that caused a rapid expansion to the universe, consequently generating tiny fluctuations in temperature of order 10^{-5}. Furthermore, these temperature fluctuations retain the information about the events that occurred during the CMB formation, about 380,000 years after the Big Bang. Recent analysis of the Planck data has shown small deviations from Gaussian condition. These deviations can reveal additional information from the very early times. The existence of a Non-Gaussian (NG) signal is predicted in a variety of classes of inflationary models, with different amplitudes. For this reason, finding a primordial NG signal is essential for discriminating which class of model was responsible for inflation. However, inflation is not the only source of non-Gaussianities, but it can also be produced by any sort of contamination in the CMB. In this context, this work aims at searching for NG signal in the data from the Planck satellite by using two statistical estimators. These are the momenta estimator that produced 3 statistical maps, and the Minkowski functionals that produced 3 plots for each parameter. We have performed a qualitative analysis of our results, which consisted on the comparison of the real to the simulated data. Our analysis has confirmed the presence of some residual contamination due to the large deviations from Gaussianity. Therefore, the detection of primordial NG requires data that is free of contamination.

Keywords: Cosmology – Cosmic Microwave Background – Observational Cosmology – Non-Gaussianity – Statistical Analysis: Momenta Estimator – Statistical Analysis: Minkowski Functionals.

FLUTUAÇÕES NÃO-GAUSSIANAS NA RADIAÇÃO CÓSMICA DE FUNDO EM MICRO-ONDAS

RESUMO

As flutuações de temperatura da Radiação Cósmica de Fundo (RCF) em micro-ondas validam o ΛCDM com incrível precisão, abrindo uma porta para a física do universo jovem. Essas perturbações provavelmente são decorrentes de uma fase inflacionária que causou uma rápida expansão do universo, gerando pequenas flutuações de temperatura de ordem 10^{-5}. Além disso, essas flutuações de temperatura retêm as informações sobre os eventos ocorridos durante a formação do CMB, cerca de 380.000 anos depois do Big Bang. As análises recentes dos dados de Planck mostram pequenos desvios da condição Gaussiana. Esses desvios podem revelar outras informações de tempos antes da RCF. A existência de um sinal Não-Gaussiano (NG) é prevista por uma variedade de classes de modelos inflacionários, com diferentes amplitudes. Então, se torna essencial encontrar NG primordial para descriminar qual classe de modelo foi responsável pela inflação. No entanto, a inflação não é a única fonte responsável por gerar não-Gaussianidades, que também pode ser produzida por qualquer tipo de contaminação no CMB. Neste contexto, este trabalho visa a busca de sinal NG nos dados do satélite Planck, utilizando estimadores estatísticos sensíveis. Estes estimadores são os de momento estatístico que produzem 3 mapas estatísticos e os funcionais de Minkowski que produzem gráficos para cada um dos 3 parâmetros. A nossa análise foi qualitativa em termos de comparação dos dados reais com os dados simulados. Nossa análise confirmou que ainda existe contaminação residual devido aos altos desvios de Gaussianidade. Portanto, a detecção de NG primordial requer dados livres de contaminação.

Palavras-Chave: Cosmologia – Radiação Cósmica de Fundo – Cosmologia Observacional – Não-Gaussianidade – Análises Estatísticas: Momento Estatísticas – Análises Estatísticas: Funcionais de Minkowski.

TABLE OF CONTENTS

LIST OF FIGURES

LIST OF SYMBOLS

Acronym

ACT	Atacama Cosmology Telescope
ACBAR	Arcminute Cosmology Bolometer Array Receiver
BBN	Big Bang Nucleossynthesis
BOOMERanG	Balloon Observations Of Milimetric Extragalactic Radiation AND Geophysics
COBE	COsmic Background Explorer
CMB	Cosmic Microwave Background
ESA	European Space Agency
HEALPix	Hierarchical Equal Area iso-Latitude Pixelization
NG	Non Gaussianity

1 INTRODUCTION

The Cosmic Microwave Background (CMB) radiation is the oldest observable that we have access to. It was formed about 380,000 year after the Big Bang. The universe had cooled to 3,000 K, which was perfect for electrons and protons to combine into Hydrogen atoms. At this time, the decoupling of matter and radiation happened, epoch known as Recombination era, which was when CMB photons were set free from its bound to electrons. This radiation could then travel through space freely until today (KOLB; TURNER, 1988). In 1965, Penzias and Wilson were the first to discover it (PENZIAS & WILSON, 1965). Since then, the CMB has been used to verify the standard cosmological model precision, a model that best describes our universe.

The standard cosmological model describes spacetime as being homogeneous and isotropic. According to it, the universe began from a hot and dense state and is very dynamic, which is constantly expanding and cooling. Furthermore, the success of the standard model is given for its predictions, among them a relic radiation from earlier times. The smoothness of temperature found across the sky in the CMB photons is proof of the universe's homogeneity and isotropy. In fact, the tiny temperature fluctuations imprinted in the CMB spectrum are evidence of earlier conditions. Many efforts were put into finding this relic radiation left from the Big Bang, and in 1965 Penzias and Wilson had the coincidence of finding it.

Since its discovery, many experiments have tested the accuracy of the standard model. These experiments were executed to analyze the CMB spectrum and the astrophysical contaminants around it as, for instance, Galactic emission (synchrotron, free-free and thermal dust) and extragalactic sources (HASLAM, 1981). As for these contaminants, they were a boost for the sky surveys that began the exploration of our the universe, which have been improving our knowledge of the processes that take place in our universe.

The satellite generation began with the launch of the Russian, Relikt (STRUKOV; SKULACHEV, 1984), and the American, COsmic Background Explorer (COBE)(SMOOT et al. 1990). Besides measuring the black body spectrum (Fig. 1.1) of the CMB with precision, the latter also mapped its distribution across the sky, measuring its temperature to be ($T_{CMB} = 2.725 \pm 0.010K$) and found temperature fluctuations of order 10^{-5} (SMOOT et al. 1992). The succeeding experiments motivations were to improve sensitivity and angular resolution for better observations.

The 90's was the beginning for the golden era of precision cosmology, after COBE found the temperature anisotropies in the CMB. In fact, many experiments were performed on balloons (e.g BOOMERanG (MACTAVISH et al. 2005)), from the ground, especially from the south pole (e.g ACBAR (REICHARDT et al. 2009)) as well as from the Atacama desert (e.g ACT (SIEVERS et al. 2013)), and from space, the WMAP (HINSHAW et al. 2013) and Planck (Planck Collaboration, 2018a) satellites. These experiments improved the precision of
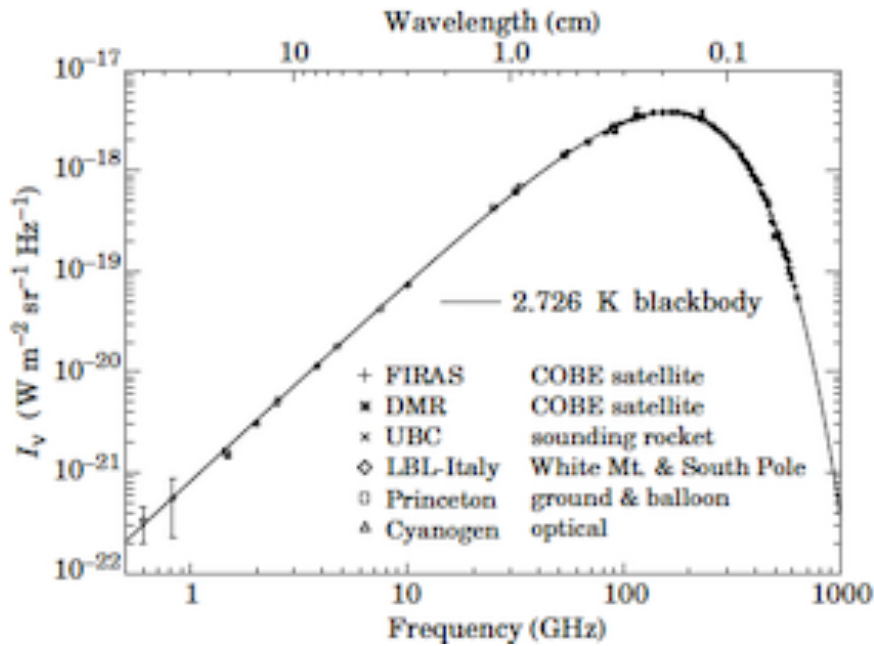
Figure 1.1: Precise measurement of the CMB black body spectrum done by FIRAS, an instrument of COBE satellite. SOURCE: SMOOT (1992)

temperature fluctuation measurements but also the slight polarization. Therefore, every CMB experiment has played its part towards completing the cosmological puzzle.

The Planck mission is the latest satellite experiment and devised to do a comprehensive study of the CMB radiation, and it ended up exploring way more (Planck Collaboration, 2009, 2013a, 2105a, 2018a). It was built with high resolution and sensitivity and a wide range of frequencies, 9 intervals from 30 to 853 GHz (Planck Collaboration, 2011a, 2011b). The incredible spectral coverage of the instruments allowed a better foreground identification and removal. As a result, Planck was able to produce an almost all clean full sky map (Fig. 1.2). Overall, there were 3 public releases and all the results are available at ESA's[1] website.

As a matter of fact, the importance of Planck and other experiments is that, besides improving our knowledge of the CMB power spectrum (temperature and polarizaion) it also improved our understanding of the physical processes that happen in our universe, which is a result of the increase of angular resolution and sensitivity of observations. Moreover, they have also been proving the amazingly concordance of the standar model (ΛCDM model) to observations. This model characterizes the geometry, dynamics and constituents of our universe. In particular, it says our universe is spatially flat (5×10^{-3} level), in constant expansion and composed of five basic cosmological constituents, which are dark matter that behaves just like vacuum energy or cosmological constant (Λ), cold dark matter (CDM, c), ordinary matter or baryons (b), CMB photons (γ) and neutrinos (ν) (Planck Collaboration, 2018f). Above all, the ΛCDM model can be described by 6 parameters and stands for an universe dominated by a cosmological constant and cold dark matter, see Fig. 1.3 for the updated constrains on the matter content.

---

[1]https://www.cosmos.esa.int/web/planck/publications
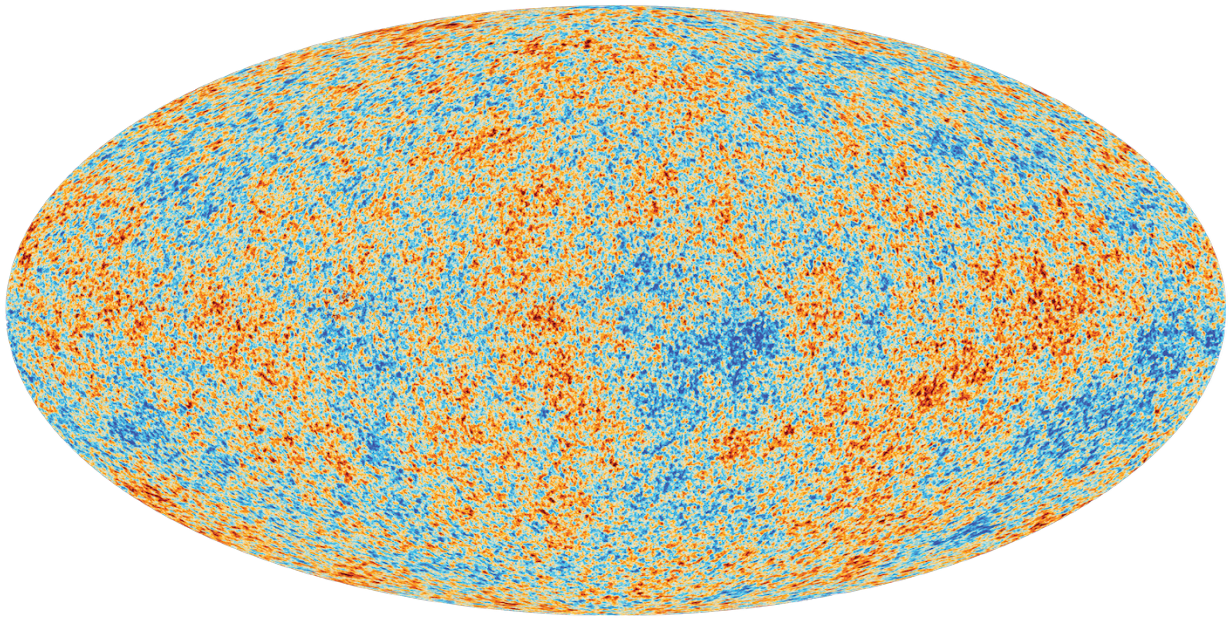
Figure 1.2: Temperature anisotropies in the CMB by Planck satellite. The map is based on the final public data release, published in July 2018. SOURCE: Planck mission / ESA webpage

Before Planck
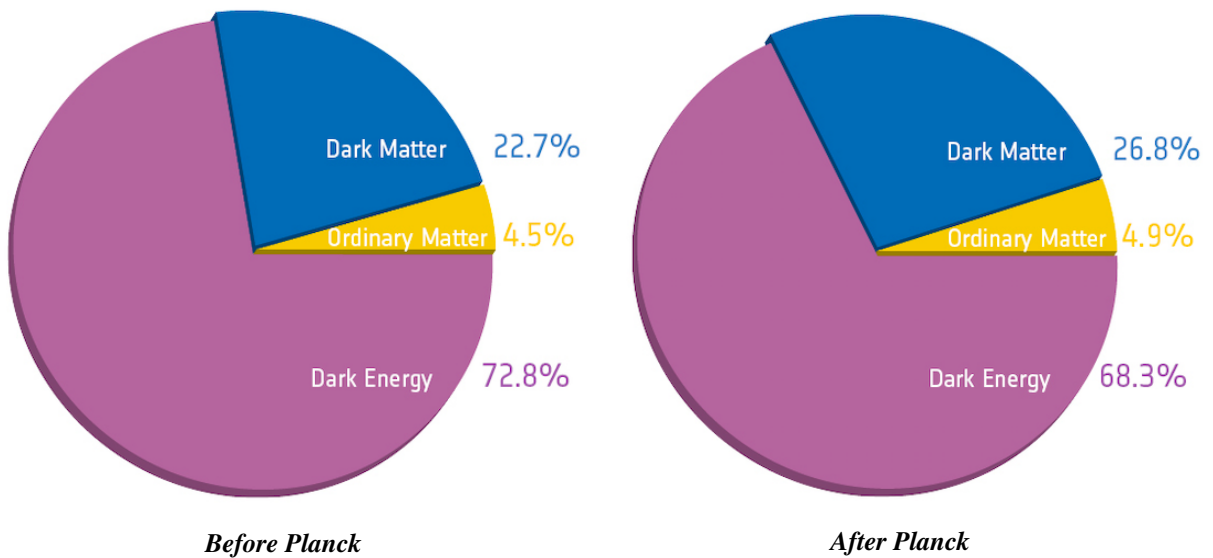
After Planck

Figure 1.3: Cosmic recipe for the universe constituents before and after Planck. On the *right*, the recipe was based on WMAP nine-year data release presented by HINSHAW et al (2013). And, on the *left*, the recipe was based on Planck's current understanding on the matter content of the universe (PLANCK COLABORATION, 2018f). SOURCE: PLANCK / ESA webpage

Even though the ΛCDM has an amazing prediction on the morphological structure and constituents of the universe and the relic radiation, there were problems to be solved as, for instance, the horizon and flatness problem, which according to the ΛCDM model, our universe could not be as homogeneous and flat as it is. Therefore in 1981, Guth proposed a solution to these problems, the solution being an inflationary phase in which the universe grew at an exponential rate (GUTH, 1981). Many others have explored the area in which the physics of inflation was developed. This phase would have happened before the standard cosmology, not as a replacement but as a complement theory (see more on Section 2.24). During the inflationary phase, the universe was subjected to quantum perturbations that overtime grew into local density perturbations to then turn into temperature fluctuations in the CMB.

The information obtained from the CMB comes from these temperature fluctuations. This information can be accessed by using the statistical properties of these anisotropies (HU, 1995). The power spectrum is responsible for holding all the information about the events that happened during recombination era. Nonetheless, it also carry information about perturbations from inflation (RIOTTO, 2002; BARTOLO, 2004; BAUMANN, 2009). These primordial perturbations are the key for understanding the initial conditions for CMB fluctuations.

Inflation is the leading theory for the origin of primordial perturbations. Also, there have been many ideas of how inflation came to be, which resulted in many classes of models that describe inflation. The different classes of models can result in similar predictions, which requires a more sensitive statistical tool (BARTOLO, 2004, 2010; KOMATSU, 2009; CHEN, 2010). The non-Gaussianity (NG) is a sensitive probe to primordial perturbations. Therefore, this tool can select or exclude the different classes of models.

However, NGs don't come exclusively from primordial perturbations. These could also be produced by astrophysical foregrounds (ICHIKI, 2014). The emission that comes from our Galaxy could mask the CMB signal. Most of galactic foregrounds are radiative processes that produce a signal in the frequency range of the CMB (BENNETT, 2003; KOGUT, 2007). This added to extragalactic foreground, i.e. emission from the background galaxies and clusters, contaminate the CMB sky. Their brightness contamination masks the CMB from detectors. Although, these foregrounds are not as understood as we would like, there is a (costly) way to mitigate this emission from our maps (BENNETT, 2003; KOGUT, 2007). The price for reducing the foreground emission is by cutting the sky in patches, which results in reduced sky observations.

The search for NGs has been intensified over the last years, the reason being that NGs have always been predicted, given the evidence of the concentration of objects in the celestial plane (ABRAMO, 2010). That is enough reason to look for deviations in the Gaussian condition. On that note, many estimators have been used to look and identify the origin of these deviations. One estimator that is widely used due to its incredible sensibility to primordial NG is the bispectrum, which is a 3-point correlation function (KOMATSU, 2002; BARTOLO, 2004). See more on Section 4.2. Another commonly used estimator is the Minkowski Functionals (NOVIKOV, 1999,

2000, 2006; KOMATSU, 2003; NOVAES, 2014a, 2014b). These have the special feature of not requiring any prior information about the map used, but only its morphological features. See more on Section 6.3. Lastly, there is the momenta estimator, which utilizes statistical information of the map to reconstruct a statistical map (BERNUI, 2009, 2010, 2012, 2014). See more on Section 6.2 . The resultant maps provide information on the variance, skewness and kurtosis of the map. Nonetheless, there are many other estimators that are able to detect NGs in the maps. However, we won't be able to talk about them in this work.

This present work has focused its attention into searching the non-Gaussian fluctuation in the CMB. The data produced by Planck satellite has gone through a cleaning process that removed the contamination of the CMB signal. Then, it should have slight deviations from Gaussianity due to primordial NG. We are going to test these maps for its presence. Our work comprised on applying two statistical estimators to the data. The results obtained were then compared to the Gaussian case in order to evaluate their deviation.

This dissertation is organized as follows: In Chapter 2, we review the basic aspects of the standard cosmological model and describe the inflationary phase, which is the seed perturbation for CMB anisotropies. In Chapter 3, we review the history of the CMB and describe the CMB power spectrum, its anisotropies and the polarization spectrum. In Chapter 4, we discuss the importance of finding primordial non-Gaussianity, its origin, and the statistical properties of the 3-point function, which is the primary estimator for non-Gaussinities. In Chapter 5, we study the systematics in the CMB data. In Chapter 6, we introduce the estimators we used in this work. In Chapter 7, we present our results and the discussion. In Chapter 8, we summarize with concluding remarks.

2 STANDARD COSMOLOGICAL MODEL

2.1 COSMOLOGY BACKGROUND

Let us begin by invoking the Copernican Principle saying "there are no special observers in the universe", which implies an isotropic space, one that is rotationally invariant or looks the same in every direction. This becomes more evident when looking at CMB's temperature uniformity across the universe. Moreover, a space which is isotropic everywhere is necessarily homogeneous, but the inverse isn't necessarily true. This brings us to the claim of homogeneous space, one that is translationally invariant or looks the same in every point (TRODDEN, 2004).

The universe can be approximated to a spatially homogeneous and isotropic three-dimensional space, which may expand as a function of time. It is necessarily the Friedmann-Robertson-Walker (FRW) metric for the spacetime of the universe (KOLB & TURNER, 1988; BAUMANN, 2009);

$$\mathrm{d}s^2 = \mathrm{d}t^2 - a^2(t)\left[\frac{\mathrm{d}r^2}{1 - kr^2} + r^2\big(\mathrm{d}\theta^2 + \sin^2(\theta)\,\mathrm{d}\phi^2\big)\right], \tag{2.1}$$

here, the scale factor $a(t)$ characterizes the relative size of a spacelike hypersurface (Σ) at different times. The curvature parameter k is +1 for positively curved Σ, 0 for flat Σ and -1 for negatively curved Σ. Eq. 2.1 makes use of comoving coordinates, $a(t)$ increases as the universe expands, but observers will keep their coordinates (r, θ, ϕ) fixed. The time coordinate t is referred to as cosmic time, or proper time, measured by a observer at rest in the comoving frame.

The casual structure of the universe is defined by the propagation of light in the FRW spacetime (2.1). So the coordinate system is the one that light travels, which is purely in the radial direction ($\theta = \phi = 0$). And, it is often convenient to express the metric in terms of a "conformal time" τ, defined by $d\tau = dt/a(t)$. The evolution is then determined by a two-dimensional line element (BAUMANN, 2009),

$$\mathrm{d}s^2 = a^2(\tau)\big[\mathrm{d}\tau^2 - \mathrm{d}\chi^2\big]. \tag{2.2}$$

Photons are massless particles and travel along a null geodesic, $ds^2 = 0$. Therefore, the maximum distance light could have propagated from an initial time t_i to some later time t is

$$\chi_{ph} = \tau - \tau_i = \int_t^{t_i} \frac{dt}{a(t)}\,, \qquad\qquad d_{prop} = a(t)\chi_{ph}. \tag{2.3}$$

which is called (comoving) particle horizon, and it is important because no information could have propagated further than χ_{ph} and still be in casual contact. The initial time t_i is taken as the "origin of the universe", $t_i \equiv 0$, defined by the initial singularity, $a(t_i \equiv 0) \equiv 0$. As for d_{prop}, it stands for the proper (or physical) particle horizon.

An important kinematic effect of the cosmological expansion is the *cosmological redshift*, so that a proper wavelength of a photon increases in time, proportionally to the scale factor $\lambda \propto a(t)$ (KINNEY, 2009). Since all photons redshift at the same rate, their energy loss due to the cosmological redshift is $h\nu \propto a^{-1}$. Therefore, their temperature also decreases as $T \propto a^{-1}$. For a photon emitted at time t_{em} and detected today at time t_0, the redshift is defined by,

$$(1 + z) \equiv \frac{a(t_0)}{a(t_{em})} = \frac{\lambda_0}{\lambda_{em}}. \tag{2.4}$$

The dynamics of an expanding universe is characterized by the evolution of its scale factor, which is determined by the Friedmann equation[1] (TRODDEN, 2004),

$$H^2 \equiv \left(\frac{\dot{a}}{a}\right)^2 = \frac{8\pi G}{3} \sum_i \rho_i - \frac{k}{a^2}, \tag{2.5}$$

where ρ_i is the energy density of the universe for the different species – matter, radiation and vacuum energy. The overdots denote derivatives with respect to physical time t. Moreover, the expansion rate of the universe is denoted by the *Hubble parameter*, $H \equiv \dot{a}/a$, and it varies as t^{-1}. The Hubble time (or Hubble radius) H^{-1} sets the time scale for the age of the universe and the size of the observable universe. It is also possible to define a *critical density* for a geometrically flat universe, $k = 0$, as $\rho_{crit} = 3H^2/8\pi G$. As for how fast (or slow) the expansion rate of the universe is, it is denoted a acceleration equation,

$$\frac{\ddot{a}}{a} = -\frac{4\pi G}{3} \sum_i (\rho_i + 3p_i). \tag{2.6}$$

Combining the Friedmann equation to the acceleration equation, we are left with the continuity equation, which governs the evolution of the energy density (BAUMANN, 2009; RIOTTO, 2002),

$$\dot{\rho} + 3H(\rho + p) = 0 . \tag{2.7}$$

The universe contains several non-interacting components that evolve separately and can dominate the total energy density contribution throughout time. Then, if the universe is dominated by relativistic matter, $p = \rho/3$, its energy density is $\rho_r \propto a^{-4}$ and $a \sim t^{1/2}$; as for non-relativistic matter, $p = 0$, with $\rho_m \propto a^{-3}$ and $a \sim t^{2/3}$; and for vacuum energy, $p = -\rho$, the energy density is constant and $a \propto exp(H/t)$, which describes a rather rapid expansion.

Consequently, when $\rho > \rho_{crit}$, the universe is positively curved and closed. As for $\rho < \rho_{crit}$, the universe is negatively curved and open (KINNEY, 2009). This ratio is expressed in terms of a density parameter, $\Omega \equiv \rho/\rho_{crit}$, which relates the total energy density in the universe to its local

---

[1]For this review the speed of light, Planck's constant and Boltzmann's constant were set to unity, $c = h = k_B = 1$, meaning that time and length have the same units which is the inverse of the unit of mass, energy or temperature

geometry by (BAUMANN, 2009; RIOTTO, 2002),

$$\Omega - 1 = \frac{k}{a^2 H^2} \ . \tag{2.8}$$

Therefore, the Friedmann equation (2.5) can be rewritten in terms of the density parameter (BAUMANN, 2012),

$$H^2 = H_0^2 \left[\Omega_{r,0} \left(\frac{a_0}{a} \right)^4 + \Omega_{m,0} \left(\frac{a_0}{a} \right)^3 + \Omega_{k,0} \left(\frac{a_0}{a} \right)^2 + \Omega_{\Lambda,0} \right], \tag{2.9}$$

here, the "curvature" density parameter was defined as $\Omega_{k,0} \equiv -k/(a_0 H_0)^2$. In literature, the subscript '0' is normally dropped, because it implies that observations are being taken *today*. And, this is also valid for the scale factor, which its value today is $a_0 = 1$,

$$\frac{H^2}{H_0^2} = \left[\Omega_r a^{-4} + \Omega_m a^{-3} + \Omega_k a^{-2} + \Omega_\Lambda \right]. \tag{2.10}$$

Over the past decades, many experiments have been done in order to accurately determine the basic features of our universe. These were in extremely concordance with the ΛCDM model. Nowadays, the observations find that the universe is spatially flat (Planck Collaboration, 2018a):

$$\Omega_k = -0.0096 \pm 0.0061 \tag{2.11}$$

and composed the different matter densities given by (Planck Collaboration, 2018b):

$$\Omega_b h^2 = 0.02237 \pm 0.00015;$$
$$\Omega_c h^2 = 0.12000 \pm 0.00120;$$
$$\Omega_\Lambda h^2 = 0.31070 \pm 0.00820. \tag{2.12}$$

These parameters are dimensionless, given that $h = H_0/100 \ kms^{-1}Mpc^{-1}$. And Hubble constant, H_0, is the present value of the expansion rate and its current value is $(67.36 \pm 0.54) \ kms^{-1}Mpc^{-1}$.

2.2 INFLATION

Until now, we have presented what is known in the standard model. Even though it has an outstanding success in predicting the physical processes presents in today's universe, there are still some blanks to be filled. These problems are mainly motivated to explain what sourced the initial conditions. Then, we need to present a new inflationary scenario.

In general the idea for inflation is a phase when the universe expanded exponentially at an accelerated rate, which requires a negative pressure and a constant energy density. This behaviour

is similar to the one of vacuum energy density. However, inflation must finite, or else radiation and matter would not be able to dominate total energy density at any point. Inflation provides a source for density fluctuations in the late universe, as well as for the rise of initial conditions.

2.2.1 Problems in Standard Cosmology

FLATNESS PROBLEM:

Spacetime in general relativity is dynamical, curving in response to the matter distribution in the universe. According to current observations, the universe is spatially flat, with $\Omega_0 \sim 1$ (2.11), which means it should be flat at all times. Let's return to Friedmann Equation rewritten as (BAUMANN, 2009; LIDDLE, 2000; RIOTTO, 2002)

$$\Omega(a) - 1 = \frac{k}{a^2 H^2}. \tag{2.13}$$

It shows a time dependence of the density parameter, $\Omega(a(t))$. In standard cosmology, the comoving Hubble radius, $(aH)^{-1}$ grows with time, and in eq. 2.13 the quantity $|\Omega(a) - 1|$ diverges with time. Therefore, any deviations from $\Omega = 1$ would result in a universe different from its near-flatness. More specifically, one finds that the deviation from flatness at the Big Bang Nucleosynthesis (BBN), during the GUT era and at the Planck scale respectively has to satisfy the following conditions (BAUMANN, 2009):

$$|\Omega(a_{BBN}) - 1| \leq \mathcal{O}(10^{-16});$$
$$|\Omega(a_{GUT}) - 1| \leq \mathcal{O}(10^{-55});$$
$$|\Omega(a_{pl}) - 1| \leq \mathcal{O}(10^{-61}).$$

thus, the values of Ω at earlier times would have to be incredibly near to 1, but not exactly 1, in order to obtain the present value of $\Omega \sim 1$ today. This requires an extreme fine-tuning to the values, which isn't compatible with observations.

HORIZON PROBLEM:

In the previous section, we have defined the (comoving) particle horizon, χ_{ph}, as the maximum distance a light ray can travel between the initial singularity, $t_i \equiv 0$, and a later time t (BAUMANN, 2009; RIOTTO, 2002),

$$\chi_{ph} \equiv \int_{t_i}^{t} \frac{dt'}{a(t')} = \int_{a_i}^{a} \frac{da}{Ha^2} = \int_{a_i}^{a} d\ln a \left(\frac{1}{Ha} \right), \tag{2.14}$$

here, the casual structure of spacetime can thus be related to the evolution of the comoving Hubble radius, $(aH)^{-1}$. For a universe dominated by a fluid with constant equation of state $w \equiv p/\rho$, then (BAUMANN, 2009),

$$(aH)^{-1} = H_0^{-1} a^{\frac{1}{2}(1+3w)}. \tag{2.15}$$
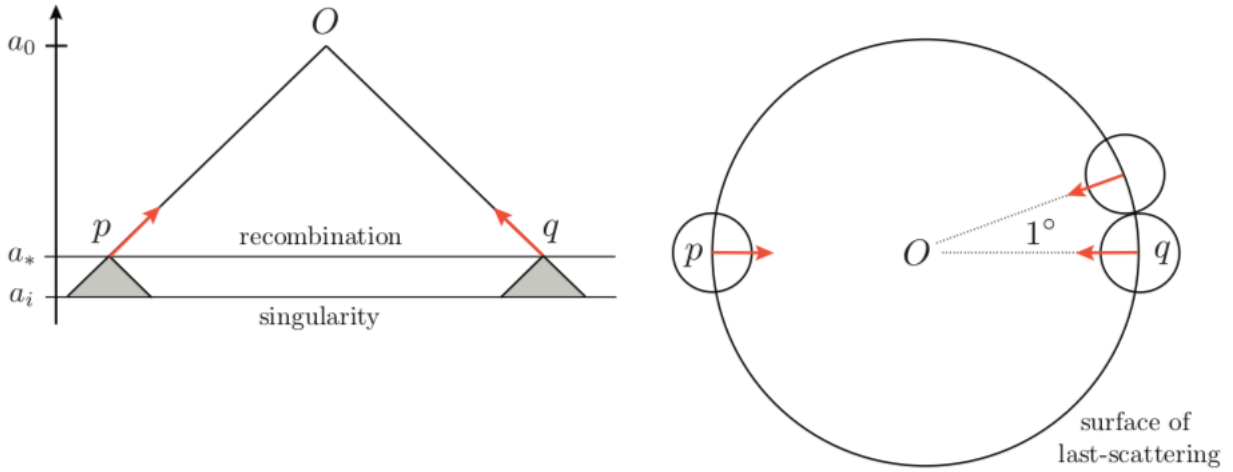
Figure 2.1: Illustration of the horizon problem. We can only observe events that are inside our past light cone. Any two points on the surface of last scattering that are separated by more than $1°$ apparently have never been in casual contact.
SOURCE: BAUMANN (2018)

The standard assumption is that the quantity $1 + 3w$ must be positive[2], which makes the comoving Hubble radius to increase as the universe expands. The integral in (2.14) shows that the (comoving) particle horizon receives its largest contribution from late times, since $a_i \equiv 0$ and $1 + 3w > 0$. In standard cosmology, the (comoving) particle horizon behaves similarly to the comoving Hubble radius (BAUMANN, 2009),

$$\chi_{ph} = \frac{2H_0^{-1}}{(1 + 3w)}\left[a^{\frac{1}{2}(1+3w)} - a_i^{\frac{1}{2}(1+3w)}\right] \equiv \tau - \tau_i. \tag{2.16}$$

However, the time elapsed from $t_i = 0$ to the time of CMB formation, t_{rec}, implying that most regions in the CMB have non-overlapping past light cones and hence were never in casual contact, which is not likely due to the near-homogeneity of the CMB photons. In this situation (Fig. 2.1), two points coming from the last scattering surface (recombination epoch) emitted sufficiently close to Big Bang singularity could not be in casual contact at that time. Therefore, it would be impossible for the CMB temperature to be isotropic and homogeneous, resulting in the horizon problem.

MONOPOLE PROBLEM:

The standard model predited the production of some stable "relics" at high temperatures. The magnetic monopoles were produced during the Grand Unified Theory (GUT) when $T \sim 10^{14} - 10^{15}$ GeV (LINDE, 2005). Because the horizon volume was extreme small then, they did not have enough time to be diluted in the very early universe.

Therefore, the universe would have been dominated by these relics because matter ($\propto a^{-3}$) dilutes slower than radiation ($\propto a^{-4}$) (BASSETT, 2006). Then they would have dominated the energy density of the universe today, thus contradicting the observations of light elements

---

[2]All matter sources have a positive strong energy condition (SEC)

abundance.

2.2.2 A Simple Solution

Both the horizon and flatness problems are directly connected to the increasing of the comoving Hubble radius. Therefore, a simple solution for them is to invert its increasing behaviour.

If the universe undergoes a period of accelerated expansion (inflation), $\ddot{a} > 0$, the integral in (2.14) becomes dominated by early times and the (comoving) particle horizon diverges in the past. The rapid expansion makes the Hubble parameter seem constant, which decreases the comoving Hubble radius $\mathrm{d}/\mathrm{d}t\, (aH)^{-1} < 0$. This behaviour implies that there was more time between the initial singularity and recombination, which solves the horizon problem (BAUMANN, 2009). It is important to note that $\tau = 0$ is not the initial singularity, but a transition from inflation to standard Big Bang evolution.

The flatness problem can be solved in the same manner. If the comoving Hubble radius decreases in (2.13), the universe will be driven towards flatness, $\Omega = 1$.

Now for the monopole problem, an accelerated expansion of the universe is able to dilute such unwanted "relics" because, during inflation, the density of monopoles drops exponentially, which makes their abundances drop to undetectable levels today.

From (2.6), the accelerated expansion requires negative pressure, $p < -\frac{1}{3}\rho$, which is neither matter or radiation. Therefore, the universe has to be dominated by something else.

2.2.3 Physics of Inflation

The models for inflation, in their majority, involve a phase during which the spacetime is a *Quasi de Sitter spacetime*[3] and a slowly rolling scalar dominating the universe.

The simplest model for inflation always involves a scalar field ϕ, the *inflaton* of unknown nature is time-dependent $\phi_0(\mathbf{x}, t)$, evolving in a potential energy density $V(\phi)$. For a homogeneous scalar field $\phi = \phi_0(t)$, its correspondent energy density and pressure are (BAUMANN, 2009; PETER, 2013):

$$\rho_\phi = \frac{\dot{\phi}^2}{2} + V(\phi), \qquad\qquad P_\phi = \frac{\dot{\phi}^2}{2} - V(\phi), \qquad\qquad (2.17)$$

here, the configuration $\dot{\phi}^2$ is the kinetic energy density. The evolution of the inflaton comes from inputting ρ_ϕ and P_ϕ in eqs. 2.5 and 2.7 become (LIDDLE, 2000; BAUMANN, 2009; PETER,

---

[3]A perfect de Sitter space,

$$ds^2 = dt^2 - \exp\{2Ht\}dx^2,$$

where $H = \partial_t \ln a = const$ grows exponentially with no end. On the other hand, inflation has to end in order for standard cosmology to take over.
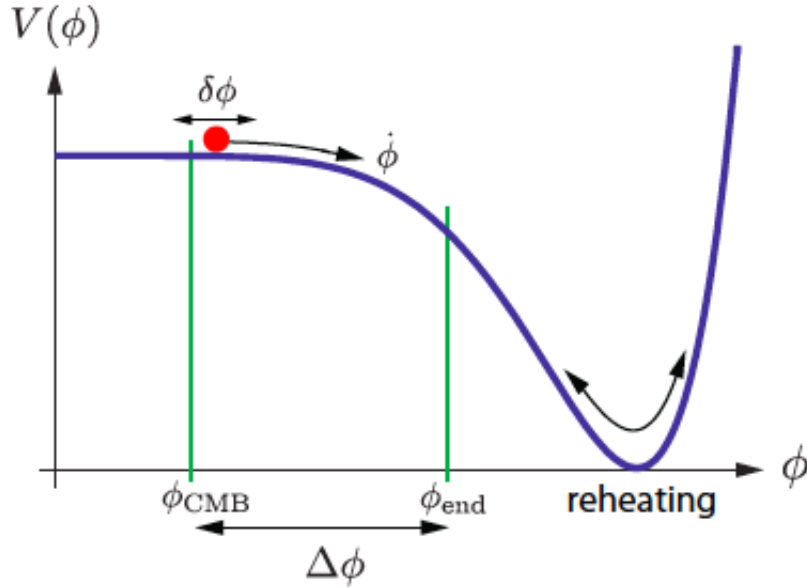
Figure 2.2: Schematics of the inflaton potential. Acceleration occurs on the region of the potential, which is sufficiently "flat", so kinetic energy is negligible. Inflation ends when kinetic energy has grown to become comparable to potential energy. At reheating, the energy density of inflation is converted into radiation.b
SOURCE: BAUMANN (2009)

2013):

$$H^2 = \frac{8\pi G}{3} \left(\frac{\dot{\phi}^2}{2} + V(\phi) \right); \tag{2.18}$$

$$\dot{H} = -4\pi G \dot{\phi}^2; \tag{2.19}$$

$$\ddot{\phi} + 3H\dot{\phi} + \frac{dV}{d\phi} = 0. \tag{2.20}$$

The first equation determines the Hubble parameter. The second equation is the continuity condition. The third equation describes the evolution of the inflaton.

The inflationary phase requires a negative pressure, $P_\phi < -\frac{1}{3}\rho_\phi$, which follows that the universe can enter its accelerated phase as soon as the potential energy dominates over the kinetic energy, $\dot{\phi}^2 \ll V$. This is the *first slow-roll* condition, for a sufficiently flat potential, the scalar field becomes negligible. So the scalar field slowly rolls down its potential, which is the reason for this period to be named *slow-roll*. Then, eq. 2.18 becomes,

$$H^2 \simeq \frac{8\pi G}{3} V(\phi). \tag{2.21}$$

And, to maintain the first slow-roll condition for a sufficient period of time, the acceleration of the field needs to be small, $\ddot{\phi} \ll 3H\dot{\phi}$, which is the *second slow-roll* condition. Thus, eq. 2.20 becomes,

$$3H\dot{\phi} \simeq -V'_\phi, \tag{2.22}$$

here V'_ϕ is the derivative of the potential with respect to the scalar. The two slow-roll conditions can be assessed by conditions on the shape of the inflaton potential (BAUMANN, 2018),

$$\varepsilon_V \equiv -\frac{\dot{H}}{H^2} \simeq \frac{M_{pl}^2}{2}\left(\frac{V'}{V}\right)^2 < 1, \qquad\qquad \eta_V \equiv M_{pl}^2\left|\frac{V''}{V}\right| < 1, \qquad (2.23)$$

where M_{pl} is the *reduced Planck mass*[4], $\varepsilon = \varepsilon_V$ and $\eta = -2\eta_V + 4\varepsilon_V$. These parameters are referred to as *(potential) slow-roll parameters*. Moreover, the use of parameters that depend only on spacetime geometry is that they are not restricted to the single scalar case. Inflation lasts until the first condition is broken, $\varepsilon_V = 1$. Although the inflaton $\phi_0(t)$ controls the amount of inflationary expansion still to occur, when it ends, it cannot control the time for the quantum fluctuations, $\delta\phi(t, \mathbf{x})$,

$$\phi(\mathbf{x}, t) = \phi_0(t) + \delta\phi(\mathbf{x}, t). \qquad (2.24)$$

These fluctuations are responsible for local differences in the time when inflation ends at δt. So the different patches of the universe all evolve classically but with different $\delta\phi$, thus leading to differences in the local densities after inflation ends. The total expansion due to inflation is measured in the amount of 'e-folds' between the beginning ϕ and the end of inflation ϕ_{end} as (CHEN, 2010; BAUMANN, 2018),

$$N_{total} = \zeta \approx aH\delta t \approx -aH\frac{\delta\phi}{\dot{\phi}_0}. \qquad (2.25)$$

Some terms were suppressed by the slow-roll parameters. This e-fold difference is the conserved quantity at horizon crossing, $k = aH$, until sometime after the Big Bang. It is the physical quantity measured, for example, from temperature anisotropies in the CMB, $\zeta \approx -5\Delta T/T$ (CHEN, 2010). The information about primordial inflation is then encoded in the statistical properties of this variable. The correspondent power spectrum for the comoving curvature perturbations,

$$\mathcal{P}_\zeta(k) = \left(\frac{aH}{2\pi}\right)^2\left(\frac{aH}{\dot{\phi}_0}\right)^2\Bigg|_{k=aH} = \frac{H^2}{8\pi^2 M_{pl}^2\varepsilon}\left(\frac{k}{k_*}\right)^{-2\varepsilon-\eta}, \qquad (2.26)$$

let k_* be the scale for the exit the horizon, so the spectrum index is defined as (BARTOLO, 2010; CHEN, 2010; BAUMANN, 2018),

$$n_s - 1 \equiv \frac{d\ln\mathcal{P}_\zeta}{d\ln k} = -2\varepsilon - \eta, \qquad (2.27)$$

here it was used the relation $d\ln k = Hdt$. The spectrum is scale invariant when $n_s = 1$. Recent data determined the spectral index to be $n_s = 0.9626 \pm 0.0057$ (Planck Collaboration, 2018c).

---

[4]

$$M_{pl}^2 = \frac{1}{8\pi G}$$
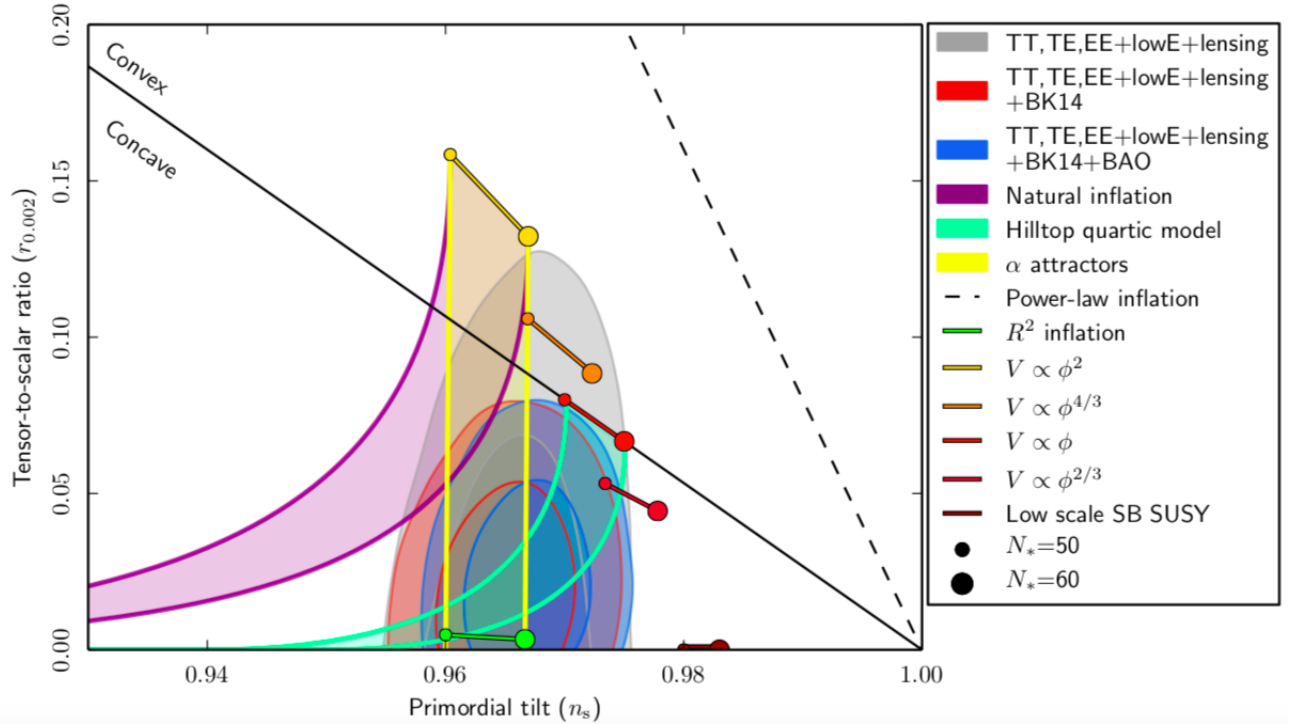
Figure 2.3: Constrains on n_s and $r_{0.002}$ in the different inflationary models predictions. N represents the amount of 'e-folds'. In *horizontal axis*, primordial tilt (n_s) is a direct measurement of the time dependance in the inflationary dynamics. In *vertical axis*, tensor-to-scalar ratio ($r_{0.002}$) is a direct measurement of the expansion rate H during inflation. The solid line represents the geometry of the potential, $V''(\phi)$, whether it is positive (convex) or concave (negative).
Source: Planck Collaboration (2018c)

This result requires a small η, which gives more e-folds of inflation.

These results are valid for a single field slow-roll inflation, which is the most explored model in literature (BAUMANN, 2009; CHEN, 2010; BARTOLO, 2004). In figure 2.3, it is possible to see the constrains for the different inflationary models.

2.3   A BRIEF THERMAL HISTORY

According to the ΛCDM model, the universe began very hot and dense. At that time, particle interactions were efficient enough to keep all different species in local equilibrium. And, after the discovery of the CMB, the standard cosmological model has been in extreme agreement with its findings. As predicted, the universe is constantly expanding and cooling, which gives rise to element formation, a relic radiation and Large-Scale Structures (LSS) seen in the sky today.

In the first 10^{-10} seconds of existence, the universe grew exponentially in a inflationary phase (GUTH, 1981), which was potential-dominated. The quantum fluctuations produced in these phase lead to local perturbations in density after inflation, which eventually grew into the LSS observed in the universe today (BAUMANN, 2009). After inflation was done, the universe

reheated and became dominated by radiation. The primordial plasma was almost in perfect local thermal equilibrium with very high temperature (KOLB & TURNER, 1988).

The early universe was filled with a primordial plasma, a period dominated by radiation ($t \lesssim 4 \times 10^{10} sec$), where particle interactions were efficient enough, so all species shared a common high temperature above 1 TeV. The thermal equilibrium was mainly maintained by the interaction of this radiation with matter by two processes: Compton scattering and thermal bremsstrahlung (GAWISER, 2000). After only a few seconds of existence the universe already had dropped its temperature to $\sim$ 10 MeV, and in around 3 minutes, the formation of the first light elements occurred, during Big Bang Nucleosynthesis (BBN). The standard model predicted the abundance of these elements observed in the extragalactic medium (KOLB & TURNER, 1988). Then, in around 1 eV ($10^{11}s$), the energy density in radiation balanced that in matter, called the matter-radiation equality.

Charged matter particles were strongly coupled to photons in the primordial plasma in the epoch of matter-radiation equality, and fluctuations in the density propagated as cosmic 'sound waves' (BAUMANN, 2009; DODELSON, 2003). These small perturbations have an important significance for the generation of large-scale structures and for the development of CMB anisotropies because they grow at different rates. Nearly 380,000 years (or 0.1 eV) after the Big Bang, the temperature dropped low enough ($\approx 3000K$) so electrons and protons could combine into the first neutral atoms, a process named *recombination* (BAUMANN, 2009; BAUMANN, 2018). Before that, the strongest coupling was between electrons and photons was via Compton scattering. Furthermore, after the severe drop in electron density, due to recombination, photons scattered for one last time at redshift 1100, and decoupled from the plasma, free streaming through the universe. Neither recombination and decoupling happened instantaneously. The photons we observe today are a snapshot of the early universe, and their tiny temperature fluctuations provide evidence for perturbations in the primordial matter density.

2.3.1 Perturbations in the Primordial Plasma

The recombination was an epoch which electrons and protons combined to form neutral hydrogen, which happened when the universe was $\sim$ 3000 K at a redshift about 1100. Before this event, the primordial plasma was composed of a tightly coupled photon-baryon fluid, where photons and protons were forced together by the strong coupling of free electrons via Thomson and Coulomb scattering (HU, 2002; TRISTRAM, 2007).

Matter tends to collapse due to gravity on regions where density is slightly higher, pushing baryons to overdense regions. However, because photons and baryons are strongly coupled, photons pressure tend to resist this collapse and push baryons outward, resulting in a succession of compression and rarefaction processes in the fluid, setting up acoustic oscillations. The fluid heats when in compression and cools when it expands, and photons also suffer redshift from climbing out of gravity potentials on the last scattering surface. This processes, also called primordial anisotropies, created the fluctuations in temperature observed today in the CMB.

3 COSMIC MICROWAVE BACKGROUND

3.1 CMB HISTORY

Discovered in 1965, the CMB radiation is the oldest light ever emitted (PENZIAS & WILSON, 1965). In the 1990s, COBE satellite verified the predictions towards the form of the CMB spectrum and mapped the temperature across the sky. As a result, it also revealed tiny deviation in the temperature at small scales. These anisotropies opened a door into the physics of the very early universe. In order to obtain better sensitivity and resolution from observation, other experiments were done and their findings helped our understanding of the early universe.

The standard model predicted there would be a relic background radiation from the hot early phase. The first detection of the CMB signal was done in 1965 by Arno Penzias and Robert Wilson. While they were investigating the radio transmission from communication satellites, they found an isotropic noise that was significantly larger than expected. The strange background noise that they could not account for had an antenna temperature of $3.5 \pm 1.0°$ K at 4080 Mc/s. The discovery of the CMB was essential to consolidate the Big Bang model, along with a wide comprehension of other of its predictions. And, the scientific community began looking for anisotropies in the CMB radiation. It was motivated by the assumption that structures in the universe (e.g galaxies, clusters) were formed from small primordial perturbations by gravitational instability. If they were right, then these fluctuations would have to be present in the CMB.

In November 1989, NASA launched its first satellite experiment COBE. It not only measured the CMB spectrum with incredible precision but it also found temperature fluctuations. The FIRAS (Far InfraRed Absolute Spectrophotometer) instrument was responsible for measuring the spectrum and the DMR (Differential Microwave Radiaometer) mapped the temperature across the sky in 3 frequencies (31.5, 53 and 90 GHz)(SMOOT, 1992). Subsequently, other experiments done on the ground and balloon-borne, continued to explore these anisotropies.

The Wilkinson Microwave Anisotropy Prove (WMAP) was the second satellite experiment launched in 2001 and operating for 9 years. It took data with radiometers on 5 frequencies from 22 to 93 GHz, all of which were also sensitive to polarization, with better resolution than COBE. These observations helped putting constrains in cosmological parameters as well as identifying contaminants, foregrounds (BENNETT et al. 2013; HINSHAW et al. 2013). All the data from WMAP observations are publicly available.

Nowadays, the data with best resolution was provided by Planck, launched in 2009 and terminated in 2018. The experiment operated at 9 frequencies (30 to 850 GHz), 7 of which were sensitive to polarization, and was composed of bolometers (the High Frequency Instrument, HFI) and radiometers (the Low Frequency Instrument, LFI). The instruments allowed Planck to
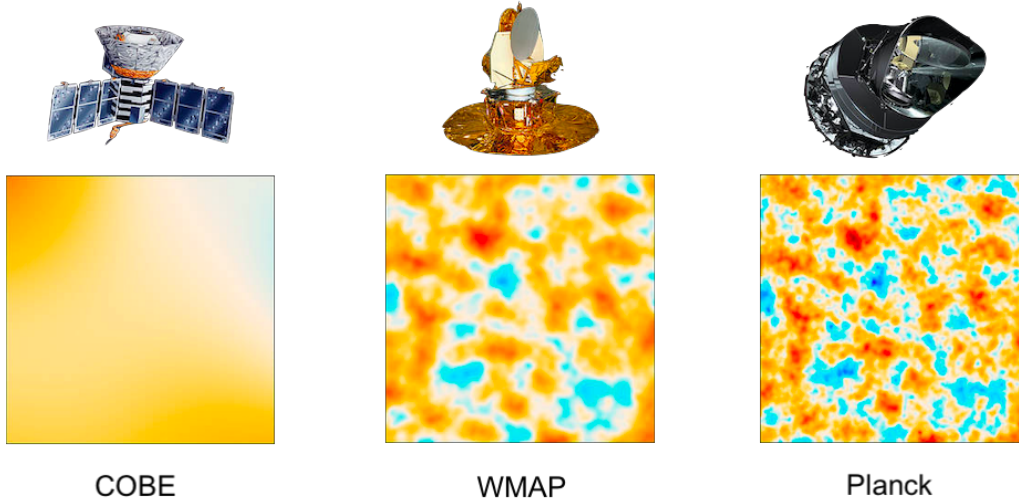
Figure 3.1: Evolution of satellite resolution. SOURCE: Planck / NASA webpage

measure the temperature fluctuations to only a few arc minutes apart (Planck Collaboration, 2014), which is the best precision achieved so far. This great spectral coverage allowed Planck to characterize and remove most of the foreground contamination.

3.2 CMB POWER SPECTRUM

The temperature fluctuations in the CMB can be expressed as (COLES; LUCCHIN, 2002):

$$\frac{\Delta T}{T}(\theta, \phi) = \frac{T(\theta, \phi) - T_0}{T_0}. \tag{3.1}$$

The temperature fluctuation is given as a fraction of the mean temperature T_0 as a function of angular position (θ, ϕ) on the sky. Furthermore, the angular dependence in (3.1) allows us to expand it in spherical harmonics,

$$\Theta(\hat{\mathbf{n}}) \equiv \frac{\Delta T}{T_0}(\hat{\mathbf{n}}) = \sum_{l=0}^{\infty} \sum_{m=-l}^{l} a_{T,lm} Y_{lm}(\hat{\mathbf{n}}), \tag{3.2}$$

where $\hat{\mathbf{n}}$ is the unit vector in the angular direction (θ, ϕ), and

$$a_{T,lm} = \int d\Omega Y_{lm}^*(\hat{\mathbf{n}}) \Theta(\hat{\mathbf{n}}). \tag{3.3}$$

The multipole l represents the inverse of the angular scale, where $l \sim 180°/\theta$. And $\hat{\mathbf{n}}$ is a unit vector pointing to an arbitrary direction. Due to statistical isotropy, the random variable of a_{lm}

for different l's and m's are not correlated, then (DURRER, 2008)

$$\langle a_{lm} \rangle = 0 \qquad\qquad \langle a_{l'm'}^* a_{lm} \rangle = \delta_{ll'} \delta_{mm'} C_l^{TT}, \qquad (3.4)$$

where δ_{ij} is the Kronecker symbol, and the variance C_l is the CMB power spectrum,

$$C_l^{TT} = \left\langle |a_{T,lm}|^2 \right\rangle . \qquad (3.5)$$

Writing an estimator $\hat{C}_l^{TT}$ of the power spectrum as (TRISTRAM, 2007),

$$\hat{C}_l^{TT} = \frac{1}{2l+1} \sum_{m=-l}^{l} |a_{T,lm} a_{T,lm}^*|. \qquad (3.6)$$

The power spectrum is the quantity that can be calculated and analyzed. If the CMB temperature fluctuations are Gaussian, as predicted by inflation, then the power spectrum contains all their statistical information (BERSANELLI, 2002; DURRER; 2008). As the CMB anisotropies are dominated by the scalar modes of inflation, the *transfer function* $\Theta_l(k)$ relates ζ and $\Theta(\hat{\mathbf{n}})$ in the following integral over momentum space (BAUMANN, 2009),

$$a_{T,lm} = 4\pi(-i)^l \int \frac{d^3k}{(2\pi)^3} \Theta_l(k) \zeta_{\vec{k}} Y_{lm}(\hat{k}), \qquad (3.7)$$

and the primordial power spectrum is then processed in the observed CMB power spectrum C_l^{TT} (BAUMANN, 2016),

$$C_l^{TT} = \frac{4\pi}{(2l+1)^2} \int d\ln k \underbrace{\mathcal{P}_\zeta(k)}_{Inflation} \underbrace{\Theta_l^2(k)}_{Anisotropies} . \qquad (3.8)$$

Now, consider two points at different directions and separated by an angle θ in the celestial sphere. If we are to measure their temperature fluctuations statistically, we must take the correlation function $C(\theta)$ of these points. The correlation function is a full realization of the power spectrum:

$$
\begin{aligned}
C(\theta) &= \langle \Theta(\hat{\mathbf{n}}) \Theta(\hat{\mathbf{n}}') \rangle_{\hat{\mathbf{n}} \cdot \hat{\mathbf{n}}' = \cos\theta} \\
&= \sum_l^\infty \left\langle a_{T,l'm'}^* a_{T,lm} \right\rangle \sum_{m=-l}^{l} Y_{lm}(\hat{\mathbf{n}}) Y_{l'm'}^*(\hat{\mathbf{n}}') \\
&= \sum_l^\infty C_l^{TT} \left(\frac{2l+1}{4\pi} \right) P_l(\cos\theta) \qquad\qquad (3.9) \\
&= \sum_l^\infty \left(\frac{2l+1}{4\pi} \right) \left[\frac{4\pi}{(2l+1)^2} \int d\ln k \mathcal{P}_\zeta(k) \Theta_l^2(k) \right] P_l(\cos\theta), \qquad (3.10)
\end{aligned}
$$

here the P_ls are the Legendre polynomials. It's important to notice that the plot of the power
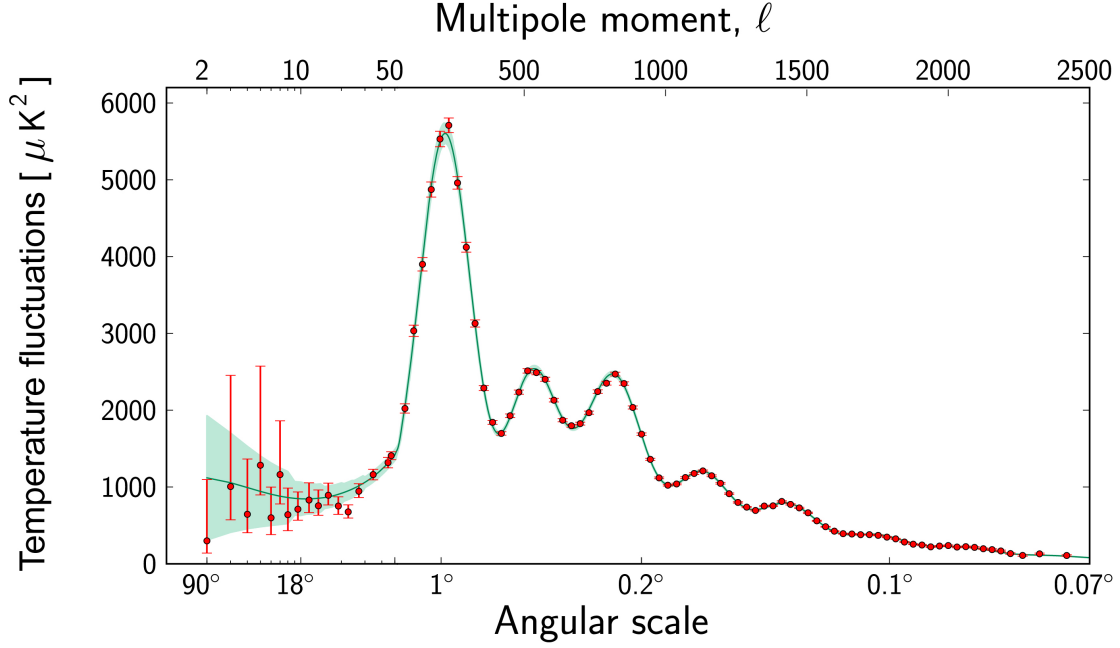
Figure 3.2: CMB power spectrum of the temperature fluctuations as measured by the Planck satellite. The red dots are measurements of the temperature fluctuations, Δ_l^{TT}, shown with error bars. The green curve is the best fit of the ΛCMD to Planck's data. The pale green area represents predictions of all variations of the standard model that best agree with the data. SOURCE: Planck / ESA webpage

spectrum is done by

$$\Delta_l^{TT} = \frac{l(l+1)}{2\pi} C_l^T \langle T \rangle^2 \,, \tag{3.11}$$

which is represented as a function of the multipole moment l, for $l \ll 1$; Δ_l^{TT} unit is μK^2. In figure 3.2, we have the best determination for the CMB power spectrum that came from Planck's observations. Moreover, all the power spectrum begin at $l = 2$ and show large errors at low multiples. That is because the power spectrum takes the average power in the multipole moment l for an assemble. Since we only got one universe to observe, we cannot average the monopole or dipole ($l = 0, 1$).

Cosmic Variance:

Because we only have one universe and one direction to observe it, we cannot compare its data to anything else. Therefore, all CMB measurements are connected with an uncertainty called cosmic variance.

The a_{lm} coefficients in equation 3.2 carry the same Gaussian properties as CMB temperature anisotropies. And each a_{lm} coefficient has $(2l + 1)$ degrees of freedom, which is, for a given l

there are $(2l + 1)$ m values. This fact induces an inevitable error, the cosmic variance

$$\sigma_l = \sqrt{\frac{\Delta \hat{C}_l}{C_l}} = \sqrt{\frac{2}{2l + 1}}. \tag{3.12}$$

Furthermore, a complete survey on the sky is not possible because foreground emission contaminates the CMB signal, which requires the use of masks that reduce the effective coverage. Then, the observed sky can be only a fraction of the whole sky, $f_{sky} < 1$ and its associated variance is

$$\sigma_l = \sqrt{\frac{2}{(2l + 1)f_{sky}}}. \tag{3.13}$$

3.3 UNCOVERING THE CMB SPECTRUM

The following discussion will take place in Fourier space (BAUMANN, 2016):

$$\Theta(\mathbf{k}, \mu, \tau) \equiv \sum_{l=0}^{\infty} (-i)^l \Theta_l(\tau, \mathbf{k}) P_l(\mu). \tag{3.14}$$

Given that the initial conditions of Θ depend on the wavevector $\mathbf{k}$, therefore on $\mu = \hat{\mathbf{k}}\hat{\mathbf{n}}$. And due to rotational symmetry, all $\Theta(\mathbf{k})$ for a given k obey the same equations. Let us consider a perfect photon-baryon fluid before recombination. The photon distribution will be isotropic in the electron rest frame, and not account for gravitational and baryon effects. The acoustic oscillations in this fluid obey the equation (HU, 2002; HU, 2008)

$$\dot{\Theta} = -\frac{1}{3}kv_\gamma,$$

which is the continuity equation in Fourier space. As well as the Euler equation, which represents the conservation of momentum in a fluid, $\dot{v}_\gamma = k\Theta$. Their combination yields a simple harmonic oscillator equation,

$$\ddot{\Theta} + c_s^2 k^2 \Theta = 0. \tag{3.15}$$

The sound speed for a radiation-dominated universe is $c_s^2 = \dot{p}_\gamma/\dot{\rho}_\gamma = 1/3$. Furthermore, the solution for the differential equation gives two initial conditions Θ_0 (monopole) and $\dot{\Theta}$ or v_γ (dipole),

$$\Theta(k, \tau) = \Theta_0 \cos(ks) + \frac{\dot{\Theta}}{kc_s} \sin(ks), \tag{3.16}$$

here $s = \int d\tau c_s$ is the sound horizon. These oscillations appear as standing waves for each Fourier mode in real space. They continue to oscillate until recombination. The oscillation patterns from that time became the **acoustic peaks** in the CMB spectrum. Considering the

adiabatic mode which starts with a finite density or temperature fluctuation and vanishing velocity perturbation,

$$\Theta(k, \tau_*) = \Theta_0 \cos(ks_*),\tag{3.17}$$

where τ_* is the recombination epoch. The modes caught at maxima or minima correspond to peaks in the power spectrum and obey the fundamental scale:

$$k_f = \frac{\pi}{s_*}; \qquad\qquad k_n = nk_f; \qquad\qquad n = 1, 2, 3...\tag{3.18}$$

The spatial inhomogeneities in the CMB temperature of wavelength λ appear as angular anisotropies of scale $\theta_f = \lambda_f/D_f$ and $l_f = k_f D_f$. These acoustic features appeared at recombination, when the universe was matter-dominated $\tau \propto a^{1/2}$. Here, the comoving angular distance, $D_f = \chi_{ph} = \tau_0 - \tau_* \approx \tau_0$, is simply the horizon distance, and $k_f = \sqrt{3}\pi/\tau_*$. Therefore, they appear at $\theta_f \approx 1/30 \approx 2°$ or $l_f = l_1 \approx 200$ in the CMB spectrum.

Acoustic motion of the photon-baryon fluid also produces a Doppler shift in the radiation that appears to the observer as a temperature anisotropy (HU, 2008). In radiation-dominated universe, the effect is of equal amplitude and $\pi/2$ out of phase, i.e. extrema of temperature are turning points of velocity (HU, 1997),

$$\Theta^2(k) = \Theta(0)[\cos^2(ks) + \sin^2(ks)] = \Theta^2(0),$$

meaning that there are not preferred k-modes at harmonics, and a scale invariant temperature would lead to a scale invariant spatial power spectrum at recombination. However, due to angular dependence, the Doppler contribution is overpowered by local temperature at recombination.

The fluctuation in the inflationary phase got turned into the temperature fluctuations by gravity influence. The Newtonian potential and spatial curvature provides a gravitational force that alters the acoustic oscillations. The Euler equation gains an additional $k\Psi$ due to gradient of the potential. In other words, gravity provides a competition between pressure gradients $k\Theta$ and potential gradients $k\Psi$, which affects the oscillations. Moreover, the continuity equation is also affected by gravity, gaining a $-\dot{\Phi}$ term on the right-hand side. Thus, the oscillator equation becomes (HU, 2002; HU, 2008),

$$\ddot{\Theta} + c_s^2 k^2 \Theta = -\frac{k^2}{3}\Psi - \ddot{\Phi}.\tag{3.19}$$

In the absence of baryons – radiation-dominated universe, the sound speed $c_s^2 = 1/3$, and the gravitational potential $\Psi \approx -\Phi$. The solution for this differential equation is the same as (3.16)

$$[\Theta + \Psi](k, \tau_*) = [\Theta + \Psi](0)\cos(ks).\tag{3.20}$$

The zero-point of this oscillator is where pressure and gravity are balanced $\Theta + \Psi = 0$. In this case, acoustic oscillations would rise by gravitational infall and compression of the fluid inside

the potential wells, increasing their energy and number density over gravitational blueshift. Then, naturally, after decoupling photons have to climb out of the potential wells, thus losing energy and suffering a gravitational redshift of Φ. The gravitational potential is a time perturbation, $\Psi = \delta t / t$, in a matter-dominated universe $t \propto a^{3/2}$. Since CMB temperature cools as a^{-1}, then

$$\Theta = -\frac{\delta a}{a} = -\frac{2}{3}\frac{\delta t}{t} = -\frac{2}{3}\Psi,$$

when it is applied to the effective temperature $\Theta + \Psi$, it yields $\Psi/3$, which is the Sachs-Wolfe (SW) effect (HU, 2008). This results in overdense regions where Ψ is negative and corresponds to cold spots in the effective temperature observed on the sky (SACHS & WOLFE, 1967). So, when the gravitational potential is negative, the effective temperature is also negative, and the fluid is rarefied in the wells. As gravity compresses the fluid and pressure resists, rarefaction becomes compression and then rarefaction again. The *first peak* corresponds to the mode caught at its first compression. The *second peak* is roughly half the wavelength that corresponds to the mode caught after a full cycle of compression and rarefaction.

The effect of baryons on the oscillations only appear effectively after recombination. They are easy to include in the evolution equations (3.19), because they contribute in the inertial and gravitational mass of the fluid. Therefore, it decreases sound speed and changes the balance of pressure and gravity. Now, gravitational infall leads to greater compression of the fluid in a potential well, which is a further displacement of the oscillation zero-point (HU, 1997). The redshift is unaffected by baryons. This relative shift is maintained after last-scattering which enhances all peaks from compression over those from rarefaction. The solution for oscillations becomes

$$[\Theta + (1+R)\Psi](k, \tau_*) = \frac{1}{3}\Psi(0)(1+3R)\cos(ks), \tag{3.21}$$

here R is the photon-baryon momentum density ratio, $R = (p_b + \rho_b)/(p_\gamma + \rho_\gamma)$. After baryon loading, the amplitude of oscillations increase by a factor of $1 + 3R$. Then, the shift in the equilibrium point reflects on peaks of different amplitudes, and the baryons enhance the compressional peaks (minima) over rarefaction (maxima), i.e. odd peaks are higher than even peaks. Finally, the lowering of the sound speed, $c_s^2 = \dot{p_\gamma} + \dot{p_b}/\dot{\rho_\gamma} + \dot{\rho_b} = 1/3(1+R)$, decreases sound horizon. However, this effect is smaller since R is growing in time. An additional effect arises due to the adiabatic damping of an oscillator with a time-variable mass. Since the energy to frequency ratio of an oscillator is an adiabatic invariant, the amplitudes must decay as $(1+R)^{-4}$ as R changes.

The gravitational potential changes with time and decays with expansion. So, when radiation dominates the energy density, the pressure gradient becomes more important than gravity on scales smaller than sound horizon. The decay of the gravitational potential acts as a driving force on the acoustic oscillations. This leaves the fluid maximally compressed with no gravitational potential to fight as it turns around, and the net effect is doubled because the redshift from Φ also goes away (HU, 2008). The peaks that began oscillating at radiation epoch have their amplitudes
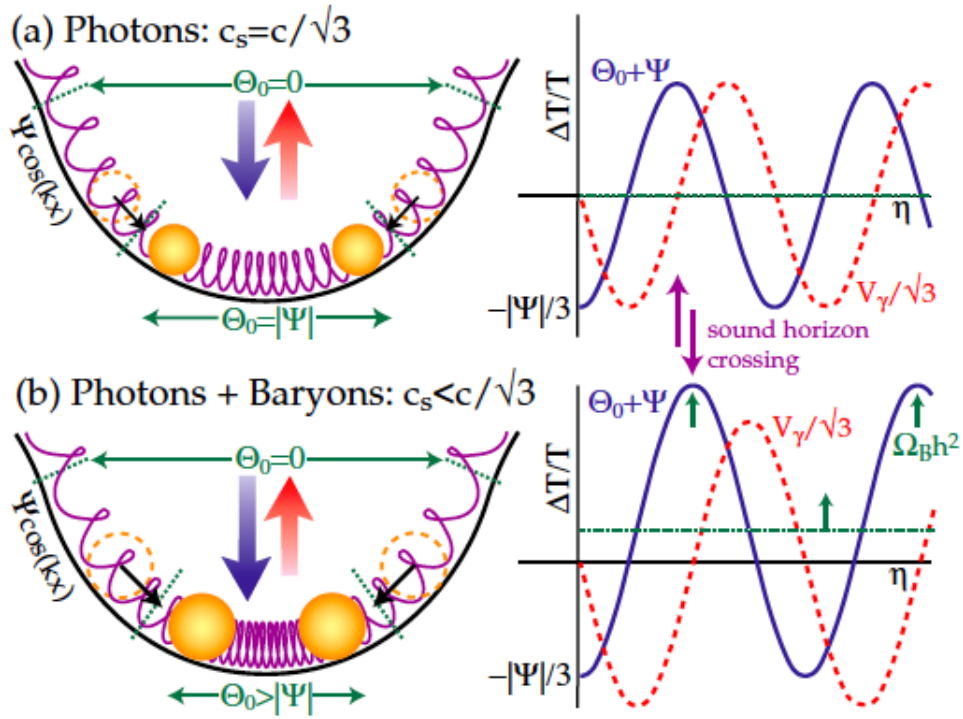
Figure 3.3: Acoustic Oscillations. (a) Photon-dominated system. (b) Photon-baryon system. Source: HU (1997)

enhanced (HU, 2008), so

$$[\Theta + \Psi](k, \tau) = [\Theta + \Psi](0) + \Delta\Theta + \Delta\Phi \tag{3.22}$$

$$= \frac{1}{3}\Psi - 2\Psi = \frac{5}{3}\Psi. \tag{3.23}$$

This estimate enhances the SW effect in $5\times$. In fact, this is generally called the integrated Sachs-Wolfe (ISW) effect. It is the gravitational redshifts from the time dependent potential that continued to generate fluctuations between last scattering and the present in the same manner which adds another uncertainty to the first peak location (HU, 1996).

However, the photon-baryon fluid has imperfections[1] which are associated with the Compton mean free path in the baryons, λ_C. At diffusion scale, $\lambda_D = \sqrt{\tau\lambda_C}$, photons can random walk through baryons from hot to cold spots, which causes a decrease in the oscillations amplitude beyond the third peak, $l \sim 1000$ (SILK, 1968; HU, 2008). At last scattering, the free electrons density decreases because of recombination and so does the electron ionization fraction, but photon's mean free path increases. Therefore, the damping length scales approximately as $(\Omega_b h^2)^{-1/4}$ (HU, 2002).

---

[1]On scales where $\lambda \gg \lambda_C$ photons are tightly coupled to electrons by Thompson scattering which in turn are tightly coupled to baryons by Compton interactions.
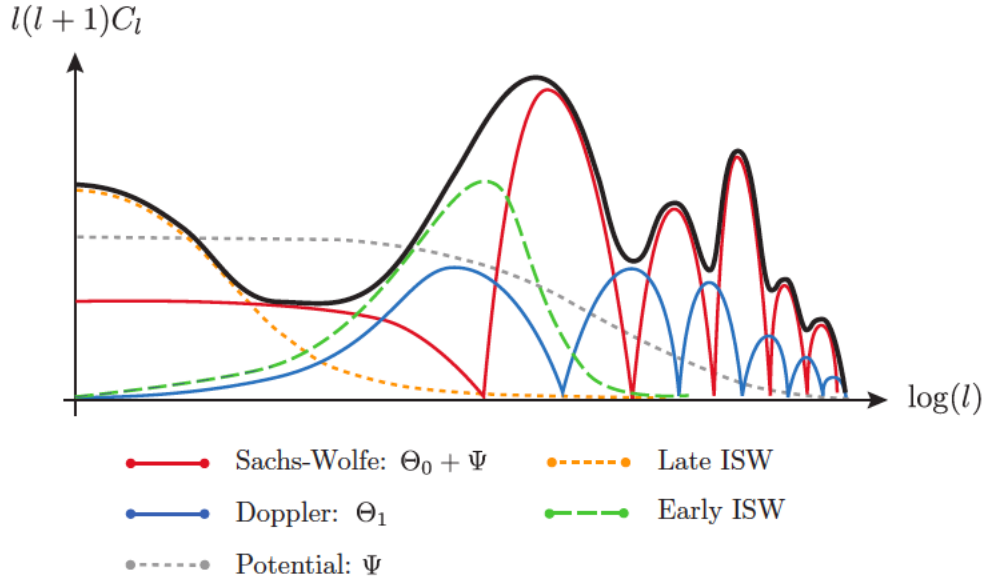
Figure 3.4: Different contributions to CMB power spectrum. Source: BAUMANN (2016)

3.3.1 From Acoustic Oscillations to Anisotropies

The discussion so far has been done in the qualitative aspects of the acoustic peaks of the power spectra. From now on, we are going to stress the sources of anisotropies and their projections into multipole moments. The acoustic oscillations modes are a more complete realization of the temperature fluctuations transfer function, in (3.8). Then the transfer function $\Theta_l(k)$ can be written as (HU, 2002; BAUMANN)

$$\Theta_l(k) = (\Theta_0 + \Psi)_* j_l(k[\tau_0 - \tau_*]) + (v_b)_* j_l^{'}(k[\tau_0 - \tau_*]) + \int_{\tau_*}^{\tau_0} d\tau(\dot{\Psi} + \dot{\Phi}) j_l(k[\tau_0 - \tau]), \quad (3.24)$$

where $(f)_* \equiv f(\tau_*, \mathbf{k})/\zeta(\mathbf{k})$ was used to simplify the notation and in a tight-coupling limit $v_\gamma \approx v_b$. Now, applying the transfer function (3.24) to the power spectra in (3.8) results in six terms: the power spectrum of the SW term, C_l^{SW}, that of the Doppler term, C_l^D, that of the ISW, C_l^{SW} and three cross spectra.

In (3.24), the spherical Bessel functions $j_l(x)$ and $j_l^{'}(x)$, for large values of l, are very peaked near $x \approx l$. So they act like delta functions in the integral (3.8), which means modes are $k(\tau_0 - \tau_*) \simeq l$. Therefore, the contribution from each inhomogeneity in the primordial fluid is plotted in figure 3.4 and their characteristics can be seen in the temperature (total intensity) power spectrum.

3.4 POLARIZATION SPECTRUM

The polarization of the CMB is described by the electromagnetic field $\vec{\epsilon}$, which is orthogonal to its direction of propagation $\vec{k}$. A general radiation is an incoherent superposition of waves with

the same wave vector $\vec{k}$ and different frequencies. Choosing two basis vectors $\hat{x}$ and $\hat{y}$ orthogonal to $\vec{k}$, all statistical information is encoded in the 'coherence matrix' $\mathbf{C}$ (MEMARI, 2007):

$$\mathbf{C} = \begin{pmatrix} \langle |\vec{\epsilon_x}|^2 \rangle & \langle \vec{\epsilon_x}\vec{\epsilon_y^*} \rangle \\ \langle \vec{\epsilon_x^*}\vec{\epsilon_y} \rangle & \langle |\vec{\epsilon_y}|^2 \rangle \end{pmatrix} = \frac{1}{2} \begin{pmatrix} I+Q & U+iV \\ U+iV & I+Q \end{pmatrix}, \tag{3.25}$$

where the averages are over a range of frequencies. The quantities I, Q, U and V are the *Stokes parameters*. The I parameter measures the intensity of radiation, the other parameters describe the polarization state: Q and U parameters measure the linear polarization, and V is the circular polarization parameter, which is typically equal to zero in CMB polarization. There is a property that allows the decomposition of the observed radiation (I, Q, U, V), which is $I^2 \geq Q^2 + U^2 + V^2$. The observed radiation can be divided into two components: an unpolarized $(I - (Q^2 + U^2 + V^2)^{-1/2}, 0, 0, 0)$ and an elliptically polarized $((Q^2 + U^2 + V^2)^{-1/2}, Q, U, V)$.

Polarization has an orientation and magnitude. its orientation relative to x-axis is

$$\chi = \frac{1}{2} \tan^{-1} \frac{U}{Q}$$

and the polarization amplitude is

$$\vec{P} = \sqrt{(Q^2 + U^2)}\hat{\chi}.$$

The parameter I is invariant under rotation, but Q and U depend on the reference frame and transform like a spin-2 object, which is when rotated by an angle ψ around $\hat{n}$, then Q and U rotate to Q' and U' by an angle 2ψ, as (ZALDARRIAGA, 1998; MEMARI, 2007; TUCKER, 2014)

$$(Q \pm iU)'(\hat{\mathbf{n}}) = e^{\mp 2i\psi}(Q \pm iU)(\hat{\mathbf{n}}), \tag{3.26}$$

where $\hat{\mathbf{n}}$ is the unit vector in the angular direction (θ, ϕ). Each quantity can be expanded in the appropriate spin-weighted basis, similarly to temperature anisotropies in eq. 3.2:

$$(Q + iU)(\hat{\mathbf{n}}) = \sum_{lm} a_{2,lm}\, {}_2Y_{lm}(\hat{\mathbf{n}}),$$

$$(Q - iU)(\hat{\mathbf{n}}) = \sum_{lm} a_{-2,lm}\, {}_{-2}Y_{lm}(\hat{\mathbf{n}}), \tag{3.27}$$

where Q and U are defined at each direction $\hat{\mathbf{n}}$ with respect to angular coordinates (θ, ϕ). In order to obtain the spin zero quantities, one needs to apply the spin raising and lowering operators. Here we are only using the results obtained by ZALDARRIAGA (1998) and MEMARI (2007):

$$a_{2,lm} = \left[\frac{(l+2)!}{(l-2)!} \right]^{-1/2} \int d\Omega Y_{lm}^*(\hat{\mathbf{n}})\bar{\eth}^2(Q + iU)(\hat{\mathbf{n}}),$$

$$a_{-2,lm} = \left[\frac{(l+2)!}{(l-2)!} \right]^{-1/2} \int d\Omega Y_{lm}^*(\hat{\mathbf{n}})\eth^2(Q + iU)(\hat{\mathbf{n}}), \tag{3.28}$$

where $\eth^2$ and $\bar{\eth}^2$ are *spin-weighted operators*. These operators are defined as:

$$\eth_s Y_{lm} = [(l-s)(l+s+1)]^{1/2}_{s+1} Y_{lm};$$

$$\bar{\eth}_s Y_{lm} = -[(l-s)(l-s+1)]^{1/2}_{s-1} Y_{lm}.$$

Instead of using $a_{\pm 2, lm}$, we introduce their linear combinations, which is more of a familiar form,

$$\begin{aligned}
a_{E,lm} &= -\frac{(a_{2,lm} + a_{-2,lm})}{2}, \\
a_{B,lm} &= i\frac{(a_{2,lm} - a_{-2,lm})}{2}.
\end{aligned} \tag{3.29}$$

In real space, these quantities become

$$\begin{aligned}
E(\hat{\mathbf{n}}) &= \sum_{lm} a_{E,lm} Y_{lm}(\hat{\mathbf{n}}); \\
B(\hat{\mathbf{n}}) &= \sum_{lm} a_{B,lm} Y_{lm}(\hat{\mathbf{n}}).
\end{aligned} \tag{3.30}$$

Using the previous equations, (3.28, 3.29), it is straightforward to show their distinct parities. Let us consider an inversion of the x coordinate but leave the others unchanged. In spherical coordinates, this leads to only a change in the sign of ϕ, $\phi \to \phi + \pi$. So, the *Stokes parameters transform*[2] as $Q'(\hat{\mathbf{n}}') = Q(\hat{\mathbf{n}})$ and $U'(\hat{\mathbf{n}}') = -U(\hat{\mathbf{n}})$. The implications of the transformation show that Q has even parity and U has odd parity.

Therefore, E and B have, respectively, even and odd parities. Under parity transformation the sign of $E(\hat{\mathbf{n}})$ remains the same, i.e. the gradient of the electric field, whereas $B(\hat{\mathbf{n}})$ changes sign, i.e. the curl of the magnetic field. Thus E and B can be thought as the electric and magnetic modes of the polarization function (TUCKER, 2014).

The statistics of the CMB perturbations are fully characterized by the power spectrum. Following the form of (3.6), we define the power spectra of the perturbations as:

$$\begin{aligned}
\langle a^*_{T,l'm'} a_{T,lm} \rangle &= \delta_{ll'} \delta_{mm'} C_l^{TT}; \\
\langle a^*_{E,l'm'} a_{E,lm} \rangle &= \delta_{ll'} \delta_{mm'} C_l^{EE}; \tag{3.31} \\
\langle a^*_{B,l'm'} a_{B,lm} \rangle &= \delta_{ll'} \delta_{mm'} C_l^{BB}; \tag{3.32} \\
\langle a^*_{T,l'm'} a_{E,lm} \rangle &= \delta_{ll'} \delta_{mm'} C_l^{TE}; \tag{3.33} \\
\langle a^*_{B,l'm'} a_{B,lm} \rangle &= \langle a^*_{B,l'm'} a_{B,lm} \rangle = 0. \tag{3.34}
\end{aligned}$$

---

[2]The operators $\eth$ and $\bar{\eth}$ act in the rotation transformation as

$$\bar{\eth}(Q+iU)'(\hat{\mathbf{n}}') = \eth(Q-iU)(\hat{\mathbf{n}})$$
$$\bar{\eth}^2(Q+iU)'(\hat{\mathbf{n}}') = \eth^2(Q-iU)(\hat{\mathbf{n}})$$

The temperature power spectra was included here for completeness of presentation. Also, the change of sign in B under parity transformation results in the cross correlations between B and T or E vanish. The study of $C_l^{TB,obs}$ and $C_l^{EB,obs}$ deviating from zero is a way to search for parity violation in the very early universe (LUE, 1999). However, the results found by Planck science team has determined that the constrains are dominated by systematic uncertainty (Planck Collaboration, 2016e).

The variance C_l for each of power spectra can be given as:

$$C_l^{TT} = \frac{1}{2l+1} \sum_{m=-l}^{l} \left\langle a_{T,lm} a_{T,l'm'}^* \right\rangle ;$$

$$C_l^{TE} = \frac{1}{2l+1} \sum_{m=-l}^{l} \left\langle a_{T,lm} a_{E,l'm'}^* \right\rangle ; \tag{3.35}$$

$$C_l^{EE} = \frac{1}{2l+1} \sum_{m=-l}^{l} \left\langle a_{E,lm} a_{E,l'm'}^* \right\rangle ; \tag{3.36}$$

$$C_l^{BB} = \frac{1}{2l+1} \sum_{m=-l}^{l} \left\langle a_{B,lm} a_{B,l'm'}^* \right\rangle . \tag{3.37}$$

The CMB polarization provides an additional source of information to the temperature data. The E-mode polarization comes mainly from *Thomson scattering*[3], of photons off of electrons in the fluid, close to last scattering ($z = 1100$), with a contribution at large angular scales from perturbations at the re-ionization epoch ($z \approx 10$) (HU, 2008; NAESS, 2014). Therefore, most of E-mode polarization is associated with the acoustic peaks anisotropies, which provides confirmation to the temperature data.

The combination of temperature and polarization data constrain a range of parameters that were degenerated with temperature data alone. The additional sensitivity increases the ability to probe neutrino properties, early dark energy and time variations of fundamental constants. Comparison of temperature and polarization data also probes cosmological effects which affect the two in different ways, such as kinematic Sunyaev-Zeldovich effect (NAESS, 2014).

Whereas, B-mode polarization does not come from primordial density perturbations, but it is induced by gravitational waves. A detection of this signal would represent a unique signal of tensor modes. However, current polarization observations of B-mode mostly come from weak gravitational lensing by all structures along the line-of-sight, for multipoles $l > 200$. Lensing converts some E-mode polarization into B-modes (NAESS, 2014).

---

[3]This scattering process does not change the photon's energy, but the unpolarized radiation generates linear polarization.
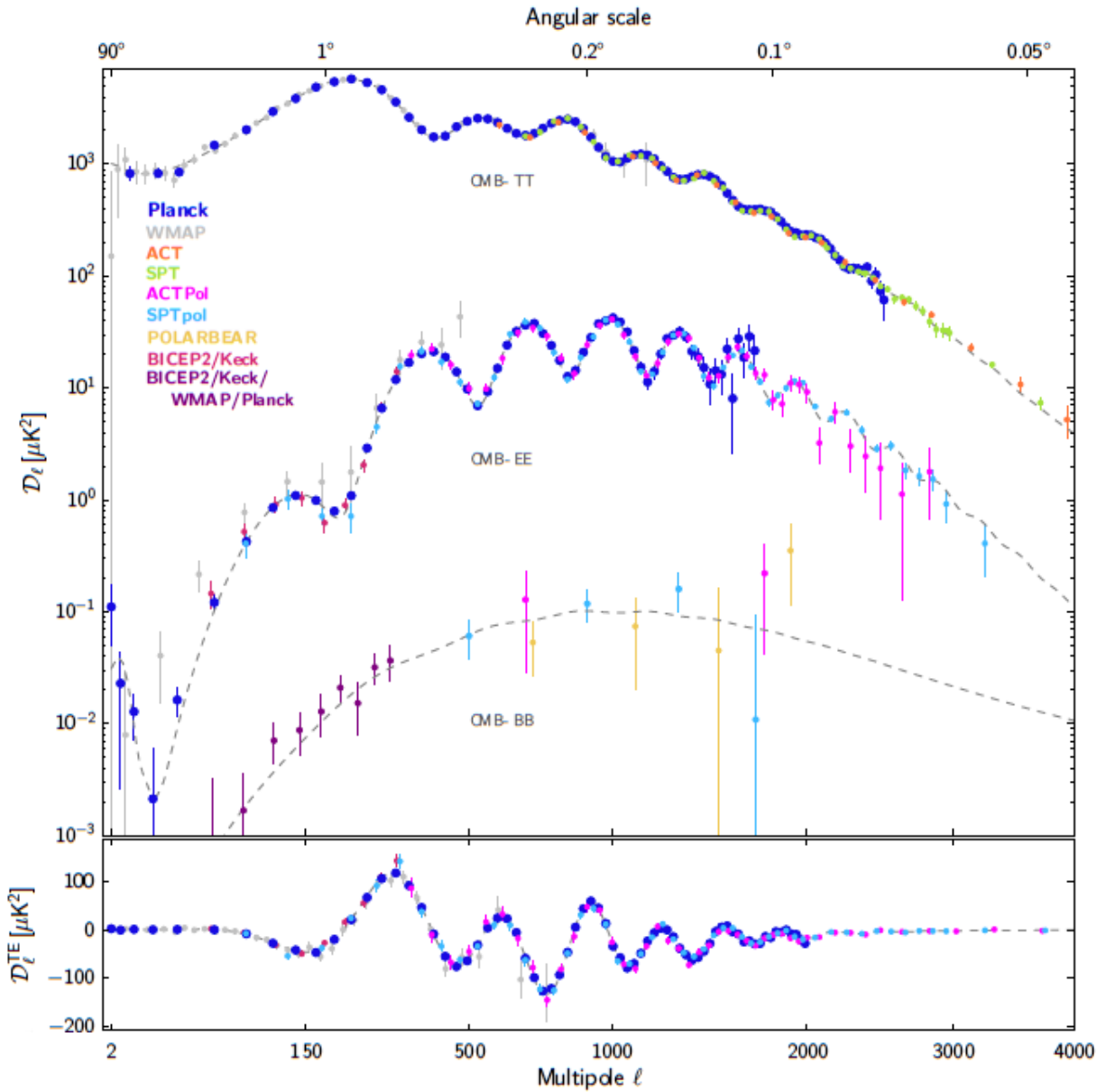
Figure 3.5: A compilation of the recent CMB angular power spectrum. The upper panel shows the power spectra of temperature, E-mode and B-mode polarization signals. The bottom panel shows the cross correlation of temperature and E-mode. Each colour corresponds to a different experiment. And the dash line refers to the best fit of the $\Lambda-$CDM model to the Planck temperature and polarization data. Source: Planck Collaboration (2018a).

4 NON-GAUSSIANITY

4.1 WHY SEARCH FOR IT?

The observations of the CMB power spectrum provide evidence for seed fluctuations in the early universe that originated our observable universe. Inflation is the leading theory for explaining the primordial origin of cosmological fluctuations and rapid expansion. Many theoretical ideas have been proposed to explain the existence of an early phase of accelerated expansion. Inflation models with a minimum number of degree of freedom, parameters and tuning needed to solve horizon and flatness problems give a fair well-defined range of predictions. However, the current experimental data has ruled out a good portion of models. There remains a substantial range of inflationary models that still fits the data (KOMATSU, 2009b; Planck Collaboration, 2016c).

The CMB power spectrum is determined by the inflationary expansion rate and the evolution of the inflationary energy density. Measurements of the power spectrum provide limited information about inflationary phase, and it alone is not enough to characterize the inflaton. In fact, the power spectrum is unable to strongly constrain the interactions of the field(s) associated with this energy density. In terms of inflationary action, the power spectrum is degenerated. Moreover, the different inflation models and different field interactions can lead to similar predictions for the power spectrum. The Non-Gaussianity (NG) is a sensitive probe to the different aspects of field(s) interactions that drive inflation and as a result contains vital information about the physics during inflation (KOMATSU, 2002, 2004; BARTOLO, 2004; Planck Collaboration, 2016b).

In many single field slow-roll models the NG is small and likely unobservable. However, a large, detectable amount of NG can be produced when any of these conditions is violated (KOMATSU, 2009a):

- *Single Field*: There was only one quantum field responsible for diving inflation and for generating the primordial seeds for structures.

- *Canonical Kinetic Energy*: The kinetic energy of the quantum field is such that the speed of propagation of fluctuations is equal to the speed of light.

- *Slow Roll*: The evolution of the field was always very slow compared to the Hubble time during inflation.

- *Initial Vacuum State*: The quantum field was in the preferred adiabatic vacuum state, which is also known as the "Bunch-Davies vacuum", just before the quantum fluctuations were generated during inflation.

The data has shown levels of primordial NG that are almost undetectable (KOMATSU, 2009b; Planck Collaboration, 2016c). These constrains have refuted inflation models that produce detectable amounts of NG. Thus, inflation is expected to produce undetectable levels of primordial NG only when all the conditions are satisfied. Therefore, the main goal on measuring NG is to confirm or to rule out the different classes of inflation models.

4.2 ANGULAR BISPECTRUM

The angular $n-$point function is a simple statistics that characterizes a clustering of fluctuations on the sky, $f(\hat{\mathbf{n}})$ (BARTOLO, 2004)

$$\langle f(\hat{\mathbf{n}}_1) f(\hat{\mathbf{n}}_2) ... f(\hat{\mathbf{n}}_n) \rangle,\tag{4.1}$$

here $f(\hat{\mathbf{n}})$ can be expanded in spherical harmonics in the same way as eq. 3.2.

$$f(\hat{\mathbf{n}}) = \sum_{l=0}^{\infty} \sum_{m=-l}^{l} a_{lm} Y_{lm}(\hat{\mathbf{n}}).$$

If the fluctuations are Gaussian, a 2-point correlation function is enough to describe all the statistical properties of $f(\hat{\mathbf{n}})$. Therefore, the 2-point function, or angular power spectrum, is the only parameter in a Gaussian distribution.

The information about the events that happened during recombination epoch is encrypted in the temperature anisotropies which can be described by a 2-point function. Nevertheless, the second order perturbations from inflation cannot. However, these primordial perturbations also obey Gaussian statistics. Then the deviations from Gaussian distribution can be measured by higher order correlation functions of CMB anisotropies. NG require at least a 3-point correlation function to be described.

The bispectrum is a 3-point correlation function of scalar perturbations that is capable of measuring NG features in the cosmological perturbations. The bispectrum is the lowest order statistics able to distinguish NG from Gaussian perturbations, because it is zero for Gaussian perturbations. The angular bispectrum is the harmonic conjugate of the 3-point correlation function and is given by

$$\langle a_{l_1 m_1} a_{l_2 m_2} a_{l_3 m_3} \rangle = B_{l_1 l_2 l_3}^{m_1 m_2 m_3},\tag{4.2}$$

and the averaged angular bispectrum is given by

$$B_{l_1 l_2 l_3} = \sum_{all\ m} B_{l_1 l_2 l_3}^{m_1 m_2 m_3} \begin{pmatrix} l_1 & l_2 & l_3 \\ m_1 & m_2 & m_3 \end{pmatrix},\tag{4.3}$$

here the matrix denotes the Wigner-3j symbol. Since l_1, l_2 and l_3 form a triangle, $B_{l_1 l_2 l_3}^{m_1 m_2 m_3}$

satisfies the triangle condition, $|l_i - l_j| \leq l_k \leq |l_i + l_j|$ for all permutation of indices. Parity invariance of the angular correlation function demands $l_1 + l_2 + l_3 = even$ and $m_1 + m_2 + m_3 = 0$.

An unbiased estimator can be defined in the same way it was done in (3.6)

$$\hat{B}_{l_1 l_2 l_3} = \sum_{all\ m} a_{l_1 m_1} a_{l_2 m_2} a_{l_3 m_3} \begin{pmatrix} l_1 & l_2 & l_3 \\ m_1 & m_2 & m_3 \end{pmatrix}. \tag{4.4}$$

It implies that $B_{l_1 l_2 l_3}^{m_1 m_2 m_3}$ consists of the Gaunt integral, $\mathcal{G}_{l_1 l_2 l_3}^{m_1 m_2 m_3}$, which is defined by

$$\mathcal{G}_{l_1 l_2 l_3}^{m_1 m_2 m_3} = \int d^2 \hat{\mathbf{n}} Y_{l_1 m_1}(\hat{\mathbf{n}}) Y_{l_2 m_2}(\hat{\mathbf{n}}) Y_{l_3 m_3}(\hat{\mathbf{n}}) \tag{4.5}$$

$$= \sqrt{\frac{(2l_1 + 1)(2l_2 + 1)(2l_3 + 1)}{4\pi}} \begin{pmatrix} l_1 & l_2 & l_3 \\ 0 & 0 & 0 \end{pmatrix} \begin{pmatrix} l_1 & l_2 & l_3 \\ m_1 & m_2 & m_3 \end{pmatrix}. \tag{4.6}$$

here $\mathcal{G}_{l_1 l_2 l_3}^{m_1 m_2 m_3}$ is real and satisfy all the Wigner-$3j$ symbol conditions. Rotational invariance of the angular 3-point correlation function implies that $B_{l_1 l_2 l_3}$ is written as

$$B_{l_1 l_2 l_3}^{m_1 m_2 m_3} = \mathcal{G}_{l_1 l_2 l_3}^{m_1 m_2 m_3} b_{l_1 l_2 l_3}, \tag{4.7}$$

where $b_{l_1 l_2 l_3}$ is an arbitrary real symmetric function of l_1, l_2 and l_3, named *reduced*[1] bispectrum. Therefore, the angular averaged bispectrum, $B_{l_1 l_2 l_3}$, by substituting eq. 4.7 into 4.3,

$$B_{l_1 l_2 l_3} = \sqrt{\frac{(2l_1 + 1)(2l_2 + 1)(2l_3 + 1)}{4\pi}} \begin{pmatrix} l_1 & l_2 & l_3 \\ 0 & 0 & 0 \end{pmatrix} b_{l_1 l_2 l_3}. \tag{4.8}$$

For small section of the sky or high multipole moments, it is sufficient to treat the sky as flat (HU, 2000; KOMATSU, 2002). Then, in the flat-sky limit, the Fourier transform of the 3-point function is

$$\langle a(\mathbf{l}_1) a(\mathbf{l}_2) a(\mathbf{l}_3) \rangle = (2\pi)^2 \delta^{(2)}(\mathbf{l}_1 + \mathbf{l}_2 + \mathbf{l}_3) B(\mathbf{l}_1, \mathbf{l}_2, \mathbf{l}_3), \tag{4.9}$$

and the bispectrum $B(\mathbf{l}_1, \mathbf{l}_2, \mathbf{l}_3)$ simplifies to $B(\mathbf{l}_1, \mathbf{l}_2, \mathbf{l}_3) \approx b_{l_1 l_2 l_3}$, where $|\mathbf{l}_i| = l_i$.

4.3 ORIGIN OF PRIMORDIAL NON-GAUSSIANITY

This section is based on the works from Komatsu (2002,2009) and Bartolo (2004). The *curvature perturbation*[2] Φ was the seed for the CMB anisotropy $\Delta T/T$. The linear perturbation

---

[1] The reduced bispectrum does not hold the Wigner-$3j$ symbol, which merely ensures the triangle conditions and selection rules. However, this quantity holds the same physical information as in the angular bispectrum, $B_{l_1 l_2 l_3}^{m_1 m_2 m_3}$.

[2] The curvature perturbation presented as Φ was introduced by Bardeen in 1980, and it is a gauge-invariant perturbation that contains the scalar perturbations ζ. The evolution of Φ on super-horizon scales in cosmological linear perturbation theory gives $\Phi = (3 + 3w)/(5 + 3w)\zeta$ (YADAV, 2010). Here w represents the equation of state of the universe, in radiation era $\Phi = (2/3)\zeta$ with $w = 1/3$, and in matter era $\Phi = (3/5)\zeta$ with $w = 0$.

theory gives a linear relation between Φ and $\Delta T/T$,

$$\frac{\Delta T}{T} \sim g_T \Phi, \tag{4.10}$$

where g_T is the radiation transfer function. The temperature fluctuations on super horizon scales at the decoupling epoch, the SW effect dominates, and $g_T = -1/3$ for adiabatic fluctuations. On sub-horizon scales, acoustic oscillations dominates and g_T oscillates. From the relation above, $\Delta T \propto \Phi$, so temperature fluctuations are Gaussian, if curvature perturbations are Gaussian. However, even when Φ is Gaussian, ΔT can still be non-Gaussian through the non-linear relation,

$$\frac{\Delta T}{T} \sim g_T (\Phi + f_\Phi \Phi^2). \tag{4.11}$$

According to the general relativistic cosmological perturbation theory, the second term with f_Φ is the highest order correction that arises from the second order gravitational perturbation theory. Therefore, even if Φ is Gaussian, ΔT becomes weakly non-Gaussian.

In fact, the non-linearity in inflation makes Φ weakly non-Gaussian. The fluctuations in the inflaton (2.24) can be expanded to a second order. We then obtain a relation between Φ and $\delta\phi$,

$$\Phi \sim M_{pl}^{-1} g_\Phi (\delta\phi + M_{pl}^{-1} f_{\delta\phi} \delta\phi^2), \tag{4.12}$$

for slow-roll inflationary scenarios with single field inflaton. $g_\Phi \sim \mathcal{O}(10)$, and $f_{\delta\phi} \sim \mathcal{O}(10^{-1})$. Moreover, if quantum fluctuations were able to produce Gaussian $\delta\phi$, there would be other possibilities for it to be perturbed as, for instance, a non-trivial coupling between long-wavelength classical fluctuations and short-wavelength quantum fluctuations. In that way, quantum fluctuations would have a Gaussian origin but weakly non-Gaussian, through the non-linear relation

$$\delta\phi \sim g_{\delta\phi} (\eta + M_{pl}^{-1} f_\eta \eta^2), \tag{4.13}$$

here η is a Gaussian, $g_{\delta\phi} \sim 1$, and $f_\eta \sim \mathcal{O}(10^{-1})$.

Rewriting all equations (4.11,4.12,4.13) as

$$\frac{\Delta T}{T} \sim g_T \big[\Phi_L + (f_\Phi + g_\Phi^{-1} f_{\delta\phi} + g_\Phi^{-1} g_{\delta\phi}^{-1} f_\eta) \Phi_L^2 \big], \tag{4.14}$$

where $\Phi_L \equiv g_\Phi g_{\delta\phi} M_{pl}^{-1} \eta \sim 10 M_{pl}^{-1} \eta$ is the Gaussian part of the curvature perturbations. Also, in $f_{NL} \sim f_\Phi + g_\Phi^{-1} f_{\delta\phi} + g_\Phi^{-1} g_{\delta\phi}^{-1} f_\eta$, the last term is dominant compared to the other two due to $\sim \mathcal{O}(10^{-2})$, from non-linearity in slow roll inflation. The f_{NL} parameter is dimensionless and can be used in different inflationary scenarios. Furthermore, by using the non-linear coupling parameter, f_{NL}, we can rewrite the last equation as

$$\Phi(\mathbf{x}) = \Phi_L(\mathbf{x}) + f_{NL} \big(\Phi_L^2(\mathbf{x}) - \langle \Phi_L^2(\mathbf{x}) \rangle \big), \tag{4.15}$$

the angular bracket denote the statistical ensemble average.

local	equilateral	orthogonal
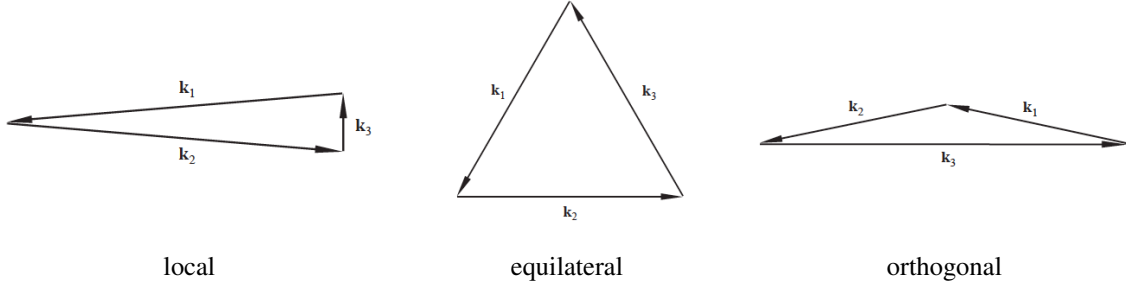
Figure 4.1: Non-Gaussianity triangular shapes. The shape function $F(k_1, k_2, k_3)$ forms the triangle in Fourier space, which depends on the k wave-vectors. For a local or "squeezed" shape, $k_3 \ll k_1 \approx k_2$; an equilateral shape, $k_1 \approx k_2 \approx k_3$, and orthogonal configuration, $k_1 \approx 2k_2 \approx 2k_3$. Source: LIGOURI (2010).

4.3.1 Primordial Bispectrum

Considering the primordial fluctuations as adiabatic scalar fluctuations,

$$a_{lm} = 4\pi(-i)^l \int \frac{d^3k}{(2\pi)^3} \Phi(\mathbf{k}) g_{Tl}(k) Y_{lm}(\hat{k}), \tag{4.16}$$

where $\Phi(\mathbf{k})$ is the curvature primordial perturbation in Fourier space, and g_{Tl} is the radiation transfer function, which contains all the physics to modify the curvature perturbations into CMB anisotropies. And, for adiabatic initial conditions, in the Sachs-Wolfe limit (YADAV, 2010),

$$g_{Tl} = -\frac{1}{3} j_l(k[\tau_0 - \tau_*]).$$

Any non-Gaussianities that might be contained in $\Phi(\mathbf{k})$ are taken by a_{lm}.

Then, the 3-point function (4.9) for the primordial perturbations becomes (YADAV, 2010)

$$\langle \Phi(\mathbf{k}_1)\Phi(\mathbf{k}_2)\Phi(\mathbf{k}_3) \rangle = (2\pi)^3 \delta^{(k)}(\mathbf{k}_1 + \mathbf{k}_2 + \mathbf{k}_3) B_\Phi(k_1, k_2, k_3), \tag{4.17}$$

where $\mathbf{k}$ is a 3-dimensional wave vector on the sky, and $B_\Phi(k_1, k_2, k_3)$ holds the information on the strength and shape of NG,

$$B_\Phi(k_1, k_2, k_3) = f_{NL} F(k_1, k_2, k_3),$$

here $F(k_1, k_2, k_3)$ is the shape function in momentum space while the amplitude of the NG is captured by the f_{NL} parameter. Both $B_\Phi(k_1, k_2, k_3)$ and f_{NL} are extremely model-dependent. Furthermore, the Dirac delta function enforces the triangle conditions as, i.e. the constraint that the wave-vectors in Fourier space must close to form a triangle: $\mathbf{k}_1 + \mathbf{k}_2 + \mathbf{k}_3 = 0$ (LIGOURI, 2010; YADAV, 2010).

The shape function $F(k_1, k_2, k_3)$ correlates the fluctuations with three wave-vectors and form a triangle in Fourier space. Depending on the physical mechanism responsible for the bispectrum, the shape of the 3-point is classified into three classes: *local*, *equilateral* and *orthogonal* (BABICH, 2004; SU, 2010). In figure 4.1 shows the three shapes and their
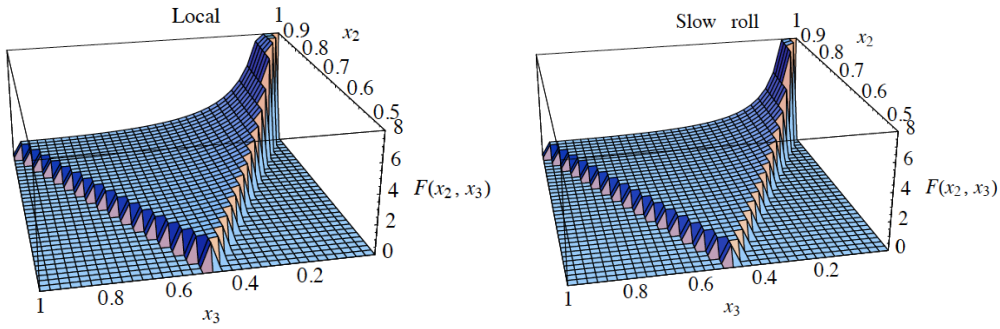
Figure 4.2: Plot of the bispectrum shape of local type (left panel), eq. 4.18. For slow-roll inflation, there are minor changes in eq. 4.18 (right panel). SOURCE: Babich (2004)

corresponding k wave-vectors.

First, the local or "squeezed" NG, where $F(k_1, k_2, k_3)$ is large for the configuration $k_3 \ll k_1 \approx k_2$. These is the most common shape for most of the inflationary, i.e. slow-roll, and Ekpyrotic models (YADAV, 2010). The motivation behind it encloses the super-horizon effects during inflation on a large scale mode as, i.e. k_3 has exited the Hubble radius, which exerts a non-linear influence on the subsequent evoltution of smaller scale modes, like k_1 and k_2 (LIGOURI, 2010). In local models, the f_{NL} often starts from $\mathcal{O}(1)$ to ~ 100 for different inflationary models. This constraint was given by the CMB bispectrum of WMAP temperature data (KOMATSU, 2003). The bispectrum for this model can be written as (YADAV, 2010; Planck Collaboration, 2016b):

$$B_{\Phi}^{local}(k_1, k_2, k_3) = 2f_{NL}^{local}[P_{\Phi}(k_1)P_{\Phi}(k_2) + P_{\Phi}(k_1)P_{\Phi}(k_3) + P_{\Phi}(k_2)P_{\Phi}(k_3)] \qquad (4.18)$$

$$= 2A^2 f_{NL}^{local}\left[\frac{1}{k_1^{4-n_s}k_2^{4-n_s}} + cycl.\right], \qquad (4.19)$$

where $P_{\Phi}(k) = A/k^{4-n_s}$ is the amplitude of the primordial power spectrum.

The local form arises from non-linear relation between inflaton and curvature perturbations, curvature models, models with fluctuations in the reheating efficiency, New Ekpyrotic models and multi-field inflationary models as, i.e. figure 4.2 (YADAV, 2010).

Second, the equilateral NG, where $F(k_1, k_2, k_3)$ is large for the configuration $k_1 \approx k_2 \approx k_3$. While most of the inflationary models predict NG of local type, this model does not work for a localized in a specific range in k space. The inflation models that predicts this type of NG usually have higher derivative kinetic terms. In these models the correlation is among modes with comparable wavelengths which go out of horizon nearly at the same time. The bispectrum for
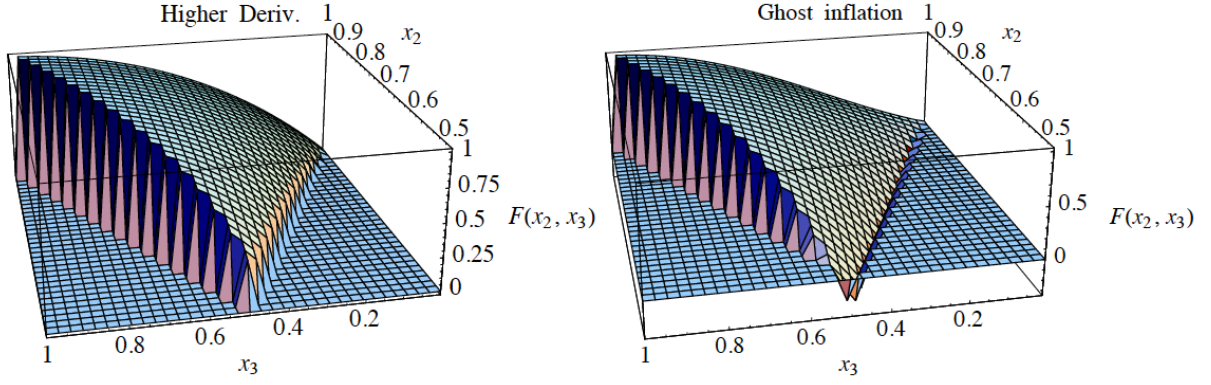
Figure 4.3: Plot of the bispectrum shape of equilateral type, eq. 4.20. Here it is presented two classes of inflation model of equilateral type, one for higher derivatives (left panel) and another for ghost inflation (right panel). SOURCE: Babich (2004)

this type is given as (YADAV, 2010; Planck Collaboration, 2016b):

$$B_\Phi^{equil}(k_1, k_2, k_3) = f_{NL}^{equil} 6A^2$$

$$\times \left[-\frac{1}{k_1^{4-n_s} k_2^{4-n_s}} - \frac{1}{k_1^{4-n_s} k_2^{4-n_s}} - \frac{1}{k_1^{4-n_s} k_2^{4-n_s}} - \frac{1}{(k_1 k_2 k_3)^{2(4-n_s)/3}} \right.$$

$$\left. + \frac{1}{k_1^{(4-n_s)/3} k_2^{2(4-n_s)/3} k_3^{4-n_s}} + (5\ permutations) \right], \qquad (4.20)$$

where the "permutation" term indicate cyclic permutations of k_i with $i = 1, 2, 3$. The equilateral form arises from non-canonical kinetic energy terms such as the Dirac-Born-Infeld (DBI) action, the ghost condensation, or any single-field models in which the scalar field acquires a low speed of sound. See figure 4.3 for illustration.

Finally, the folded, or orthogonal configuration where $F(k_1, k_2, k_3)$ is large for the configuration in which $k_3 \approx 2k_1 \approx 2k_2$. The bispectrum is given as (Planck Collaboration, 2016b):

$$B_\Phi^{ortho}(k_1, k_2, k_3) = 6A^2 f_{NL}^{equil}$$

$$\times \left[-\frac{3}{k_1^{4-n_s} k_2^{4-n_s}} - \frac{3}{k_1^{4-n_s} k_2^{4-n_s}} - \frac{3}{k_1^{4-n_s} k_2^{4-n_s}} - \frac{8}{(k_1 k_2 k_3)^{2(4-n_s)/3}} \right.$$

$$\left. + \frac{3}{k_1^{(4-n_s)/3} k_2^{2(4-n_s)/3} k_3^{4-n_s}} + (5\ permutations) \right]. \qquad (4.21)$$

this form is obtained by the combination of local and equilateral configurations. Usually, the model is constructed starting from some specific underlying symmetry for the inflation field, and is characterized by strongly constrained derivative interactions.

The Planck science team applied the bispectrum estimator to the CMB data in order to improve the constraints on primordial NG (Planck Collaboration, 2016b). Taking only

temperature data, the constraints on bispectrum shapes (4.18, 4.20, 4.21) were given as $f_{NL}^{local} = 2.5 \pm 5.7$, $f_{NL}^{equil} = -16 \pm 70$, and $f_{NL}^{ortho} = -34 \pm 33$. These were initially constrained in 2013 and had a mild improvement by 15% (for orthogonal shape) (Planck Collaboration, 2013b). However, these results were improved after using polarization data, which is complementary to temperature. The addition of polarization provided a final] constraints of $f_{NL}^{local} = 0.8 \pm 5.0$, $f_{NL}^{equil} = -4 \pm 43$, and $f_{NL}^{ortho} = -26 \pm 21$, which represents a substantially improvement from previous results, with errors bars shrinking by 14% (local), 43% (equilateral) and 46% (orthogonal) (Planck Collaboration, 2016b). Consequently, our understanding of the different inflationary candidates (models) that gave rise to the NG were improved by the limitations of the f_{NL} parameter.

5 SYSTEMATICS

The precise measurement of its temperature and polarization anisotropies has enabled a door to the physics of the early universe. And by early universe, we are talking about the inflationary phase that was a seed to processes that have built our universe as we see it today. Moreover, there are a lot of possibilities for what this seed was and we have got a lot of possibilities for it. These measurements can potentially pinpoint which model is correct. However, all the experiments collect data from all directions and cannot pick and choose which data comes from the CMB and which doesn't.

When it comes to CMB, there are a lot of 'things' in the way of the real data that could contaminate its signal, e.g. Galaxies, clusters and stars. However, not only foregrounds can contaminate the measurements, but also the instrument itself is a roadblock. In order to probe the early universe, these contaminants must be removed or reduced from the data. Otherwise, we won't be able to have a clear picture of the early universe.

This chapter is dedicated to explore the relevant Galactic and extragalatic foreground sources and the consequences of masking their emission, as well as instrument systematics.

5.1 FOREGROUND

The CMB anisotropies are considered the most powerful probe of the early universe, due to their richness in cosmological information. On that note, each of the experiments done so far (COBE (BENNETT et al. 1996), WMAP (HINSHAW et al. 2013), Planck (Planck Collaboration, 2018), DASI (LEITCH et al. 2005), MAXIMA (Hanany et al. 2000), BOOMERang (MacTavish et al. 2006), CBI (SIEVERS et al. 2009), ACBAR (Reichardt et al. 2009), ACT (SIEVERS et al. 2013) and SPT (Story et al. 2013)) has been more sensitive and with better angular resolution than its predecessor in order to strengthen the constrains on cosmological parameters, which are mostly derived from the total intensity (temperature) anisotropies. Nonetheless, CMB photons are polarized due to the Thomson scattering at recombination and reionization epochs (E and B modes). The observations of CMB polarization are expected to improve these constraints.

Despite that, the observations of the CMB are contaminated by astrophysical foregrounds, which are the main source of uncertainty in the measurements, as opposed to instrumental noise. Most of the cosmological information is contained in large angular scales of CMB anisotropies, $\Delta\theta \gtrsim 0.1°$, as are the main contaminants. Therefore, there is a considerable interest in understanding these contaminants in order to successfully subtract foreground from CMB data. The separation of the diffuse foreground is extremely difficult, since their spectra are not fully comprehended and intensities are similar to CMB signal.
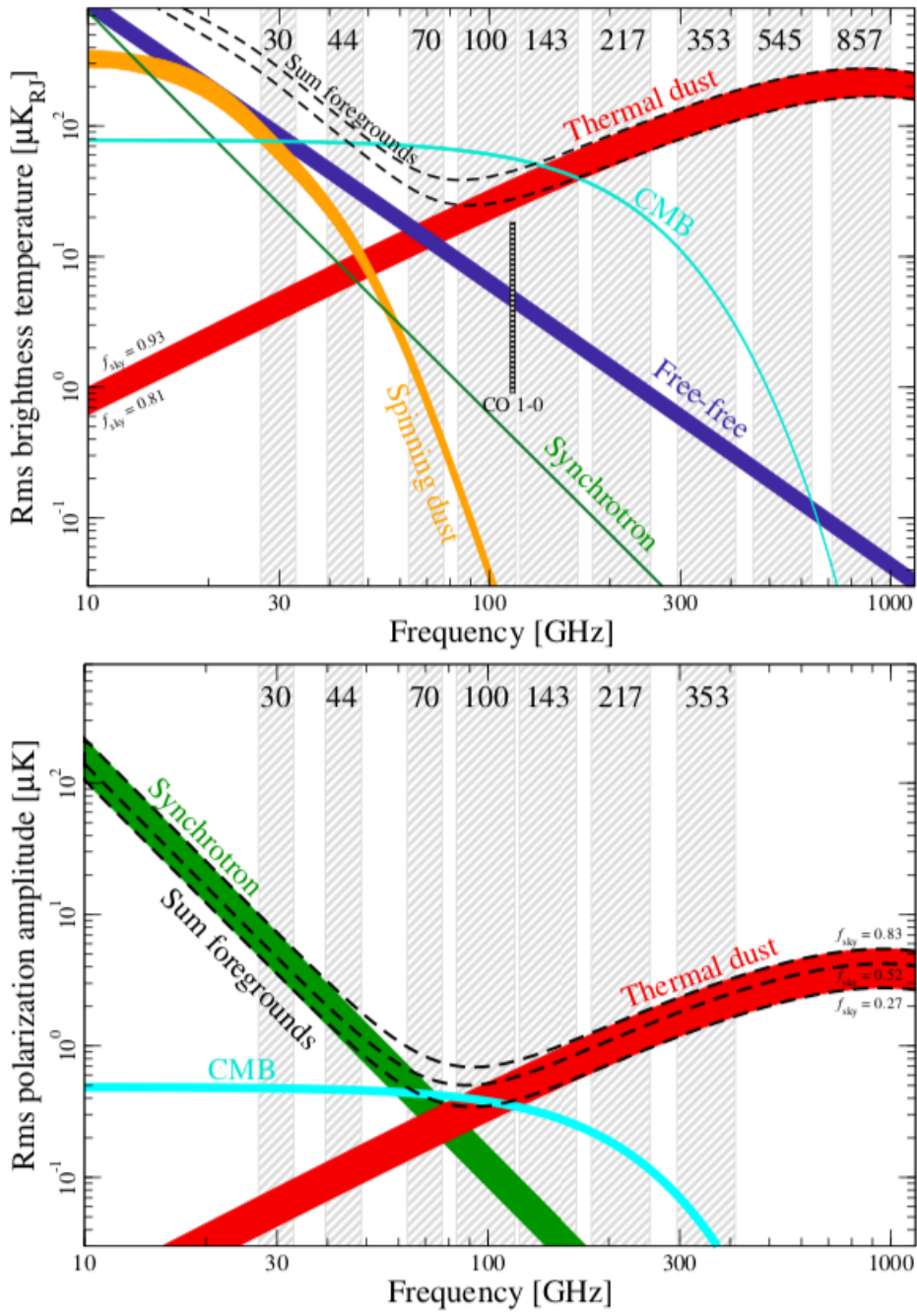
Figure 5.1: Frequency dependence on the main components of the Galactic foregrounds of the sky in temperature (*right*) and polarization (*left*). Source: Planck Collaboration (2018).

The Planck satellite, the most *precise*[1] experiment so far, has observed the CMB sky at 9 frequencies, from 30 to 857 GHz, and had its observations contaminated by Galactic foregrounds at all frequencies, fig. 5.1 (Planck Collaboration, 2018a). Therefore, each source of foreground dominates a different range of frequencies as, i.e. synchrotron emission dominates at low frequencies (≤ 30 GHz) and thermal dust at high frequencies (≥ 70 GHz). Now, regarding small angular scales, the contamination is mainly done by point sources, or extragalactic, foregrounds which are outside the Galactic plane.

5.1.1 Galactic Emission

5.1.1.1 Synchrotron

Synchrotron emission results from the interaction of relativistic (cosmic-ray) electrons in magnetic fields in the Galaxy, and thus depends on the energy spectrum of the electrons and the intensity of the magnetic field (RYBICKI, 1985). The acceleration occurs in *Type Ib* and *Type II supernova (SN)*[2] remnants. Thus, the synchrotron emission is associated with the star formation cycle (BENNETT, 2003).

The *power per unit frequency*[3] emitted by each electron can be written as:

$$P(\nu) = \frac{\sqrt{3}}{2\pi} \frac{q^3 B \sin\alpha}{mc^2} F\left(\frac{\nu}{\nu_c}\right), \tag{5.1}$$

here q and m are the charge and mass of an electron, ν is the frequency of a given electron, α is the electron direction pitch angle to the magnetic field B, and F is a frequency dependent function. The critical synchrotron frequency ν_c characterizes the emission spectrum (SMOOT, 1999),

$$\nu_c = \frac{3\gamma^2 qB}{2mc} sin\alpha. \tag{5.2}$$

The energy spectrum of cosmic-ray electrons is expressed as a relativistic electron number density distribution , $N(E)dE = N_0 E^{-p} dE$. Since $N(E)$ varies across the galaxy, as does the magnetic field, which results in significant spatial variations in spectral index on the sky. The synchrotron spectrum is approximated by a power law (DAVIES, 1998; KOGUT, 2007; ICHIKI, 2014),

$$T(\nu) \propto \nu^\beta, \qquad\qquad \beta = -\frac{p+3}{2}, \tag{5.3}$$

typically with $\beta_s \approx -2.7$ at radio frequencies, steeping to $\beta_s \approx -3.0$ at frequencies above 20 GHz and with typical spatial variation of ± 0.2 (ICHIKI, 2014). Moreover, it is known that a

---

[1]In terms of resolution, the ACT and SPT provided a better resolution than Planck (NASA, 2018). However, both of them observed the sky in small patches. As of today, Planck satellite is the most precise experiment with full sky coverage.

[2]the same $M > 8M_\odot$ stars that form these remnants also emit UV radiation that heats dust grains and ionizes hydrogen in the interstellar medium (IM)

[3]see Chapter 6 section 2 of RYBICKI (1985)

pure synchrotron spectrum steepens with frequency due to effects of spectral aging, although this could happen due to the presence of multiple components (MACELLARI, 2011).

The cosmic-ray electrons are originated mainly in SN then diffuse outwards in the expanding remnant. Structure will be formed in the remnant as it collides with the non-uniform ambient medium. The magnetic field will be likewise amplified in compression regions and vary in strength and direction. The net effect is to produce elongated synchrotron emission structures on a wide range of scales. The spectrum index of emission varies with position in two manners by the electron spectral index that changes from one SN to another and by the spectrum steeps with time due to radiation energy loss, resulting in a aging spectral index (DAVIS, 1998).

The synchrotron emission is produced in and near the Galactic plane, dominating at low-frequencies ($\nu \leq 30$ GHz), and its spectrum is not simple to model (Planck Collaboration, 2015a). The first throughout sky survey, in 408 MHz, was done by Haslam in 1981, which was followed by Reich in 1986, in 1420 MHz, then in 2.3 GHz by Jonas in 1998 and most recently by Tello in 2013. These surveys provided a high Signal to Noise (S/N) data set which assists in the component separation methods.

Synchrotron emission is highly polarized and dominates at frequencies below 50 GHz. Thus, accurate modeling of the Galactic cosmic-ray and magnetic field distribution can in principle be used to predict the polarization foreground and remove it from observed maps. The resulting synchrotron emission is partially polarized with fractional linear polarization,

$$f_s = \frac{p+1}{p+\frac{7}{3}},$$

aligned perpendicular to the magnetic field (RYBICKI, 1985). For spectral index ≈ -3, the fractional polarization is as high as $f_s \sim 0.75$ (KOGUT, 2007). The line-of-sight tend to reduce the observed polarization because it averages over regions with different electron distribution and magnetic field orientation.

5.1.1.2 Free-Free

Free-free emission (or bremsstrahlung) arises from electron-electron scattering from warm ($T_e \approx 10^4$ K) ionized gas in the interstellar medium. This diffuse component can be traced with Hα line of emission, both of which come dominantly from *H II regions*[4] in the galaxy. There are no sky surveys of free-free emission because it does not *dominate the sky*[5] at any of the CMB's frequency range (BENNETT, 2003). However, a close approximation for the free-free emission are the sky maps of Hα (hydrogen transition from $n = 3$ to $n = 2$) emission, which are in high-resolution and in large-scale (BENNETT, 2003; Planck Collaboration, 2016d).

---

[4]Under the right conditions, such as near a hot star or after a supernova explosion, the gas can become ionized, and these places are called H II regions. The gas in both states is more generally called the interstellar medium or ISM.

[5]Free-free emission contributes with some level of excess emission at 20-100 GHz (Planck Collaboration, 2016d). However, it is mostly overpowered by other Galactic emissions.

For an optically-thin regime, the intensity is given by an integration along the line-of-sight, as in $I_\nu = \int j_\nu ds$ (RYBICKI, 1985; ICHIKI, 2014):

$$j_\nu = 6.8 \times 10^{-38} \frac{g_{ff} Z_i^2 n_e n_i}{\sqrt{T_e}} \exp\left(-\frac{h\nu}{kT_e}\right) (erg\ s^{-1} cm^{-3}), \tag{5.4}$$

here, n_e and n_i are the number density of electrons and ions, respectively, Z_i is the atomic number, and T_e is the electron temperature. The gaunt factor for free-free emission is approximately given by, for $h\nu \ll kT$

$$g_{ff} = \frac{\sqrt{3}}{\pi}\left[\ln \frac{(2kT)^{3/2}}{\pi e \nu \sqrt{m}} - \frac{5\phi}{2}\right], \tag{5.5}$$

where e and m are the electron charge and mass, respectively, and ϕ is the Euler constant. Therefore, the free-free emission has a high-frequency ($\nu > 10$ GHz) spectrum of $T \sim \nu^{\beta_f}$, with $\beta_f = -2.15$, and a low-frequency rise of $T \sim \nu^2$ due to optically thick self-absorption (BENNETT et al. 2003).

The two-parameter model of DRAINE (2011) and adopted by Planck Collaboration (2015a) for analysis are the intensity of emission, I_ν, and the electron temperature, T_e. In figure 5.1, the spectrum is close to a power law. Therefore, its amplitude is determined by the intensity of emission. The Planck Collaboration (2015a) ran up and down the spectrum index to find that it changes very slightly with temperature, i.e. from $\beta_f = -2.13$ for $T_e = 500$ K to $\beta_f = -2.15$ for $T_e = 20000$ K. The effective free-free emission is ≈ -2.14 for $T_e \approx 8000$ K. At low-frequencies, this component is significantly degenerated with synchrotron emission, but its power law index is flatter than for synchrotron which makes it easier to distinguish them.

Thermal free-free emission is intrinsically unpolarized because the scattering directions of electrons are isotropic and random. However, a secondary polarization signature can occur at the edges of bright free-free features as, i.e. H II regions, from Thomson scattering (RYBICKI, 1985). This could cause a significant polarization, $\sim 10\%$, in the Galactic plane, particularly when observed at high angular resolution. However, for optically thin plasmas at high Galactic latitude, the effect should be small, $< 1\%$. Free-free emission was found to be unpolirazed with an upper limit of 3.4% at the 95% confidence level (MACELLARI, 2011).

5.1.1.3   Thermal Dust

Thermal dust emission arises when dust grains in the interstellar medium absorb optical and UV photons and re-radiate the energy in the far-infrared. The spectrum is defined by a modified black-body and can be approximated to (KOGUT, 2007; Planck Collaboration, 2013a)

$$I_\nu \approx \tau_d \left(\frac{\nu}{\nu_d}\right)^{\beta_d} B(T), \tag{5.6}$$

where the optical depth τ_d is defined at reference frequency ν_d, β_d is the spectral index, and $B_\nu(T)$ is the Planck function for dust at temperature T. The temperature is determined by the interstellar radiation field (heating). Also, the dust that is hotter for any reason, efficiency of absorption, contribute more to the emission, at all frequencies, than colder dust. Moreover, a variety of circumstances and shapes of dust grains lead to multiple temperatures (ICHIKI, 2014), and along the line-of-sight it is possible that dust properties may vary.

The thermal dust dominates Galactic foreground at far-infrared and submilimetre wavelength ($\nu \geq 70$ GHz). SCHELEGEL et al. (1998) presented a full sky 100 μm map of Galactic dust based on COBE/DIRBE and IRAS/ISSA data and is mainly used as an estimator for Galactic extinction. FINKBEINER et al. 1999 adopted two temperature components (the so-called Model 8) as $T_{1,2} = (9.4, 16.2)$ K and $\beta_{d1,2} = (1.67, 2.70)$, respectively, and has been used to predict the dust foregrounds at microwave frequencies.

Detailed all-sky maps of dust intensity and temperature have been released by the Planck Collaboration, where they have derived the temperature using IRIS 100 μm and the Planck-HFI data at 857 and 545 GHz (Planck Collaboration, 2011). Along the Galactic plane, temperatures varying from $T \approx 14 - 15$ K in the outer Galactic regions to the inner Galactic regions around the Galactic center regions $T \approx 19$ K. This tendency is probably due to the presence of massive stars and warmer dust in the inner Galaxy regions. Near the Galactic poles, the temperature determination becomes noisy, due to the low signal levels.

The polarization peaks near the V band ($\lambda_{max} \approx 0.55$ μm) and is produced by dust grains that are somehow partially aligned by the interstellar magnetic field (DAVIS, 1951; DRAINE 2011)[6]. The polarization is higher along the longest axis when the magnetic field is uniform and perpendicular to the line-of-sight. However, the alignment mechanism is still a puzzle and the polarization fraction also depends on grains size distribution.

5.1.1.4 Spinning Dust

Dust radiates in another form at microwave wavelengths in addition to the thermal dust emission. This emission is associated with ultra small dust grains spinning and with non-zero electric dipole moment, producing electric dipole radiation (DRAINE, 1998a, 1998b). The physical process associated with the spinning dust emission is pretty straightforward: the grains will spin due to interaction with the ambient interstellar medium and radiation field, thus radiate electromagnetic waves, due to their electric dipole moment. (ALI-HAÏMOUD, 2009).

First observations of this anomalous microwave emission were interpreted as free-free emission from shock-heated gas, which was inconsistent due to the lack of consistency with Hα data (ICHIKI, 2014). See more on LEITCH (2013). The power spectrum of this emission requires a large number of small grains, their dipole moments and their rotational velocities. Its expected peak frequency is still uncertain, because it depends on physical properties of grains,

---

[6]For a more detailed description of polarization see Chapter 21, section 3 of DRAINE (2011)

but it typically lies on the $\sim 20 - 60$ GHz range. Consequently, the shape of the spectrum is also uncertain (Planck Collaboration, 2015a).

Finally, the polarization generated by these small dust grains, which normally are aligned weakly with the magnetic field, is assumed to be negligible. Currently, the best constrains on the polarization fractional, at peak frequencies, are at the level of $1 \sim 3\%$ and less than 1% at higher frequencies (Planck Collaboration, 2015a, 2015c).

5.1.2 Extragalactic Sources

The extragalactic contamination comes essentially from background galaxies as, i.e. radio point sources and Cosmic Infrared Background (CIB) contaminants, and clusters. These are responsible for the Sunyaev-Zel'dovich effect (SZe).

The SZe is the spectral distortion of the CMB photons produced by the Compton interaction with the intracluster hot and ionized gas. After such a scatter, the spectrum is no longer a perfect blackbody, which provides a unique observation signature. Despite the fact the effect is weak, it provides the brightest clusters on the sky (Planck Collaboration, 2015a). The surveys of galaxy clusters have improved considerably after using the SZe, because it is a powerful tool for sampling clusters at high redshift. The combined observations from space- and ground-based instruments, i.e. Planck (Planck Collaboration, 2009), SPT (CARLSTROM, 2011) and ACT (FOWLER, 2007), released catalogues of SZe selected clusters. Moreover, these surveys improved the constrains of this emission and the understanding of cluster mass over a broad range of redshift.

The galaxies radiate, and throughout cosmic history, this emission appears as a diffuse cosmological background. The CIB is the far-infrared part of this emission, and it contains about half of its total energy (Planck Collaboration, 2013b). This emission contains a lot of information about the process of star forming at high redshift, because it is produced by the stellar-heated dust within galaxies (Planck Collaboration, 2013a). Even though these processes are extremely difficult to detect individually, the CIB represents an exceptional tool for studying these objects and for tracing their overall distribution.

The radio point source come from Active Galactic Nuclei (AGN) which are observed via their synctrotron emission. These have been well-known and catalogued at high and low frequencies. Moreover, the foreground maps for this source are more similar in frequency to the free-free or thermal dust emission maps (Planck Collaboration, 2016c). Then, the radio contaminant, that were catalogued are removed from the signal.

5.1.3 Foreground-Cleaned maps

The foreground removal is not new to cosmology due to the need to remove contamination from actual data. The Planck satellite has observed the sky in nine different frequencies in
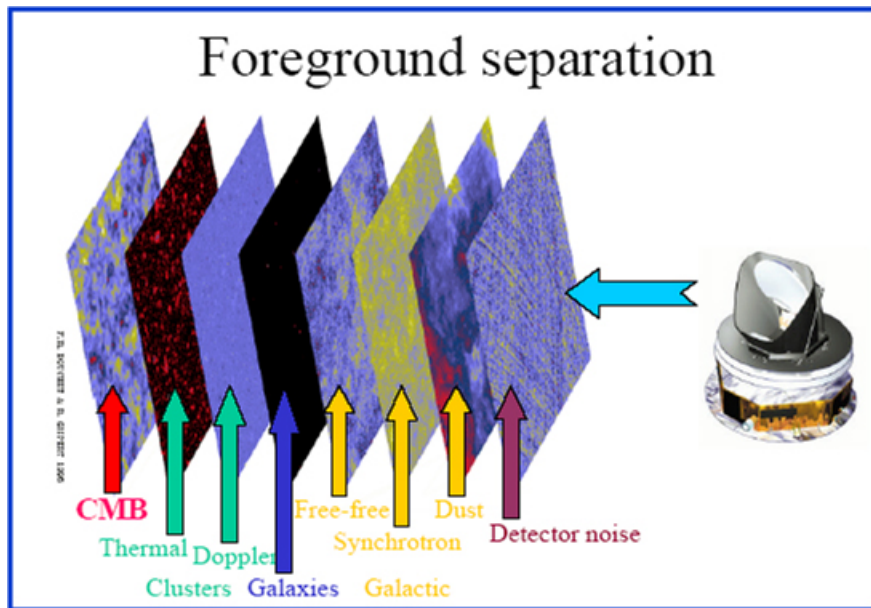
Figure 5.2: Representation for the foreground sources from detection to the CMB signal. By accurately measuring the light coming from these sources, it is possible to separate them from the CMB signal. SOURCE: Caltech website

temperature and polarization throughout its 8-year mission. The data acquired in this mission was combined to previous observations done by Planck's predecessors in order to best constrain foreground emission and isolate the CMB signal while cleaning the contamination. See figure 5.2.

The Planck satellite made use of four different component separation methods, which are the main approaches developed throughout the years. These are the following:

- *Commander*(ERIKSEN, 2008): is a Bayesian parametric method that works in the map domain. Both CMB and foregrounds are modelled using a physical paramaterization in terms of amplitudes and frequency spectra, which is perfect to perform astrophysical component separation (Planck Collaboration, 2015c);

- *NILC* (BASAK, 2012,2013): is an implementation of internal linear combination (ILC) that works in the needlet (wavelet) domain. The input maps are decomposed into needlets at a number of different angular scales, which minimizes the variance of scales (Planck Collaboration, 2015c);

- *Sevem* (LEACH, 2008): is an implementation of the template-cleaning approach to component separation that works in the map domain. Foreground templates are constructed from differentiating two maps which are used to clean each CMB-dominated frequencies. The final CMB map is produced from a combination of cleaned maps in harmonic space (Planck Collaboration, 2015c);

- *SMICA* (CARDOSO, 2008): is a non-parametric method that works in the spherical harmonic domain. Foreground are modelled from arbitrary values which are auto- and

cross-power spectra of the frequency channel maps. The final CMB map is derived from a combination of these frequency maps in the spherical harmonic domain (Planck Collaboration, 2015c).

Each method produces CMB maps in Stokes I, Q and U; its own confidence masks; effective beam and a noise estimate map that together characterize the CMB (Planck Collaboration, 2018a). However, these methods cleaned the maps from Galactic foreground emission, mostly present at large angular scales, and some extragalactic emission, those which were catalogued by previous sky surveys. The unresolved point sources, mostly present at small angular scales, were not masked (Planck Collaboration, 2015). Therefore, the foreground-cleaned CMB full-sky maps still carry some foreground residuals.

5.2 INSTRUMENTAL SYSTEMATIC EFFECTS

The evolution of the CMB instruments provided a new generation of precise measurements of temperature and polarization. However, these are subjected to errors which come from the instruments as, i.e. calibration, and their effect on data collecting process. Therefore, it is important to characterize these systematics in order to successfully reduce their effects on our measurements (SU, 2010).

The data used in the present work was taken from the Planck satellite, which is the third generation of space radiometer. Planck made use of two instruments over its 8 year flight. The Low Frequency Instrument (LFI) is an array of 22 coherent microwave radiometers in the 30, 44 and 70 GHz frequencies (Planck Collaboration, 2011a). The LFI front-end is cooled to 20 K for optimal sensitivity. As for the High Frequency Instrument (HFI) covers the 100 to 850 GHz bands with bolometers cooled to 0.1 K (Planck Collaboration, 2011b).

Both of these instruments have their own systematic effects. Radiometers have been studied for a long time, since COBE-DMR. And, bolometers have been studied just as much since Planck. These systematic effects cannot be removed but can be reduced. In 2015, Planck team has achieved a great breakthrough in the LFI uncertainties (Planck Collaboration, 2015b). Although the instrumental systematics have been reduced throughout the year, residual systematic effects can still be seen in the maps, which makes their characterization even more important, when taking into consideration the analysis of the early universe (SU, 2010). In the following subsections, we will characterize the effects of instrumental systematics in the bispectrum.

5.2.1 Temperature Systematics

When considering the instruments that measure temperature, three parameters can be introduced: the linear calibration (gain fluctuation) parameter of receivers, $a(\hat{\mathbf{n}})$, the non-linear

response of the detectors to observed CMB parameter, $b(\hat{\mathbf{n}})$, and the effects associated with optical imperfections, i.e. beam shape, c (SU, 2010)

$$\Theta^{obs}(\hat{\mathbf{n}}) = [1 + a(\hat{\mathbf{n}})]\Theta(\hat{\mathbf{n}}) + b(\hat{\mathbf{n}})\Theta(\hat{\mathbf{n}})^2 + [c \otimes \Theta](\hat{\mathbf{n}}) + ... \tag{5.7}$$

The last term here accounts for effects associated with beam systematics. Here, $\otimes$ represents the convolution in 2-D real space, which corresponds to a product in multipole space $\tilde{c}(\mathbf{l})\tilde{\Theta}(\mathbf{l})$ and implies a $l - l$ coupling (SU, 2010). The beam shape effects will only modify the $l-$dependence of an already existing bispectrum as, i.e. in case that $f_{NL} = 0$ these beam effects are irrelevant.

Instrumental systematics have an impact on the measured bispectrum. For instance, the linear calibration systematics of detectors can only distort the primordial CMB bispectrum. In other words, any detection with only the presence of linear systematics means the detection of primordial NG. In constrast, non-linear systematics can produce new but spurious bispectrum even when there is no primordial bispectrum signal.

The CMB 3-point function of the temperature is affected by the linear $a(\hat{\mathbf{n}})$ and non-linear $b(\hat{\mathbf{n}})$ systematics (SU, 2010)

$$
\begin{aligned}
\left\langle \Theta^{obs}(\hat{\mathbf{n}}_1)\Theta^{obs}(\hat{\mathbf{n}}_2)\Theta^{obs}(\hat{\mathbf{n}}_3)\right\rangle_{CMB,syst} =& \left\langle \Theta(\hat{\mathbf{n}}_1)\Theta(\hat{\mathbf{n}}_2)\Theta(\hat{\mathbf{n}}_3)\right\rangle_{CMB} \\
&+ \left\langle a(\hat{\mathbf{n}}_1)\right\rangle_{syst}\left\langle \Theta(\hat{\mathbf{n}}_1)\Theta(\hat{\mathbf{n}}_2)\Theta(\hat{\mathbf{n}}_3)\right\rangle_{CMB} + (perm.) \\
&+ \left\langle b(\hat{\mathbf{n}}_1)\right\rangle_{syst}\left\langle \Theta^2(\hat{\mathbf{n}}_1)\Theta(\hat{\mathbf{n}}_2)\Theta(\hat{\mathbf{n}}_3)\right\rangle_{CMB} + (perm.) \\
&+ \left\langle a(\hat{\mathbf{n}}_1)a(\hat{\mathbf{n}}_2)\right\rangle_{syst}\left\langle \Theta(\hat{\mathbf{n}}_1)\Theta(\hat{\mathbf{n}}_2)\Theta(\hat{\mathbf{n}}_3)\right\rangle_{CMB} + (perm.) \\
&+ \left\langle a(\hat{\mathbf{n}}_1)b(\hat{\mathbf{n}}_2)\right\rangle_{syst}\left\langle \Theta^2(\hat{\mathbf{n}}_1)\Theta(\hat{\mathbf{n}}_2)\Theta(\hat{\mathbf{n}}_3)\right\rangle_{CMB} + (perm.) \\
&+ \left\langle a(\hat{\mathbf{n}}_1)a(\hat{\mathbf{n}}_2)a(\hat{\mathbf{n}}_3)\right\rangle_{syst}\left\langle \Theta(\hat{\mathbf{n}}_1)\Theta(\hat{\mathbf{n}}_2)\Theta(\hat{\mathbf{n}}_3)\right\rangle_{CMB} + (perm.)
\end{aligned}
\tag{5.8}
$$

The correlation function could go on to higher orders, but in our case we are only interested in in terms up to second order in CMB fields, that is $\Theta^2(\hat{\mathbf{n}})$. The first term is the signal coming from the primordial bispectrum as, i.e. the target signal. The second term is the first order gain response from linear systematics. When this term is non-zero, this term introduces a linear bias to the primordial signal. In case of non-zero $\langle b(\hat{\mathbf{n}})_{syst}\rangle$, the third term introduces a new bispectrum even if there is no primordial NG. The self correlation of linear distortion field parameter, in the forth term, is capable of distorting the existing primordial bispectrum. If the systematics field is NG, then the term containing three distortion parameters, $\langle a(\hat{\mathbf{n}}_1)a(\hat{\mathbf{n}}_2)a(\hat{\mathbf{n}}_3)\rangle_{syst}$, can also contaminate f_{NL} measurements.

In a flat-sky approximation, the observe temperature anisotropy that was contaminated by calibration can be written as (SU, 2010),

$$\Theta(\mathbf{l})^{obs} = \Theta(\mathbf{l}) - \int \frac{d^2\mathbf{l}'}{(2\pi)^2}\Theta(\mathbf{l}')\left[a(\mathbf{l} - \mathbf{l}') + \int \frac{d^2\mathbf{l}''}{(2\pi)^2}\Theta(\mathbf{l}'')b(\mathbf{l} - \mathbf{l}' - \mathbf{l}'') + ...\right]. \tag{5.9}$$

The effect of systematics on bispectrum can be obtained by Fourier transforming of the temperature bispectrum affected by systematics, in 5.8. Then, the total observed bispectrum is (SU, 2010)

$$B^{TTT,\,obs}_{(l_1,l_2,l_3)} = B^{TTT,\,primordial}_{(l_1,l_2,l_3)} + \delta B^{TTT,\,dist}_{(l_1,l_2,l_3)} + B^{TTT,\,bias}_{(l_1,l_2,l_3)} \qquad (5.10)$$

where X, Y, Z is temperature or E-mode polarization field of CMB. The $B^{TTT,\,primordial}_{(l_1,l_2,l_3)}$ is the primordial signal that we are interested in, the right-hand side terms $B^{TTT,\,bias}_{(l_1,l_2,l_3)}$ and $\delta B^{TTT,\,dist}_{(l_1,l_2,l_3)}$ are respectively the bispectrum contribution from linear and non-linear systematics, and the systematic distortion.

5.2.2 Polarization Systematics

The measurement of CMB polarization is complicated due to its low intensity signal that could be masked by galactic foreground emission and various systematic effects. The instrument used for measuring the polarization is the Polarization Sensitive Bolometer (PSB), which measures the intensity of one direction of the polarization. Polarization measurements involve taking the difference of received intensity at two orthogonal polarizers. Any differences between the two PSBs might generate spurious Q and U signals. Therefore, if several detectors are combined to obtain these maps, it is important to match the responses of these detectors precisely in terms of cross-calibration, beam shape, spectral response, etc.

The polarization systematics are associated with the detector system which distorts the polarization state of the incoming polarization signal (type 1 systematics), and with systematics of the CMB signal due to the beam anisotropy (type 2 systematics).

The first order, the effects of type 1 systematics on the Stokes parameters are (HU, 2002b; SU, 2010)

$$\delta[Q \pm iU](\hat{\mathbf{n}}) = [a \pm i2\omega](\hat{\mathbf{n}})[Q \pm iU](\hat{\mathbf{n}}) + [f_1 \pm if_2](\hat{\mathbf{n}})[Q \mp iU](\hat{\mathbf{n}}) + [\gamma_1 \pm i\gamma_2](\hat{\mathbf{n}})\Theta(\hat{\mathbf{n}}), \quad (5.11)$$

where $a(\hat{\mathbf{n}})$ is a scalar field that describes the miss-calibration of the polarization measurements, $\omega(\hat{\mathbf{n}})$ is another scalar field which describes the rotation of the instrument, $(f_1 \pm if_2)(\hat{\mathbf{n}})$ are spin ± 4 fields that describe the coupling between two spin ± 2 states (spin-flip), and $(\gamma_1 \pm i\gamma_2)(\hat{\mathbf{n}})$ are spin ± 2 fields that describe monopole leakage from temperature to polarization.

The effect of type 2 systematics on the Stokes parameters can be written as (HU, 2002b; SU, 2010)

$$\begin{aligned} \delta[Q \pm iU](\hat{\mathbf{n}}, \sigma) &= \sigma\mathbf{p}(\hat{\mathbf{n}})\boldsymbol{\nabla}[Q \pm iU](\hat{\mathbf{n}}, \sigma) \\ &\quad + \sigma(d_1 \pm id_2)(\hat{\mathbf{n}})(\partial_1 \pm i\partial_2)\Theta(\hat{\mathbf{n}}, \sigma) + \sigma^2 q(\hat{\mathbf{n}})(\partial_1 \pm i\partial_2)^2\Theta(\hat{\mathbf{n}}, \sigma) + ... \end{aligned} \qquad (5.12)$$

where the systematic fields are smoothed over the average beam σ of the experiment. Therefore, the type 2 effects are sensitive to the imperfections of the beam on the beam scale, σ. The spin ± 1 fields, $(p_1 \pm ip_2)$ and $(d_1 \pm id_2)$ describe pointing errors and dipole leakage from temperature

to polarization respectively, and q is a scalar field that represents quadrupole leakage.

The non-linearity of the instruments can be parametrized as (HU, 2002b; SU, 2010)

$$
\begin{aligned}
\delta[Q \pm iU](\hat{\mathbf{n}}) = {} & [\tilde{\gamma_1} \pm i\tilde{\gamma_2}](\hat{\mathbf{n}})\Theta(\hat{\mathbf{n}})^2 \\
& + \sigma[\tilde{d_1} \pm i\tilde{d_2}](\hat{\mathbf{n}})(\partial_1 \pm i\partial_2)\Theta^2(\hat{\mathbf{n}}, \sigma) + \sigma^2 \tilde{q}(\hat{\mathbf{n}})(\partial_1 \pm i\partial_2)^2\Theta^2(\hat{\mathbf{n}}, \sigma) + ...
\end{aligned}
\tag{5.13}
$$

where $\tilde{\gamma_i}$ are spin ± 2 non-linear parameters which describe the second order leakage from temperature to polarization states, and $\tilde{d_i}$ are spin ± 1 parameters which describe the dipole leakage from second order temperature. In general, $\tilde{S}$ will be used for systematics of non-linear response and distinguish from linear systematics.

The calculation for the spurious bispectrum distorted by linear instrumental systematics involving polarization field. So, the distorted polarization E-mode from linear systematics (5.11,5.12) is (SU, 2010)

$$
E(\mathbf{l})^{obs} = \int d\hat{\mathbf{n}}[\tilde{Q}^{obs}(\hat{\mathbf{n}})\cos(2\phi_1) - \tilde{U}^{obs}(\hat{\mathbf{n}})\sin(2\phi_1)]e^{-i\mathbf{l}\cdot\hat{\mathbf{n}}}.
\tag{5.14}
$$

And in the presence of non-linear systematic fields, the observed E-polarization is the leakage from second order temperature to E-polarization, which is the dominant systematics that can potentially generate bias bispectrum detection. The non-linear monopoles are responsible for generating new bispectrum, as for any correlation between linear and non-linear systematics (SU, 2010),

$$
E(\mathbf{l})^{obs} = E(\mathbf{l})^{obs} + \int \frac{d^2\mathbf{l}'}{(2\pi)^2}\frac{d^2\mathbf{l}''}{(2\pi)^2}\tilde{S}(\mathbf{l} - \mathbf{l}' - \mathbf{l}'')\tilde{T}(\mathbf{l}')\tilde{T}(\mathbf{l}'')W_E^{\tilde{S}}(\mathbf{l}, \mathbf{l}', \mathbf{l}'').
\tag{5.15}
$$

here the window function given by $W_E^{\tilde{S}}(\mathbf{l}, \mathbf{l}', \mathbf{l}'')$ contains all the non-linear systematic responses. In contrast to temperate bispectrum case, the polarization contains many cross-correlations between linear $(a, \omega, f_1, f_2, p_1, p_2, \gamma_1, \gamma_2, d_1, d_2, q)$ and non-linear $(\tilde{\gamma_1}, \tilde{\gamma_2}, \tilde{d_1}, \tilde{d_2}, q)$ systematics.

Then, the total observed bispectrum $B_{(\mathbf{l}_1,\mathbf{l}_2,\mathbf{l}_3)}^{XYZ,\,obs}$, including both systematics induced and distorted contributions, is (SU, 2010)

$$
B_{(\mathbf{l}_1,\mathbf{l}_2,\mathbf{l}_3)}^{XYZ,\,obs} = B_{(\mathbf{l}_1,\mathbf{l}_2,\mathbf{l}_3)}^{XYZ,\,primordial} + \sum_{S} B_{(\mathbf{l}_1,\mathbf{l}_2,\mathbf{l}_3)}^{XYZ,\,dist} + \sum_{\tilde{S}} B_{(\mathbf{l}_1,\mathbf{l}_2,\mathbf{l}_3)}^{XYZ,\,bias}.
\tag{5.16}
$$

as the temperature induced systematics, the bispectrum has a contribution from the primordial signal, a bias bispectrum that comes from non-linear systematics, and a distortion term that comes from linear systematics. Even though, bolometers systematics aren't as well understood as radiometers. The reduction of its residuals have been made significant progress in the last release of Planck's data (Planck Collaboration, 2018a).

The main goal of the present work is to search for NG in the CMB data. In order to accomplish this task, we have employed a series of estimators that are sensitive to deviations in the Gaussian distribution.

The data used in this work was provided by Planck satellite in its second public release, which was published after 50 months[1] of operation. By then, the mission had already achieved many of its objectives and more as, i.e. it had updated the constrains on the cosmological parameters and on inflation, catalogued and characterized the emission from Galactic and extragalactic foregrounds and reduced the instrumental systematic effects (Planck Collaboration, 2015a). The information was then processed in the CMB maps by using different separation techniques, such as Commander, NILC, Sevem and SMICA (Planck Collaboration, 2016a). The diffusion component separation process resulted in four almost full sky foreground-cleaned CMB maps, and each component possesses its own confidence mask. See figure 6.1 for example. In other words, the mask represents the most likely region where foreground contamination can be found for each component separation technique.

In this work, the simulated maps are a product of the ACT team and are available online on LAMBDA website. They were produced from the cosmological parameters of the WMAP 5-year parameters measumrents in six bands, from 30 to 350 GHz (DUNKLEY, 2008; SEHGAL, 2009). They are essential to this work because they calibrate the sensitivity of the estimators. We have used the maps that have been produced in two types: unlensed and lensed.

This chapter is dedicated to describe the NG estimators that will be used in this work.

6.1 SPHERICAL CAPS TECHNIQUE

The CMB celestial sphere can be divided homogeneously into spherical caps of same area and aperture γ, $\Omega_j = \Omega(\theta_j, \phi_j) \in \mathbb{S}^2$, with center at the jth pixel, $j = 1...N_s$, where (θ_j, ϕ_j) are the angular coordinates of the jth pixel and N_s is the number of spherical caps. The equal division of the celestial sphere and the coordinate of their centers were defined using HEALPix pixalization scheme (GÓRSKI, 2005).

According to the HEALPix pixalization scheme, the foreground-cleaned maps have a total amount of 50,331,648 pixels. The spherical cap technique employed here has the objective of selecting a determined amount of pixels in each spherical cap. Then, these pixels will be used for further calculations.

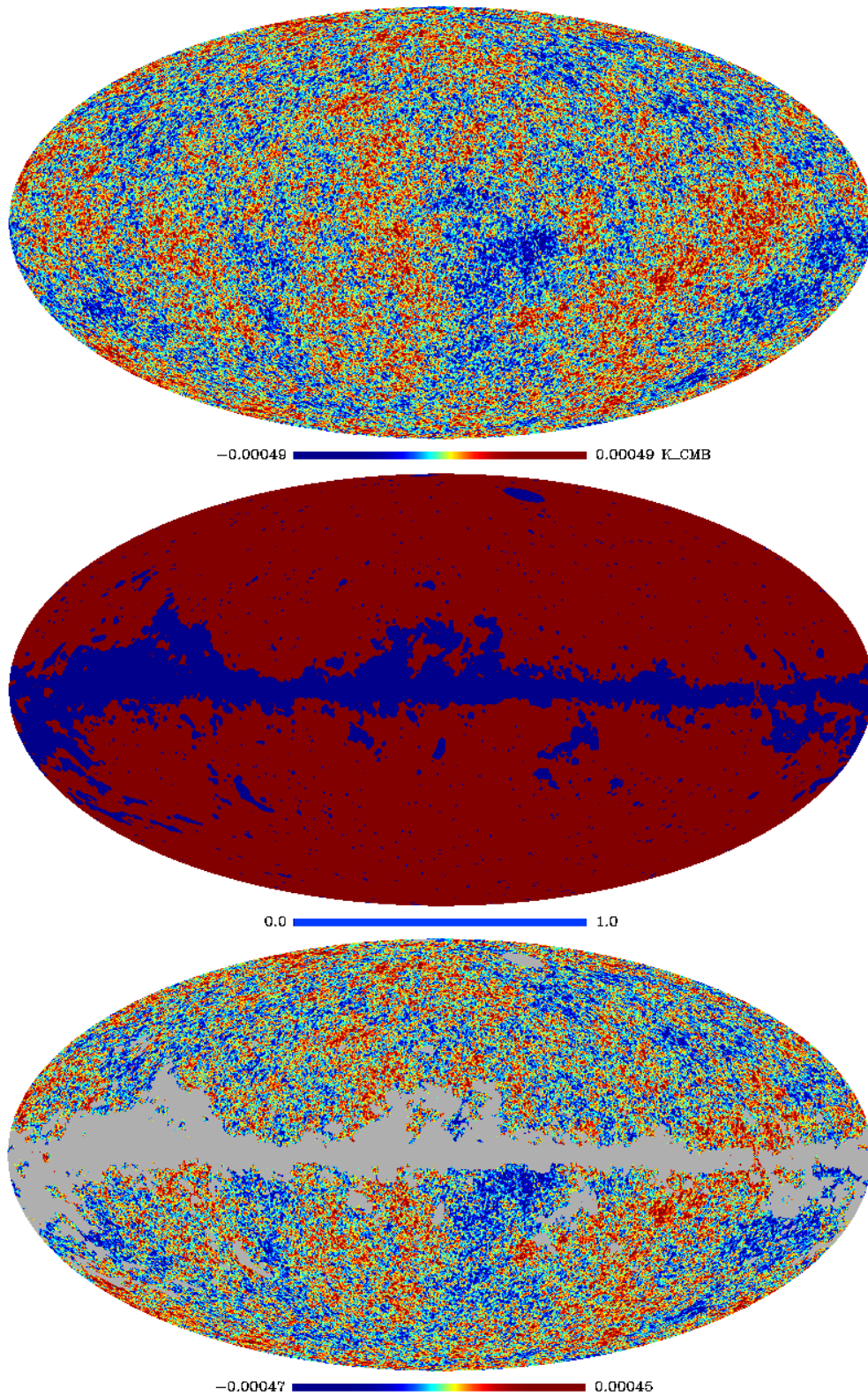[1] Available at the Legacy Archive for Microwave Background Data Analysis (LAMBDA) website

Figure 6.1: Illustration of the component-separation products (Commander): an almost full sky projection of the foreground-cleaned CMB map (*top*), the confidence mask of the Commander component (*middle*), and the application of the mask on the foreground-cleaned map (bottom). For simplification, the other components are not shown.

50

6.2 MOMENTA ESTIMATOR

The goal here is to construct non-Gaussian estimators from statistical measurements and their associated maps, which can be calculated from either real or simulated CMB temperature maps (BERNUI, 2009). The process is done by accessing the deviation from Gaussianity of the CMB temperature fluctuations by calculating the variance V, the skewness S and the kurtosis K. In other words, they measure the local variance in the direction (θ, ϕ), the symmetry about the mean temperature and the non-Gaussian degree of peakness of the temperature distribution, respectively.

The momenta maps can be created from either real or simulated CMB maps. By making use of the spherical cap technique, inside each cap there is a collection of pixels with different temperatures. The statistical data inside them can be calculated by (BERNUI, 2010; BERNUI, 2014)

$$V_j = \frac{1}{N_p} \sum_{i=1}^{N_p} \left(T_j^i - \bar{T}_j \right)^2 = \sigma_j^2 \tag{6.1}$$

$$S_j = \frac{1}{N_p \sigma_j^3} \sum_{i=1}^{N_p} \left(T_j^i - \bar{T}_j \right)^3 \tag{6.2}$$

$$K_j = \frac{1}{N_p \sigma_j^4} \sum_{i=1}^{N_p} \left(T_j^i - \bar{T}_j \right)^4 - 3 \tag{6.3}$$

where N_p is the number of pixels in the jth cap, T_j^i is the temperature at the ith pixel and $\bar{T}_j$ is the mean temperature of the jth cap. The momenta maps are done after patching together the whole set of values from V_j, S_j and K_j in a sphere with N_s pixels. The *mollweide*[2] projection of this sphere is termed as the statistical measurement from which it was created. The coloured celestial sphere (Fig. 7.1) is the final product of the estimators.

Previous work have downgraded the foreground-cleaned maps prior to their use, from $N_{side} = 2048$ to $N_{side} = 512$, and applied the results in a new map of resolution of $N_{side} = 4$ or 16 (BERNUI, 2009,2010,2012,2014). In contrast to their work, our analyses did not involve downgrading the resolution of the foreground-cleaned maps. That is, the resolution was kept at $N_{side} = 2048$, which required more computational time. Moreover, we have increased the resolution of the results map to $N_{side} = 32$, which allows us to have a more detailed perspective of the data. The estimator was applied in the maps in four different apertures, from 10 to 90 degrees. In figures (7.5-7.7), we present the four foreground-cleaned momenta maps processed in a resolution of $N_{side} = 32$. However, we have only shown the momenta whose aperture is of $90°$. This is because, smaller caps near (or even inside) the masked region introduce additional statistical noise as compared to caps that aren't. In these cases, the statistical data inside the cap is performed with fewer pixels, which provides a wrong sampling of the map. As an illustration,

---

[2]The mollweide projection provides a full sky map projection of equal-area and pseudo-cylindrical of HEALPix maps.

figure (7.2) shows simulated data with caps having aperture smaller than $90°$, thus it shows higher statistical values.

In the latest studies on the skewness and kurtosis estimators, these have been explored more extensively than variance's. In 2009, Bernui has presented them as NG estimators for the WMAP three and five years data (BERNUI, 2009). They found some level of foreground contamination in the WMAP maps. Additionally, their analysis also confirmed the maps to be Gaussian, in agreement with the WMAP team and others. In 2010, the estimator was applied to the foreground-reduced maps from WMAP five and seven years data (BERNUI, 2010). Hence, they found significant deviation from Gaussianity which varied with the foreground-reduced procedure. Then, in 2012, a study of the sensitivity, power and limitations of the estimators was done (BERNUI, 2012). For that, they created a series of simulations with different amounts of primordial NG of local type, which neither of the estimators are sensitive to. In conclusion, their previous results indicate that the NG captured was of non-primordial origin.

Regarding the variance estimator, recent studies have shown a strong dipole signal in all maps used (BERNUI, 2014). They noticed that this dipolar structure did not come from foreground contamination, because the different CMB frequencies produced similar direction and intensity. Furthermore, they suggested the removal of the quadrupole and octapole from the analysis, due to the lower intensity of the real data compared to simulations. Bernui and his team said that it is worth looking into it because these results have a higher confidence level than real data.

6.3 MINKOWSKI FUNCTIONALS

The Minkowski functionals present many advantages as compared to other statistical estimators. One of them is their versatility in detecting diverse types of NG without a previous knowledge of their features, such as angular dependence or intensity, and also because they can be efficiently applied in masked skies or small regions of the CMB sphere (NOVAES, 2014).

The CMB maps have morphological properties that are invariant under translation and rotation, and that are additive. They are a 2-dimensional (2-D) map where its temperature field is defined on a sphere with zero mean and variance σ^2. Regarding these features, there's a branch of mathematics that provides a natural tool for this characterization, which says that all the morphological properties of any pattern in d-dimensional space can be described using $d + 1$ Minkowski Functionals (MFs) (MINKOWSKI, 1903). This tool is able to test non-Gaussian attributes by assessing the properties of connected regions in the map (KOMATSU, 2003).

Considering a connected region R_i in a CMB pixelized sphere of the excursion set with $\nu(\theta, \phi) \equiv (\Delta T(\theta, \phi)/T)/\sigma > \nu_t$, where $\nu(\theta, \phi)$ is the measure and ν_t is the threshold. In the 2-D case, only three parameters are to be considered: the area of the region a_i, the length of its contour l_i and the number of holes in the area n_i. These are the three partial MFs for a 2-D map. Their correspondent global MFs are obtained by computing all the disjoint regions of the

excursion set as, i.e. taking the sum of each parameter $A = \sum a_i$, $L = \sum l_i$ and $G = \sum g_i$: "the number of isolated $\nu > \nu_t$ regions" $-$ "the number of isolated $\nu < \nu_t$ regions". That is the difference between the number of hot spots (high threshold) and the number of cold spots (low threshold). Therefore, the global MFs of Gaussian fields are (KOMATSU, 2003; ERIKSEN, 2004):

$$A(\nu) = \frac{1}{4\pi} \int_{\Sigma} d\Omega = \sum a_i; \qquad (6.4)$$

$$L(\nu) = \frac{1}{4\pi} \frac{1}{4} \int_{\partial\Sigma} dl = \sum l_i; \qquad (6.5)$$

$$G(\nu) = \frac{1}{4\pi} \frac{1}{2\pi} \int_{\partial\Sigma} \kappa dl = \sum g_i = n_{hot} - n_{cold}. \qquad (6.6)$$

where Σ is the set of regions with $\nu > \nu_t$, $\partial\Sigma$ is the boundary of Σ and $d\Omega$ and dl are elements of solid angle and line, respectively. In the genus definition, the quantity κ is the geodesic curvature. The MFs are calculated from a given threshold ν_t.

Previous studies with the MF show that they are good at finding NG in the CMB map. Komatsu has found that the MF had good agreement with the bispectrum results (KOMATSU, 2003). In a more recent study, which has done a local analysis of the Planck data (NOVAES, 2014b), they divided the sky in 192 regions and used the MF to analyze each one, which resulted in a set of 13 regions with large discrepancies from Gaussianity. These were in good agreement with the Planck Collaboration (2016f) findings and a possible new anomalous region. Nonetheless, they confirmed that the most affected regions are near the Galactic plane, which are more affected due to the foreground component separation process.

7 RESULTS AND DISCUSSION

Our analysis will take place after applying our estimators to the data, which is foreground-cleaned maps from Planck and simulated maps from ACT. First, our standard case comes from a simulated unlensed map, which is the Gaussian case. Also, we did not apply any of the validation masks to it. Furthermore, the foreground-cleaned maps come in a resolution of $N_{side} = 2048$. However, the simulated maps have $N_{side} = 8192$. In order to apply the estimators on the simulated maps, we had to downgrade their resolution by 4. Thus, all the maps analyzed would have the same resolution.

Turning to the application of the momenta estimator, we have created a new map with resolution of $N_{side} = 32$ to collect the results from each spherical cap. This lower resolution map had all of its pixels located by vectors, which were then used in the spherical cap selection technique. The standard case was created in the same manner; see figure 7.1.

For the Minkowski's estimator case, we did not have to create a new map to collect data, because the MF utilizes only the morphological features of the map to create its parameters. The standard case is illustrated in fig. 7.8.

7.1 MOMENTA RESULTS

Let's begin our analysis by saying that both real and simulated maps had all four of the validation masks applied to all of the maps.

First, we present the simulated results, for both unlensed and lensed maps. For simplicity, we only present the maps that had the Commander validation mask applied. However, the simulated in the 6 frequencies behave in similar ways when all four masks are applied. In figures 7.3 and 7.4, it is evident that the momenta in the masked maps behave differently from the standard case in fig. 7.1. This happens because the masking process removed pixels from the simulated maps, which contributed to its Gaussian condition. Thus, the simulated masked maps present the Gaussian condition for masked maps.

Regarding the four foreground-cleaned maps from Planck, these were produced after a component separation process that was supposed to remove all foreground contamination. Each component map had its own validation mask applied to them, see figures 7.5-7.7. Therefore, we can see four maps that are clearly deviating from both Gaussian cases. The contamination in these maps produces non-Gaussianity, which could come from either foreground or instrumental systematics. The latter being an unresolved problem in the data, and the component separation method used in Planck's 2015 data has been improved in the latest release (Planck Collaboration, 2018e).
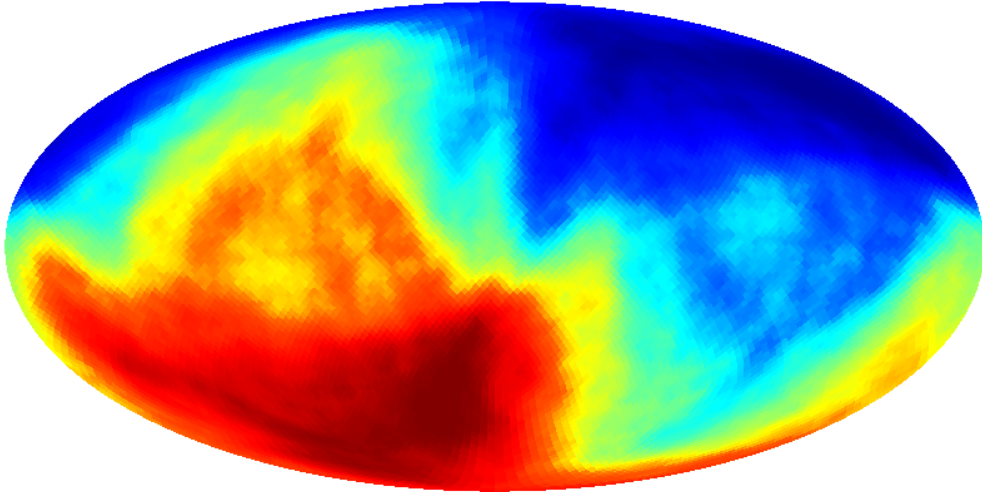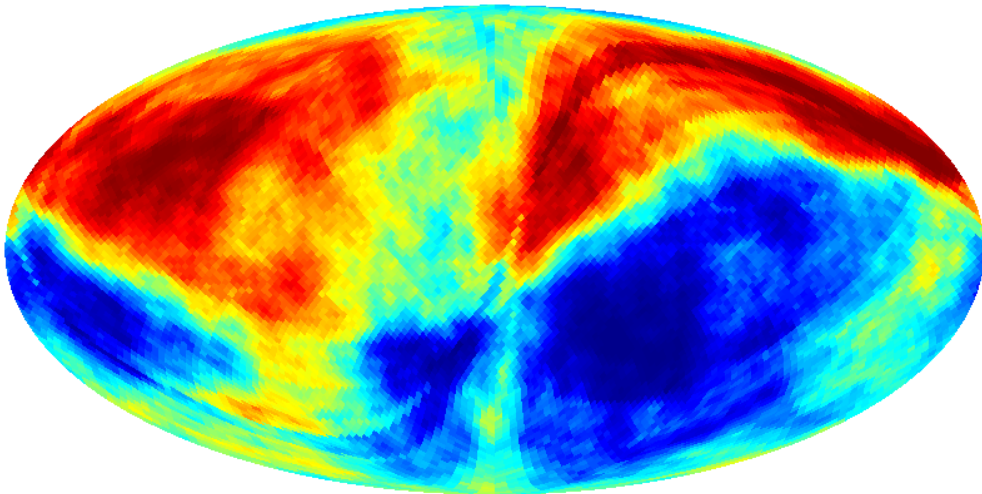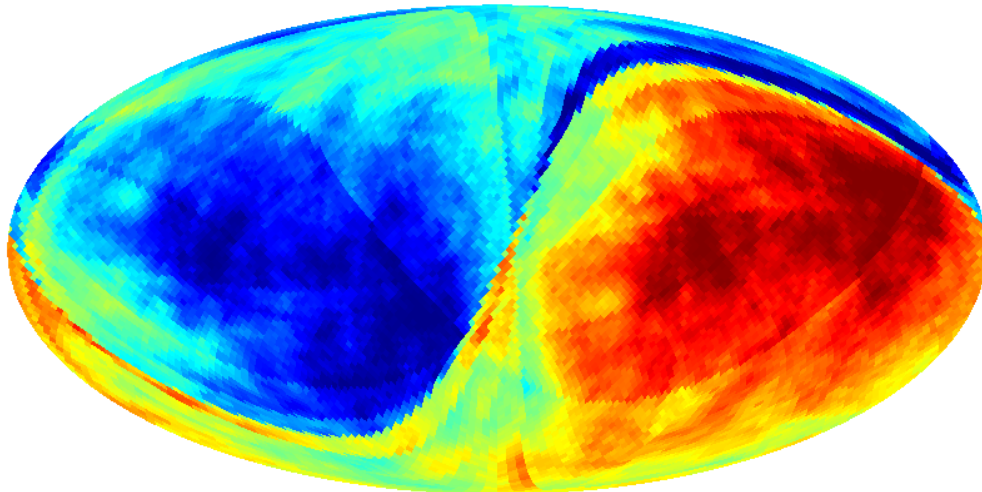
Figure 7.1: Standard case of the momenta estimator applied to a simulated Gaussian map.
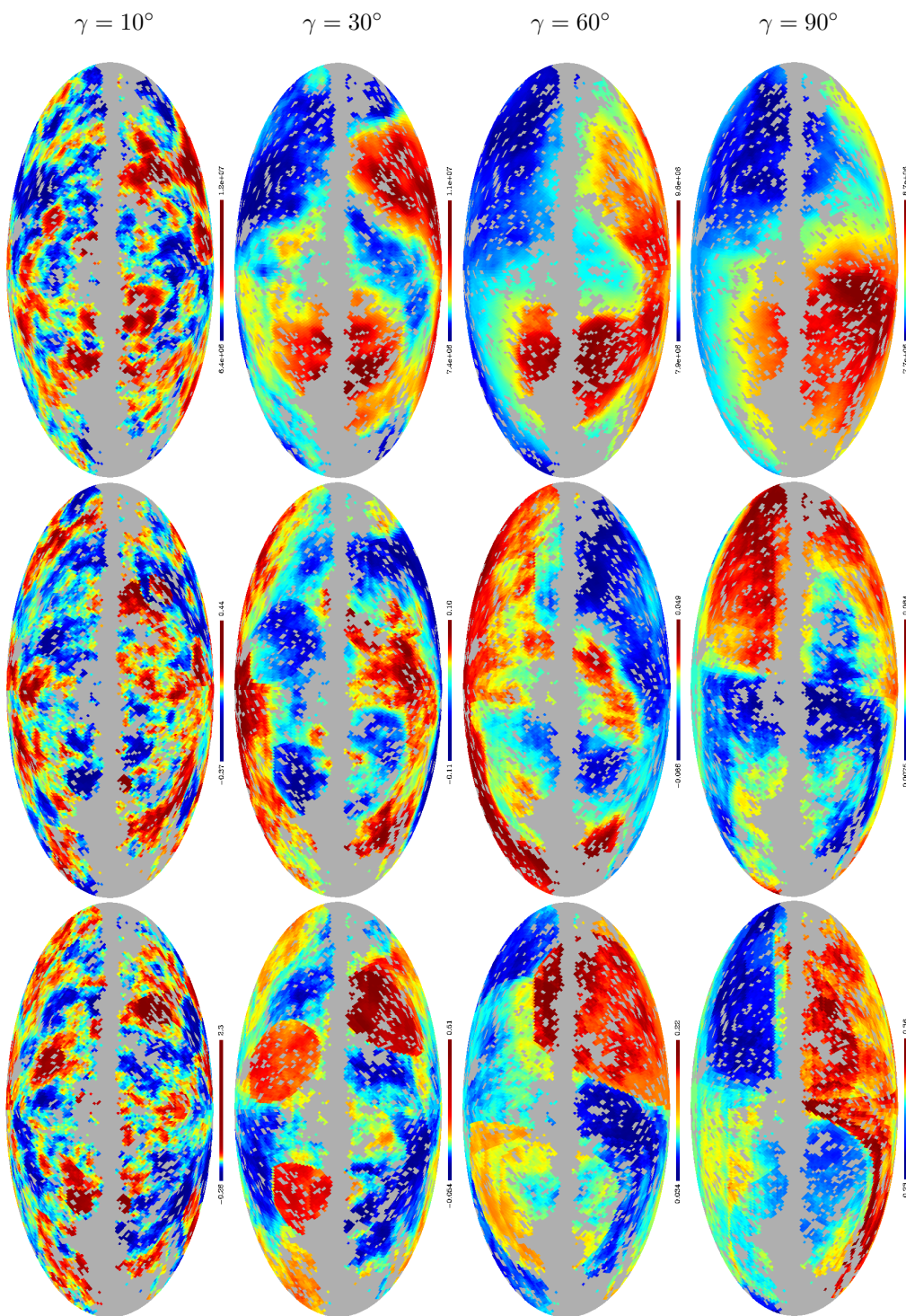
Figure 7.2: Momenta estimator applied to simulated masked maps for different degrees of apertures (from $10°$ to $90°$). The apertures smaller than $90°$ carry larger statistical values, which adds additional noise to the analysis. The momenta maps are divided as: (*top*) Variance, (*middle*) Skewness and (*bottom*) Kurtosis.

Variance Map   Skewness Map   Kurtosis Map

30 GHz   30 GHz   30 GHz

90 GHz   90 GHz   90 GHz

148 GHz   148 GHz   148 GHz

219 GHz   219 GHz   219 GHz

277 GHz   277 GHz   277 GHz

350 GHz   350 GHz   350 GHz
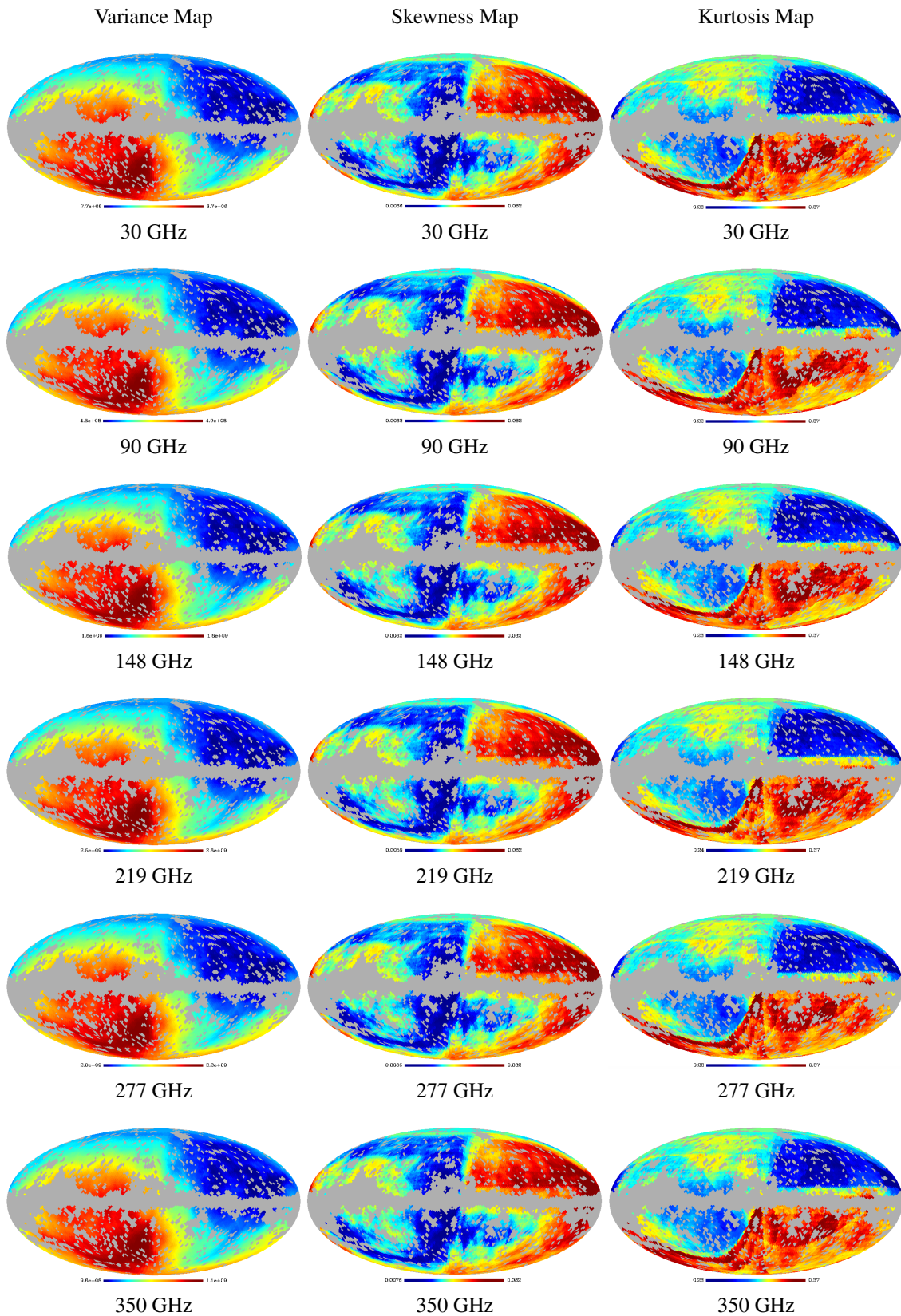
Figure 7.3: Momenta estimator applied to simulated unlensed maps with Commander masks, and aperture of 90 degrees. According to the colour scale, the minimum (maximum) value of a set $\{V_j, S_j, K_j\}$ corresponds to the bluest (reddest) pixel.

57

Variance Map   Skewness Map   Kurtosis Map

30 GHz   30 GHz   30 GHz

90 GHz   90 GHz   90 GHz

148 GHz   148 GHz   148 GHz

219 GHz   219 GHz   219 GHz

277 GHz   277 GHz   277 GHz

350 GHz   350 GHz   350 GHz

Figure 7.4: Momenta estimator applied to simulated lensed maps with Commander masks, and aperture of 90 degrees. According to the colour scale, the minimum (maximum) value of a set $\{V_j, S_j, K_j\}$ corresponds to the bluest (reddest) pixel.

Commander Variance Map

Sevem Variance Map

NILC Variance Map
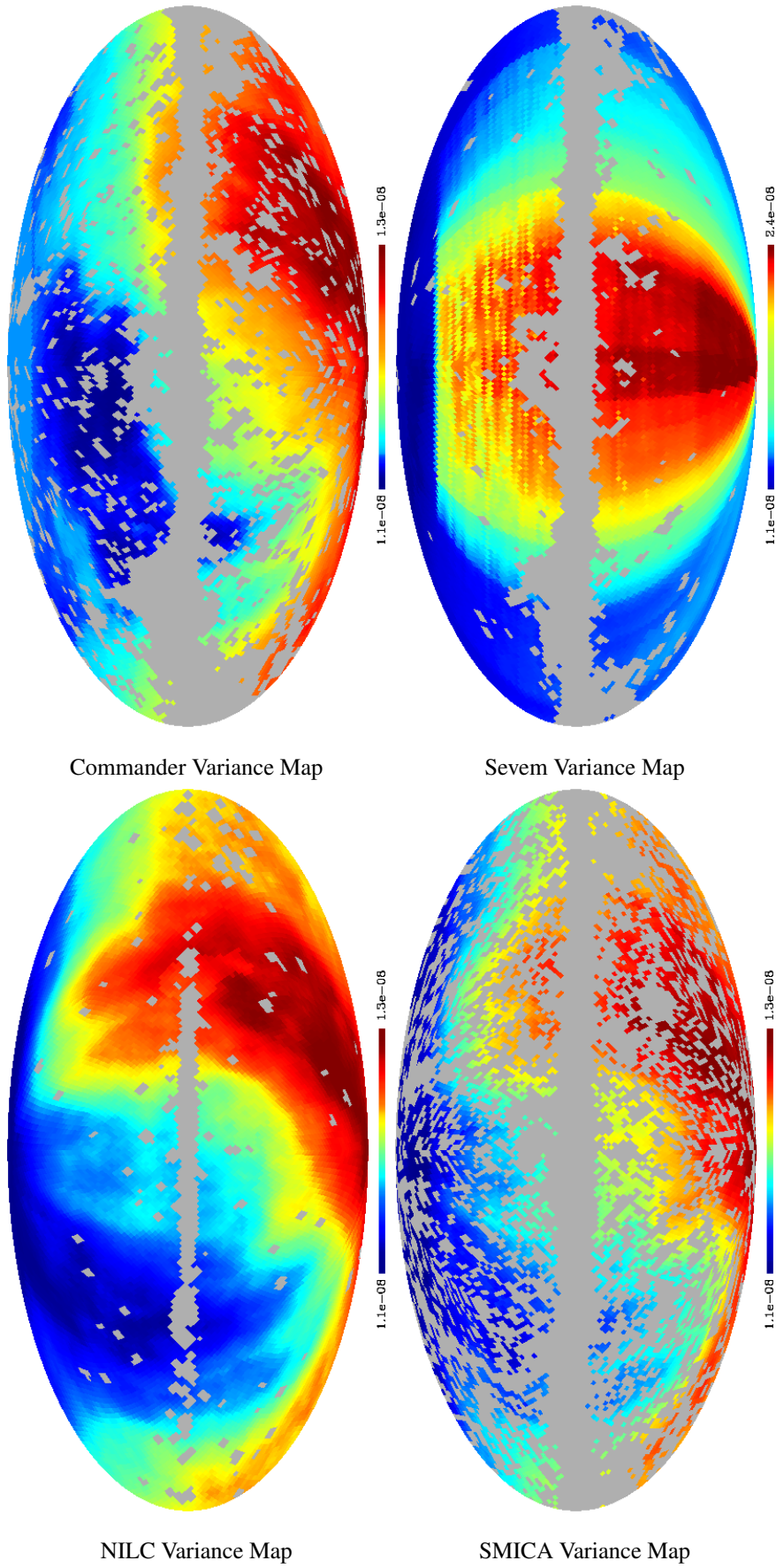
SMICA Variance Map

Figure 7.5: Variance maps applied to the Planck's four foreground-reduced maps. According to the colour scale, the minimum (maximum) value of a set $\{V_j\}$ corresponds to the bluest (reddest) pixel. The momenta maps shown have aperture of 90 degrees, which reduces the statistical noise due to the use of masks in the maps.
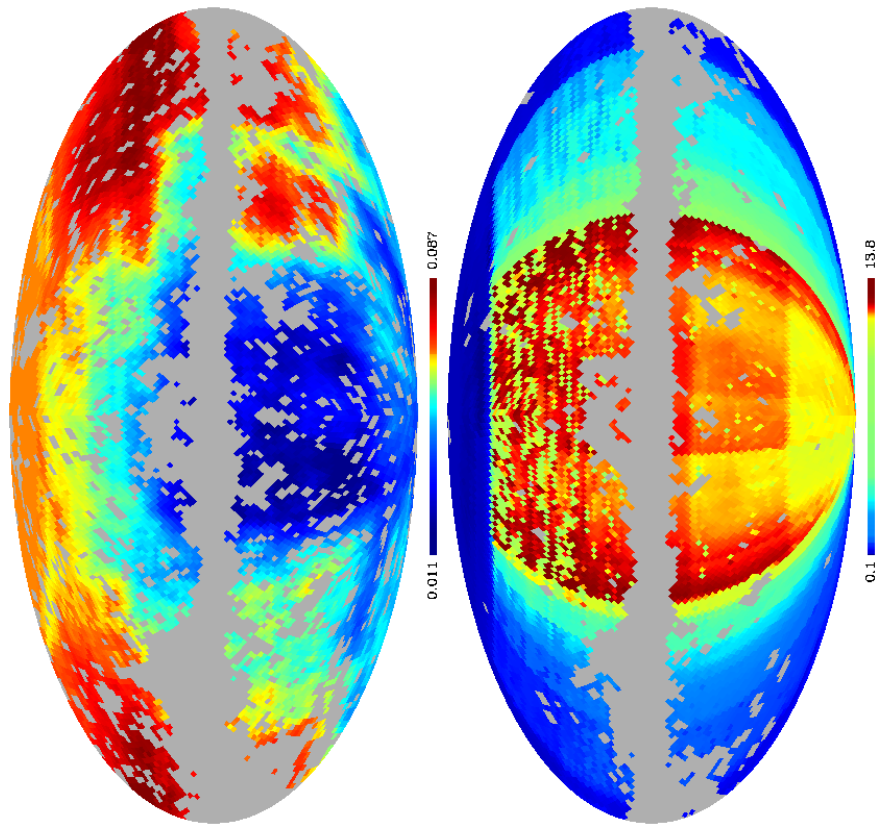
Commander Skewness Map

Sevem Skewness Map
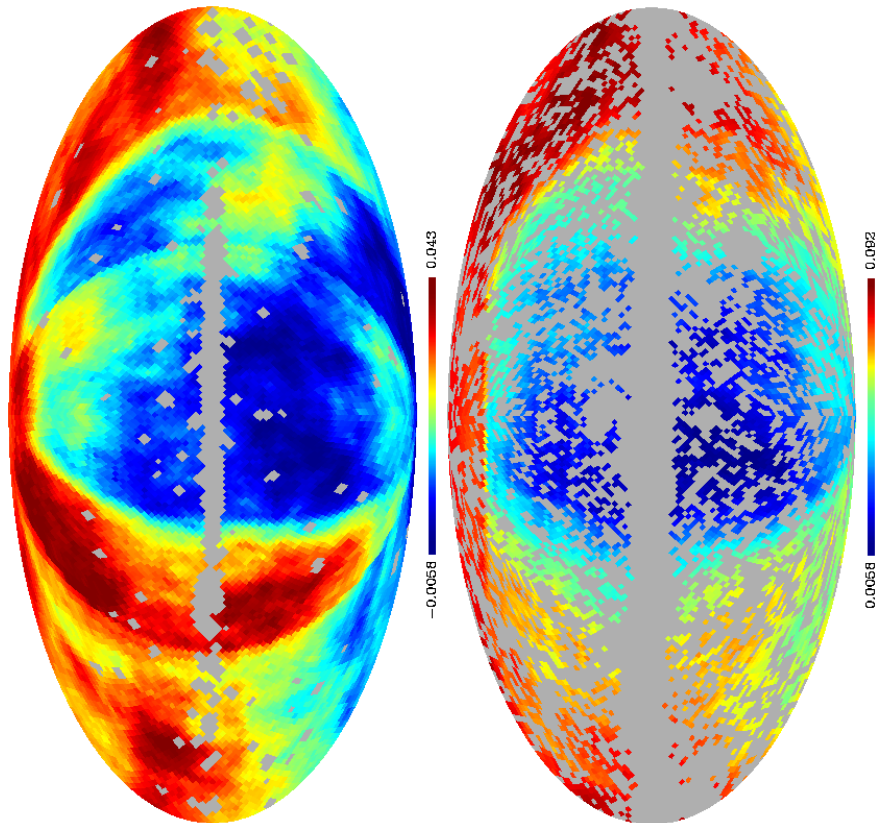
NILC Skewness Map

SMICA Skewness Map

Figure 7.6: Skewness maps applied to the Planck's four foreground-reduced maps. According to the colour scale, the minimum (maximum) value of a set $\{S_j\}$ corresponds to the bluest (reddest) pixel. The momenta maps shown have aperture of 90 degrees, which reduces the statistical noise due to the use of masks in the maps.

Commander Kurtosis Map

Sevem Kurtosis Map

NILC Kurtosis Map

SMICA Kurtosis Map

Figure 7.7: Kurtosis maps applied to the Planck's four foreground-reduced maps. According to the colour scale, the minimum (maximum) value of a set $\{K_j\}$ corresponds to the bluest (reddest) pixel. The momenta maps shown have aperture of 90 degrees, which reduces the statistical noise due to the use of masks in the maps.
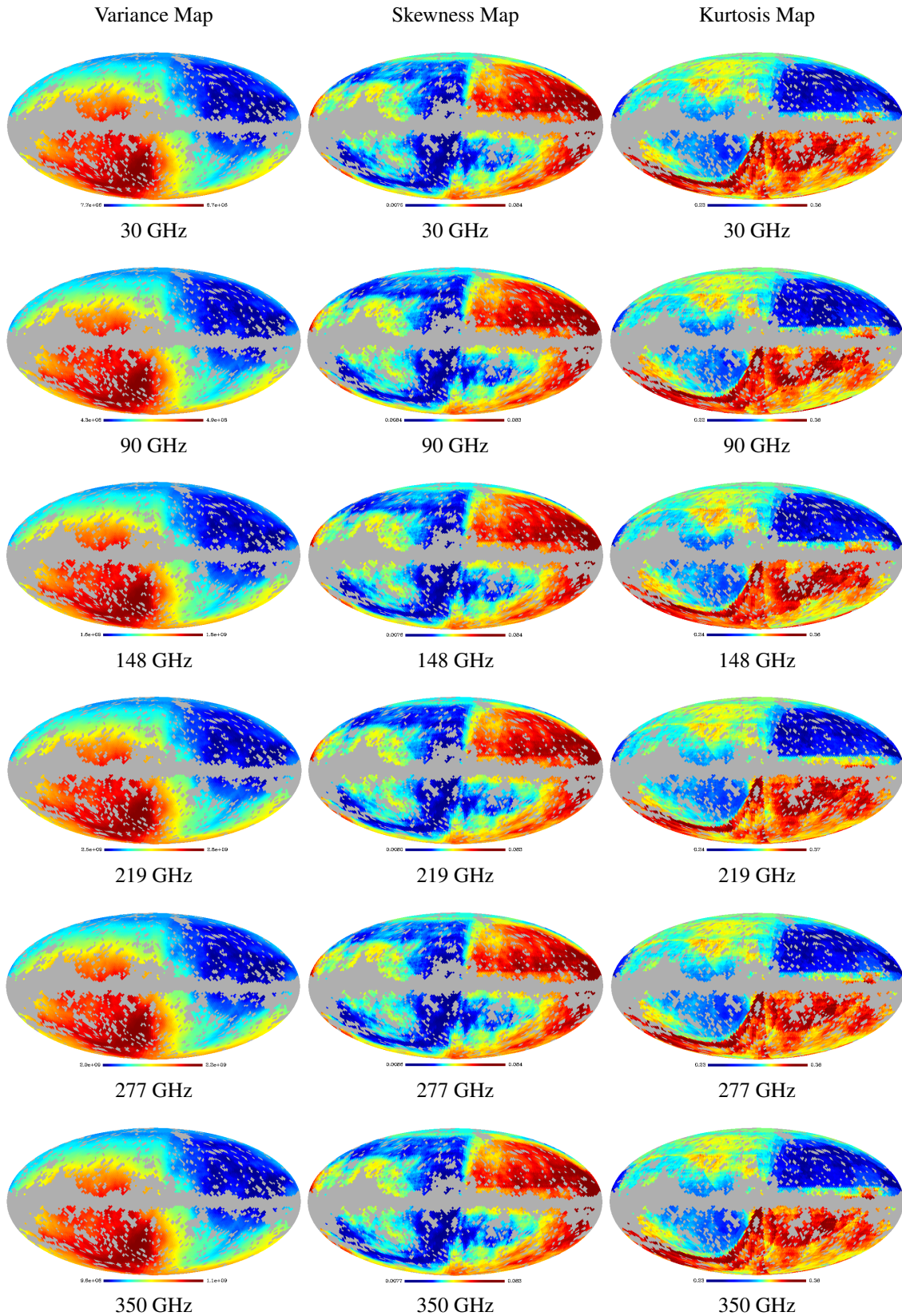
7.2 MINKOWSKI RESULTS
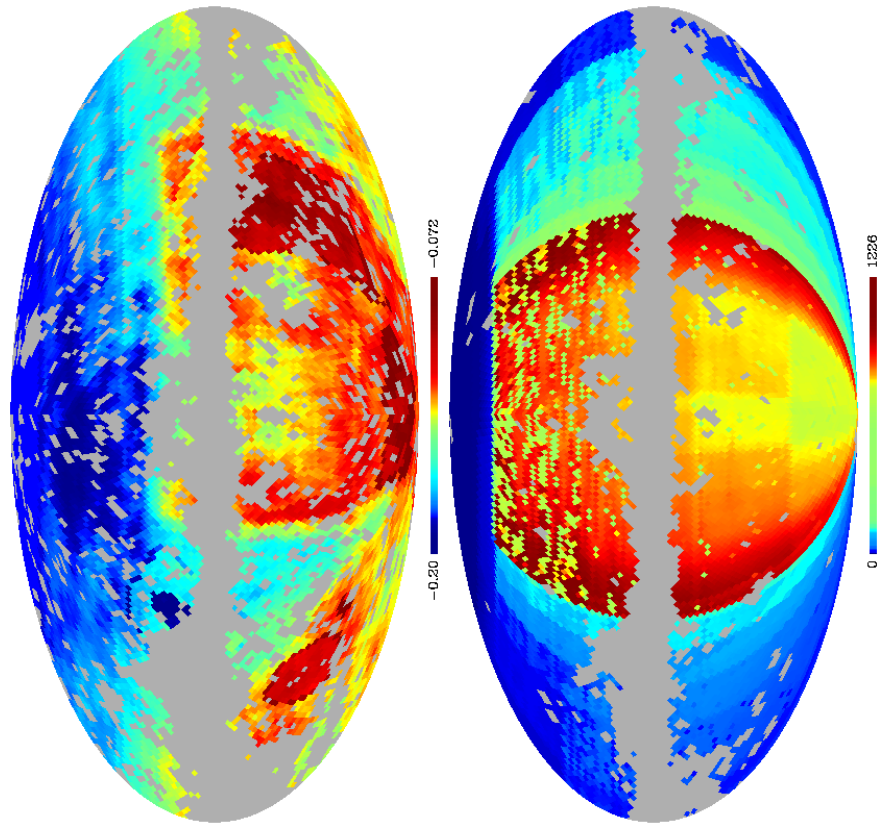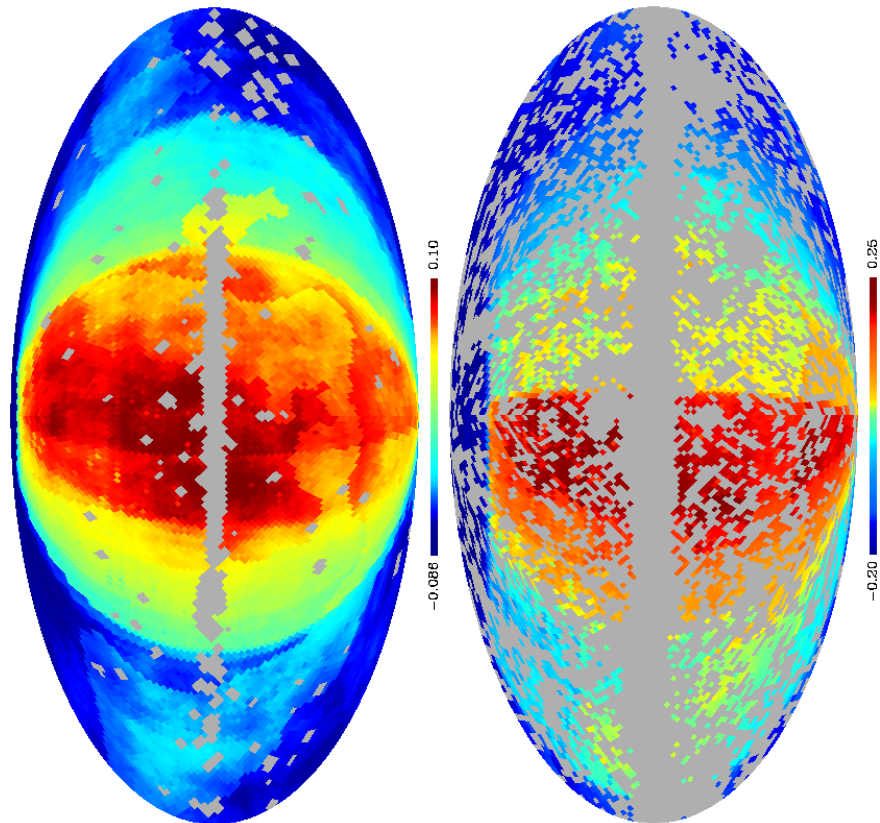
The MF were applied to both real and simulated maps, and they were all masked with the four validation masks. Similar to the momenta results, we will present first the simulated masked data. Furthermore, all the plots have the Gaussian included, which is a red line with plus signs. The application of this estimator presented a similar behaviour for all these maps, and for simplicity, we have decided to only show $1/4$ of the results here.

In the Minkowski application, the simulated masked maps also have part of their pixels erased. In fact, this is more evident than in the momenta case because of the gap in the plot functionals; see figures 7.9 and 7.10. The simulated masked maps slightly diverge from the Gaussian case due to the application of the mask, but it maintains its Gaussian condition.

Now, let's examine the four foregorund-cleaned maps. In figures 7.11-7.16, we can see the 3 MF functionals were plotted and all of them show large deviations from the Gaussian case. Therefore, we can assume that there are still traces of residual contamination in the Planck maps.
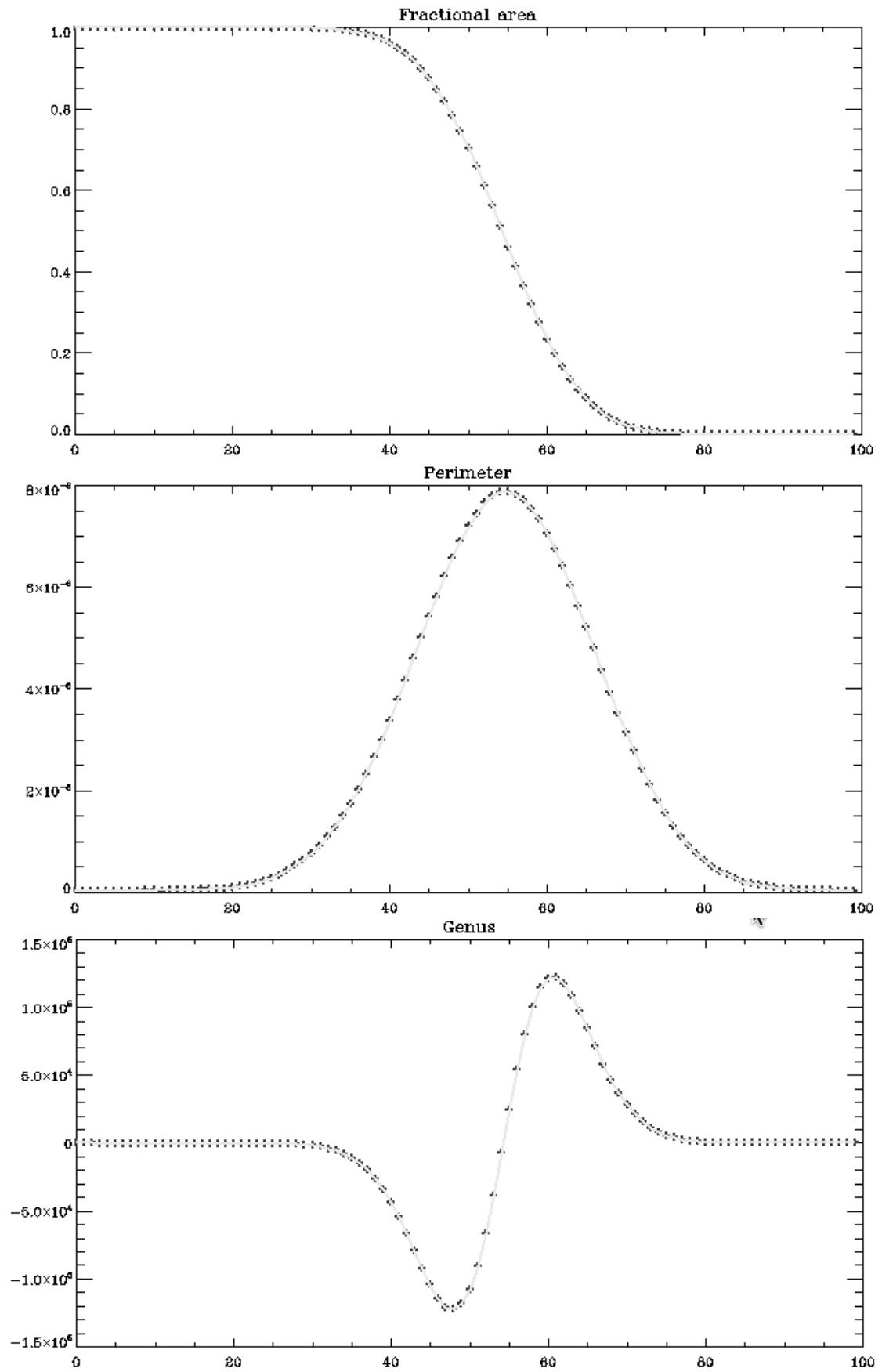
Figure 7.8: Standard case of the Minkowski Functionals estimator applied to the simulated Gaussian maps. The Gaussian case is represented by the solid line (simulated unlensed unmasked map) and by the plus signs (simulated lensed unmasked map)

63

Area	Perimeter	Genus

30 GHz · 30 GHz · 30 GHz

90 GHz · 90 GHz · 90 GHz

148 GHz · 148 GHz · 148 GHz

219 GHz · 219 GHz · 219 GHz

277 GHz · 277 GHz · 277 GHz

350 GHz · 350 GHz · 350 GHz

Figure 7.9: Minkowski Functionals applied to simulated unlensed maps with Commander masks, in six bands. The plot of the MF is represented by the diamonds. The Gaussian case is represented by the red solid line (simulated unlensed unmasked map) and by the plus signs (simulated lensed unmasked map).

Area	Perimeter	Genus
30 GHz	30 GHz	30 GHz
90 GHz	90 GHz	90 GHz
148 GHz	148 GHz	148 GHz
219 GHz	219 GHz	219 GHz
277 GHz	277 GHz	277 GHz
350 GHz	350 GHz	350 GHz

Figure 7.10: Minkowski Functionals applied to simulated lensed maps with Commander masks, in six bands. The plot of the MF is represented by the diamonds. The Gaussian case is represented by the red solid line (simulated unlensed unmasked map) and by the plus signs (simulated lensed unmasked map).

65

Figure 7.11: The Area Minkowski Functional applied to the Planck's foreground-reduced maps (Commander and NILC). The area parameter, A, considers the area of the map. The celestial sphere was divided in pixels with the same area by HEALPix pixelization scheme. These were subdivided into 100 steps of temperature, then plotted in the abscissa and the MF values are plotted in the ordinates. The plot of the MF is represented by the diamonds. The Gaussian case is represented by the red solid line (simulated unlensed unmasked map) and by the plus signs (simulated lensed unmasked map).

Figure 7.12: The Area Minkowski Functional applied to the Planck's foreground-reduced maps (Sevem and SMICA). The area functional, A, considers the area of the map. The plot of the MF is represented by the diamonds. The Gaussian case is represented by the red solid line (simulated unlensed unmasked map) and by the plus signs (simulated lensed unmasked map).
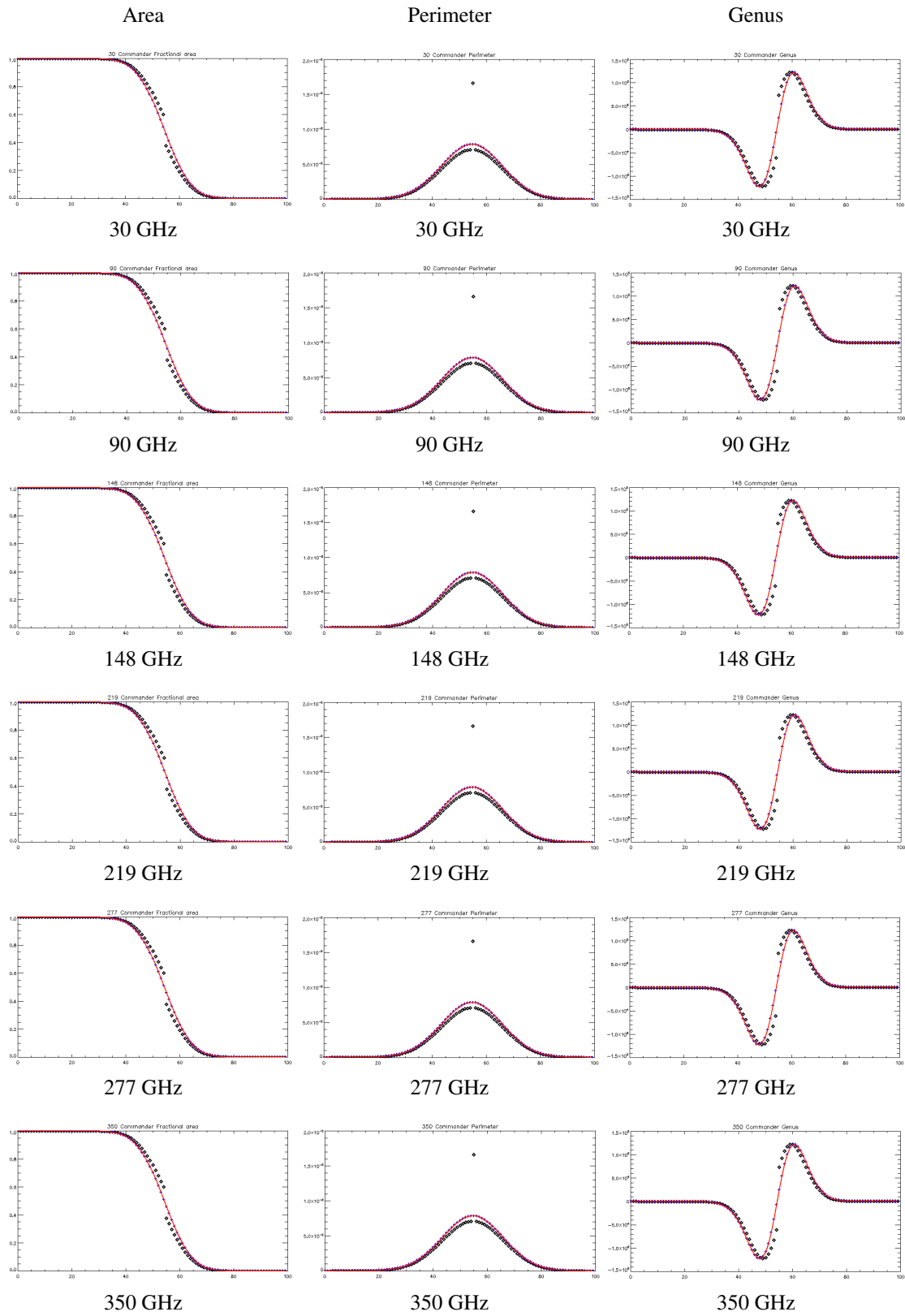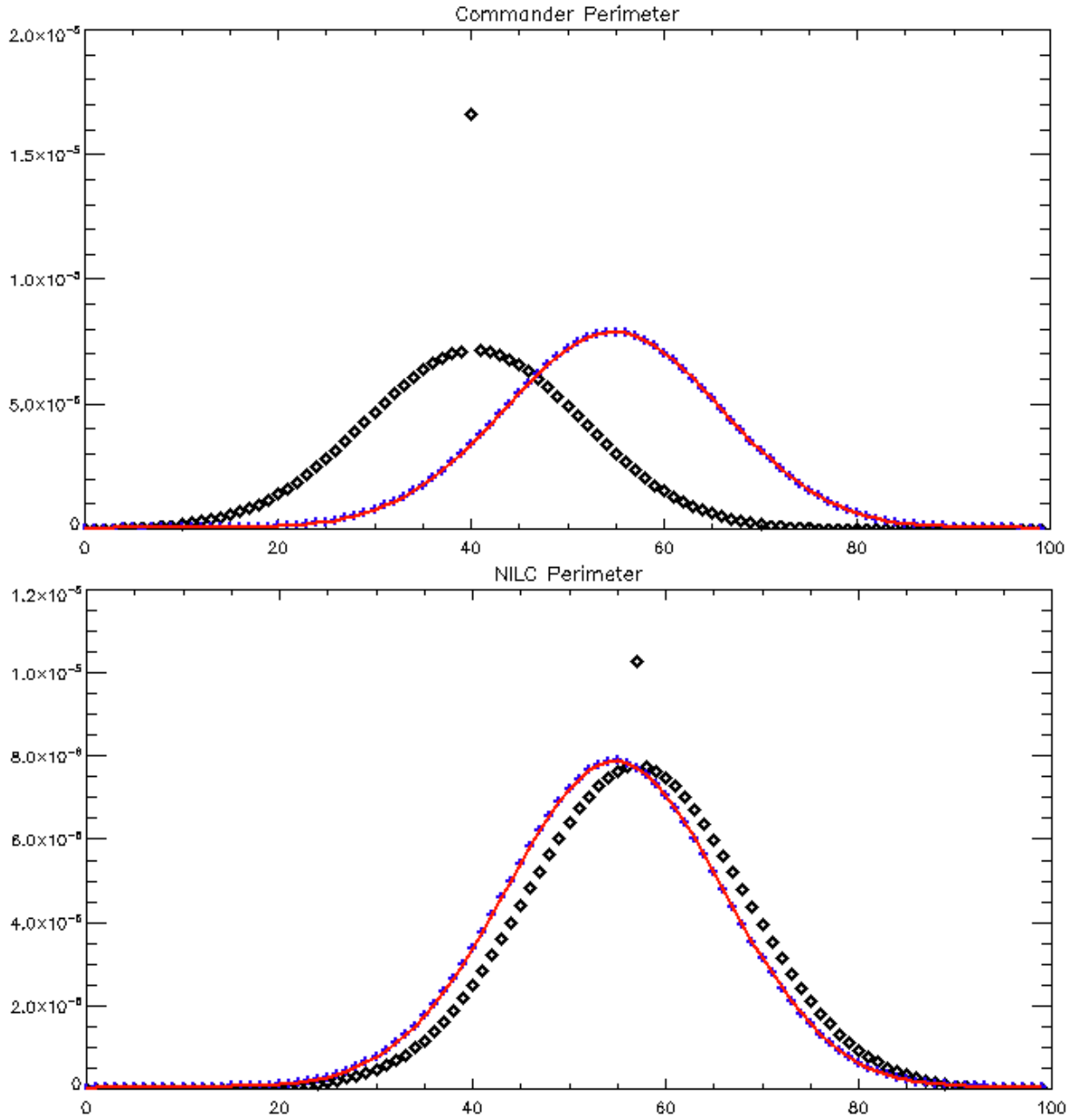
Figure 7.13: The Perimeter Minkowski Functional applied to the Planck's foreground-reduced maps (Commander and NILC). The perimeter functional, L, considers the length of the map's contour. The celestial sphere was divided in pixels with the same area by HEALPix pixelization scheme. These were subdivided into 100 steps of temperature, then plotted in the abscissa and the MF values are plotted in the ordinates. The plot of the MF is represented by the diamonds. The Gaussian case is represented by the red solid line (simulated unlensed unmasked map) and by the plus signs (simulated lensed unmasked map).
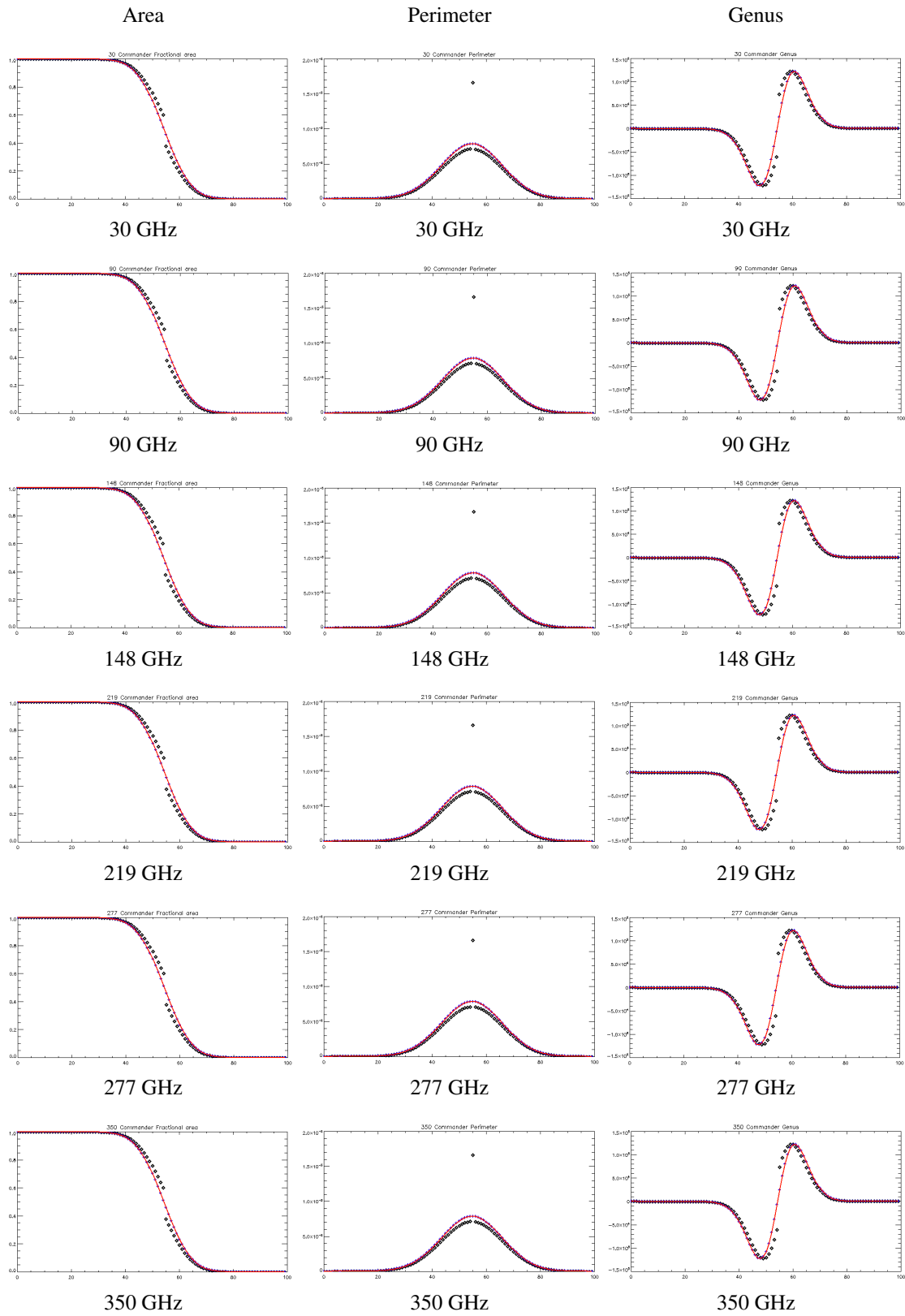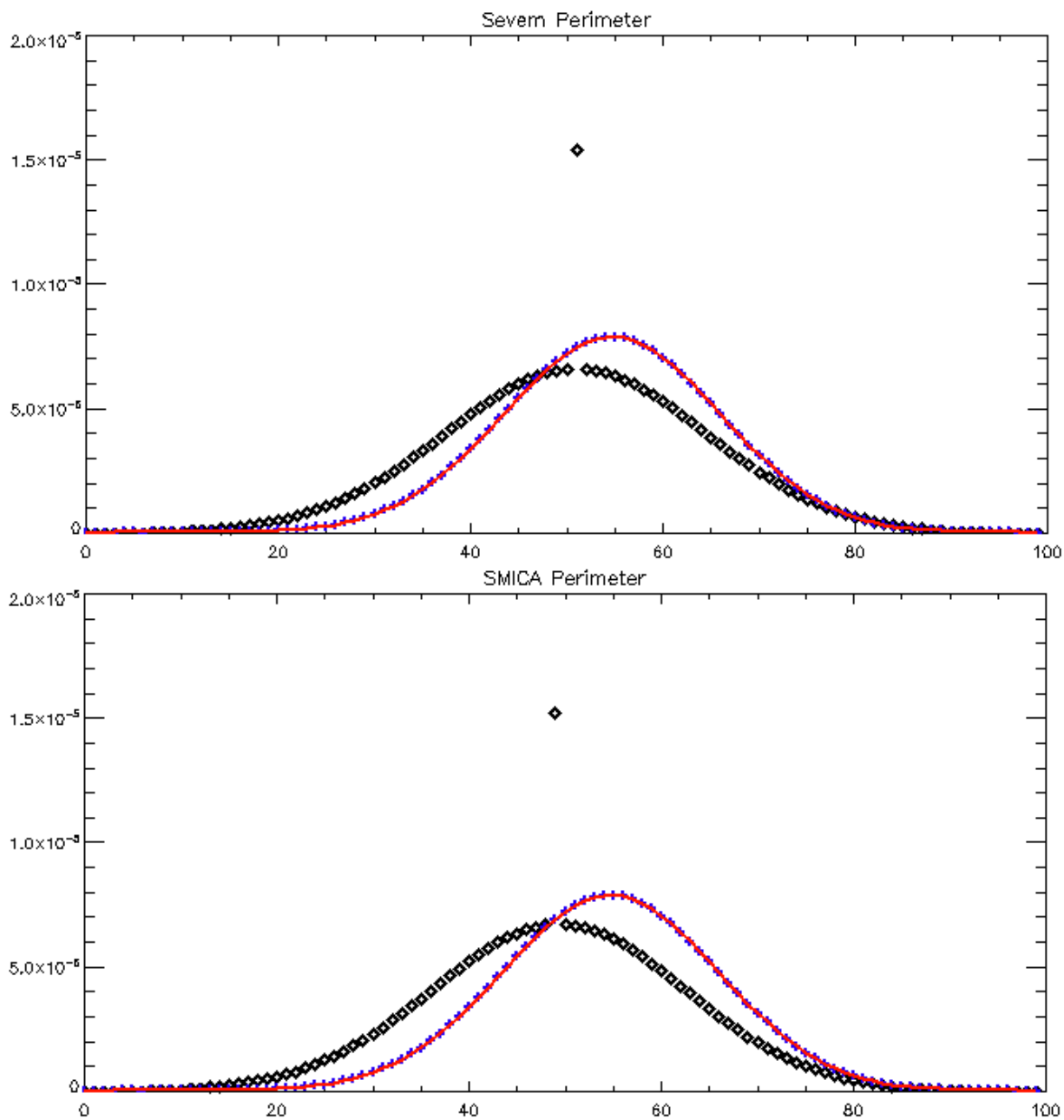
Figure 7.14: The Perimeter Minkowski Functional applied to the Planck's foreground-reduced maps (Sevem and SMICA). The perimeter function, L, considers the length of the map's contour. The plot of the MF is represented by the diamonds. The Gaussian case is represented by the red solid line (simulated unlensed unmasked map) and by the plus signs (simulated lensed unmasked map).
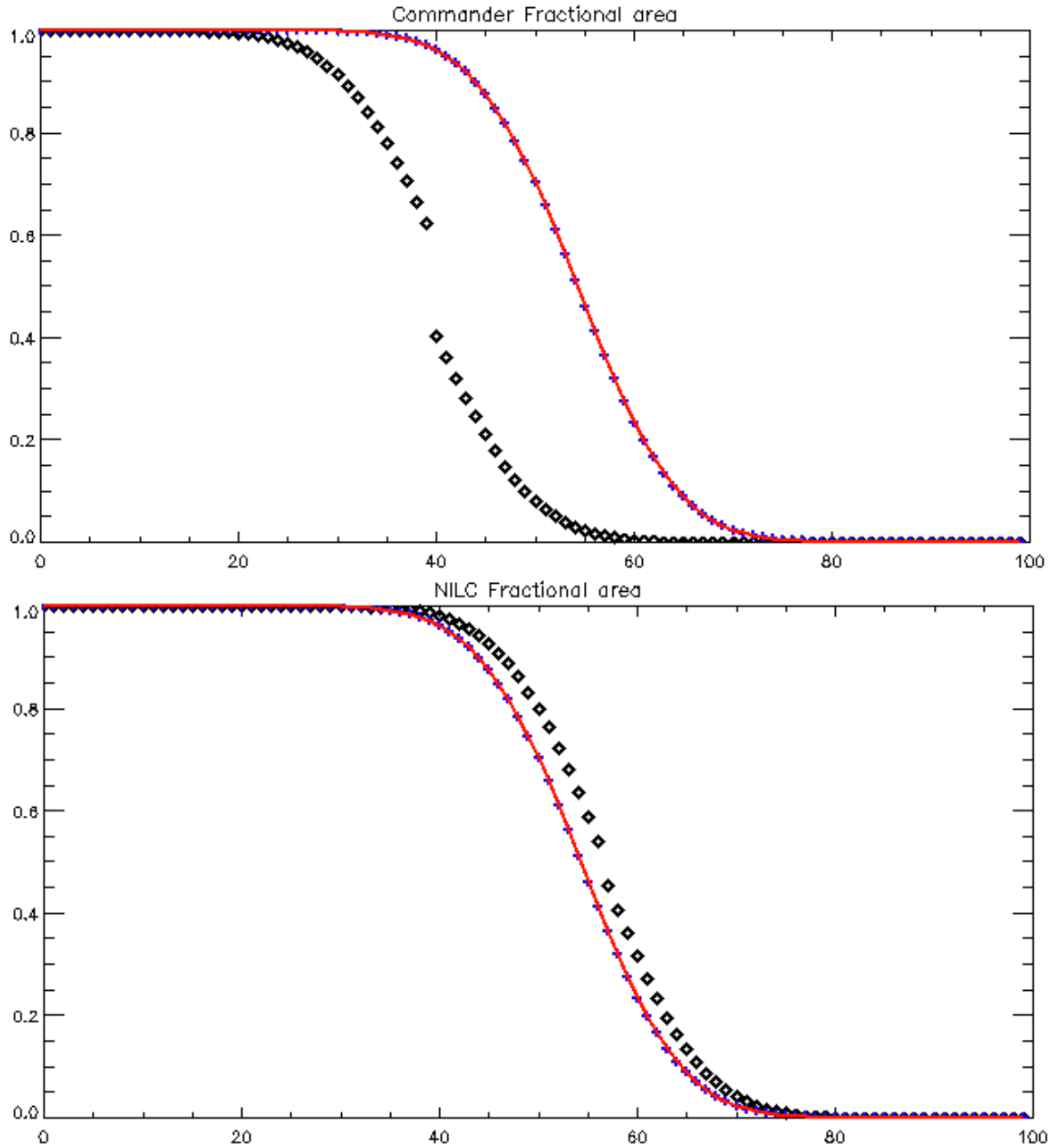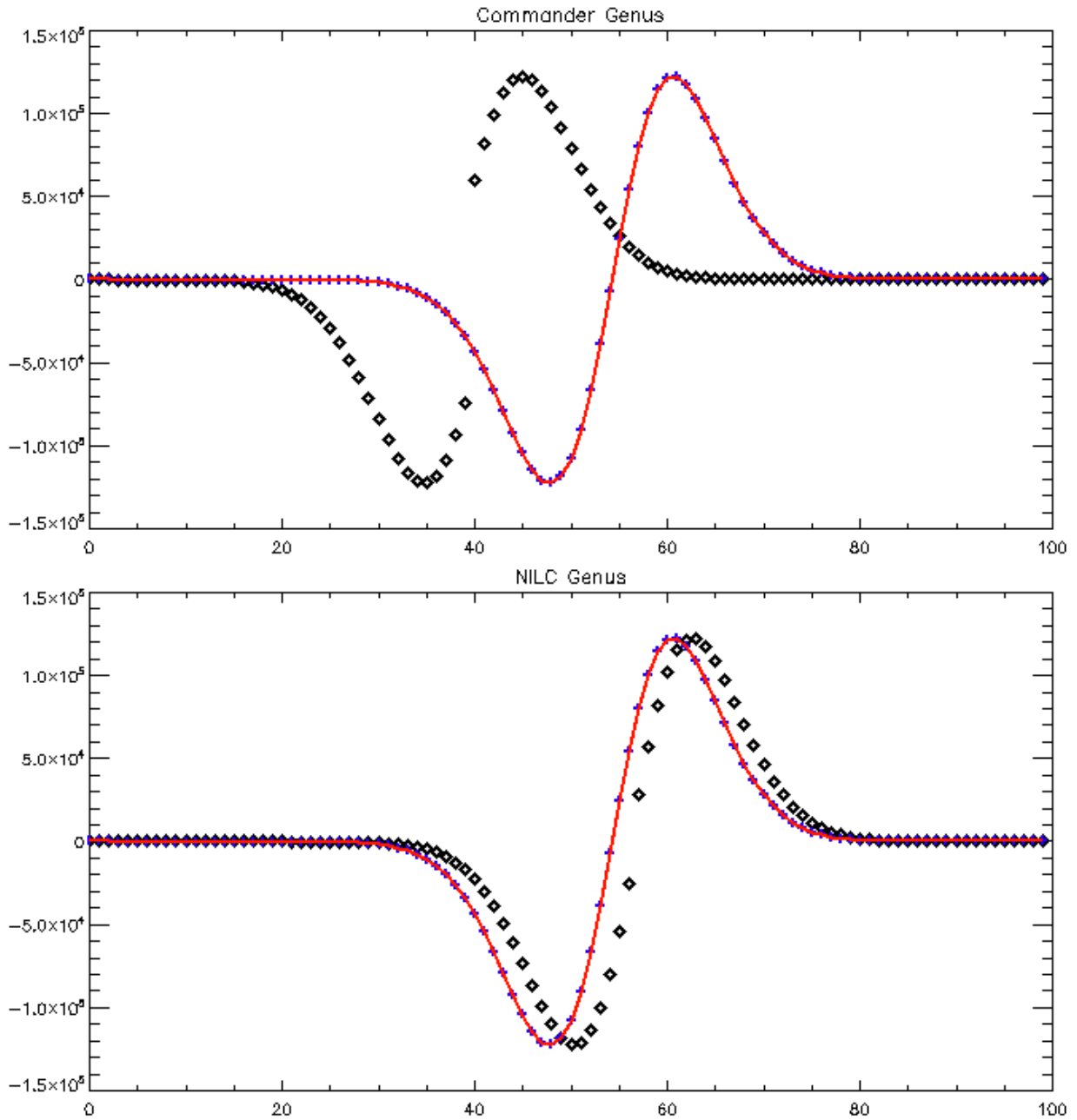
Figure 7.15: The Genus Minkowski Functional applied to the Planck's foreground-reduced maps (Commander and NILC). The Genus function, G, considers the difference between the number of hot spots and the number of cold spots in the map. The celestial sphere was divided in pixels with the same area by HEALPix pixelization scheme. These were subdivided into 100 steps of temperature, then plotted in the abscissa and the MF values are plotted in the ordinates. The plot of the MF is represented by the diamonds. The Gaussian case is represented by the red solid line (simulated unlensed unmasked map) and by the plus signs (simulated lensed unmasked map).
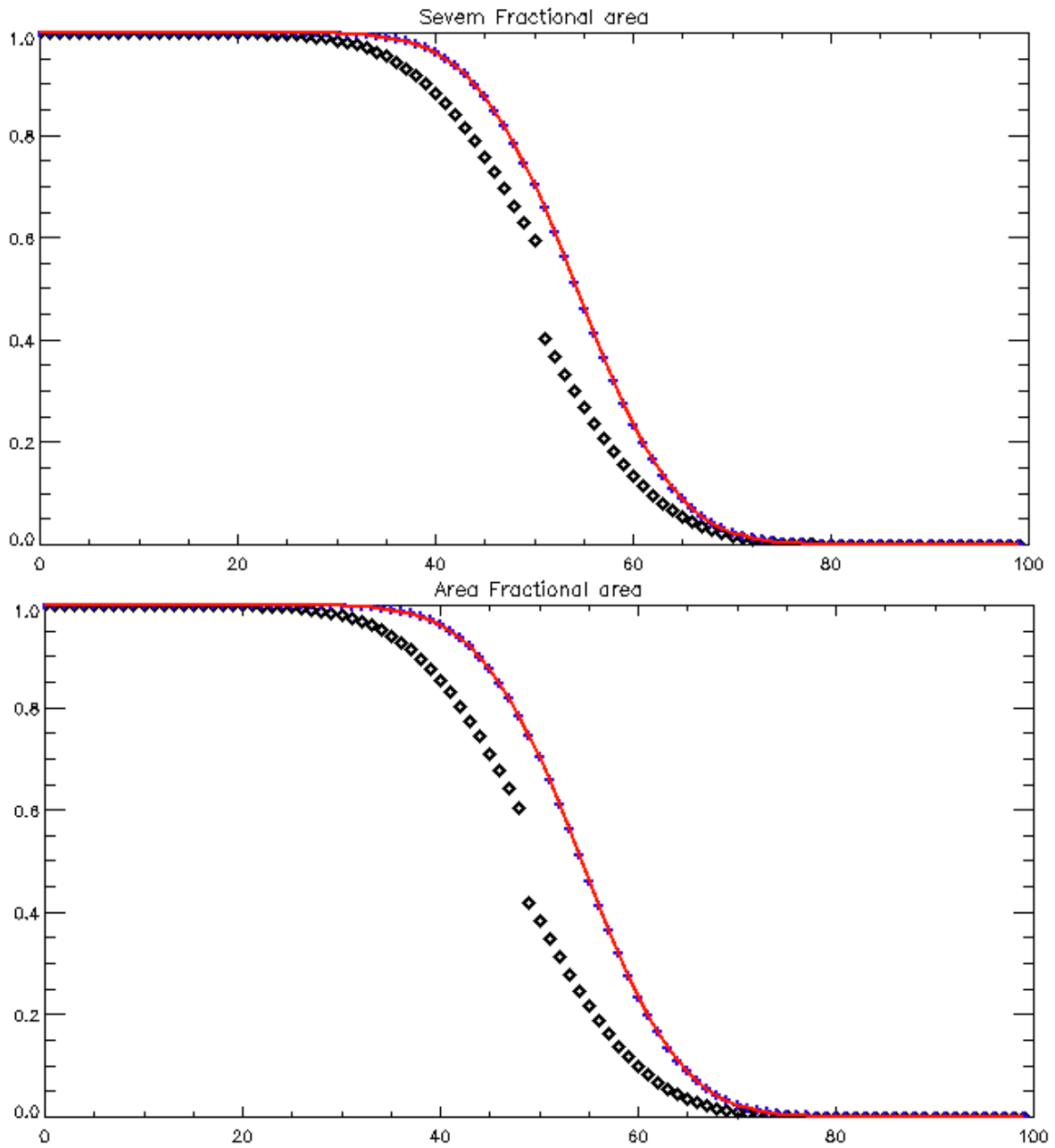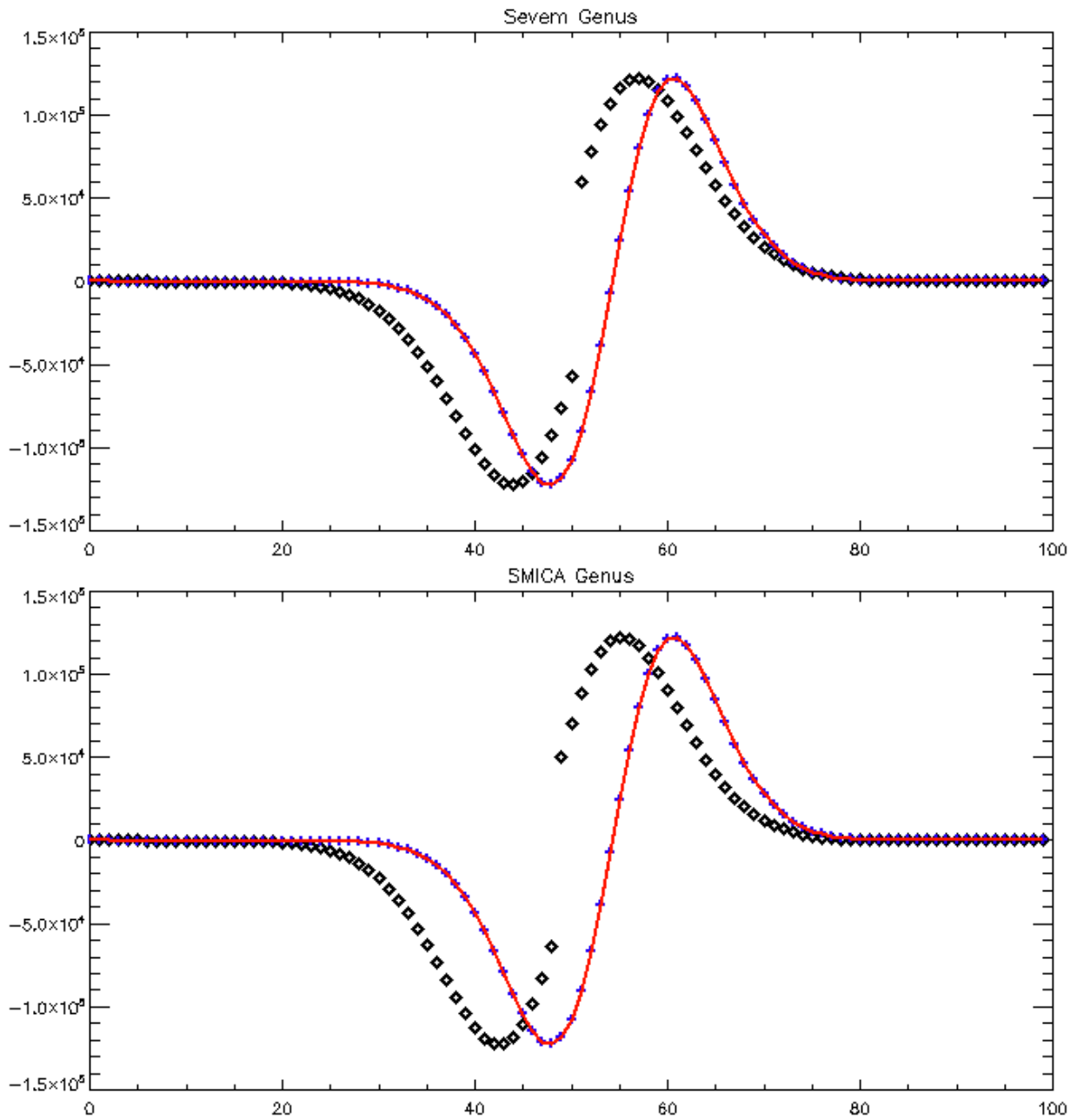
Figure 7.16: The Genus Minkowski Functional applied to the Planck's foreground-reduced maps (Sevem and SMICA). The Genus function, G, considers the difference between the number of hot spots and the number of cold spots in the map. The plot of the MF is represented by the diamonds. The Gaussian case is represented by the red solid line (simulated unlensed unmasked map) and by the plus signs (simulated lensed unmasked map).

8 CONCLUDING REMARKS

This work has presented a throughout review on the aspects surrounding the CMB and its NG. Our objective was to test the Gaussian condition of the most precise data, the Planck's 2015 data. Furthermore, we have applied two estimators to a series of four Planck maps and 12 ACT simulated maps (SEHGAL, 2009; Planck Collaboration, 2016a). Our results were then compared to a Gaussian case for analysis.

We could notice that both methods required a large portion of the sky, or full sky. Also, even after applying the mask, the inclusion of some residual contamination in the analysis was inevitable, not only foreground residuals but also instrumental systematics. These systematics were reduced from 2013 to the 2015 release, but not removed. Besides, the Planck team was not able to totally remove these residuals in the 2018 data (Planck Collaboration, 2018a). Therefore, our analysis has confirmed that there is indeed residual contamination in the Planck data because of the large deviations from the Gaussian case. That being said, the tools used do not allow us to fully investigate the physics involved, only the presence of deviations.

Therefore, the measurement of the primordial NG requires a better component separation algorithm in order to remove all foreground contamination. It is clear from our analysis that the residuals present in the data create large deviations from Gaussianity. And, as it was said before, large NG have been ruled out as primordial perturbations candidate (KOMATSU, 2009b). Then, it is possible that the Planck team has successfully improved their component separation algorithms in 2018 (Planck Collaboration, 2018e). The tests with the 2018 data are left for a future work.

Bibliography

ALI-HAÏMOUD, Y.; HIRATA, C. M.; DICKINSON, C. A refined model for spinning dust radiation. MNRAS, v. 395, p. 1055. [astro-ph/0812.2904], 2009.

ABRAMO, L. R.; PEREIRA, T. S. Testing gaussianity, homogeneity and isotropy with the cosmic microwave background. Advances in Astronomy, p. 52. [astro-ph/1002.3173], 2010.

BABICH, D.; CREMINELLI, P.; ZALDARRIAGA, M. The shape of non-Gaussianities. JCAP. 0408:009. [astro-ph/0405356], 2004.

BARDEEN, J. M. Gauge-invariant cosmological perturbations. Physical Review D, v. 22, i. 8, pp.1882-1905. 1980.

BARTOLO, N.; KOMATSU, E.; MATARRESE, S.; RIOTTO, A. Non-Gaussianity from inflation: theory and observations. Physics Reports, v. 402, p. 103–266. [astro-ph/0406398], 2004.

BARTOLO, N.; MATARRESE, S.; RIOTTO, A. Non-Gaussianity and the Cosmic Microwave Background Anisotropies. [astro-ph.CO/1001.3957], 2010.

BASAK, S; DELABROUILLE, J. A needlet internal linear combination analysis of WMAP 7-year data: estimation of CMB temperature map and power spectrum. MNRAS, v. 419, p. 1163, 2012.

BASAK, S; DELABROUILLE, J. A needlet ILC analysis of WMAP 9-year polarization data: CMB polarization power spectra. MNRAS, v. 435, p. 18, 2013.

BASSETT, B. A.; TSUJIKAWA, S.; WANDS, D. Inflation Dynamics and Reheating, [astro-ph/0507632]. 2006.

BAUMANN, D. TASI lectures on inflation. [hep-th/0907.5424], 2009.

BAUMANN, D. Cosmology. Part III Mathematical Tripos. [Amsterdam Cosmology group webpage. Available at: damtp.cam.ac.uk/user/db275/Cosmology/Lectures.pdf], 2012.

BAUMANN, D. Advanced Cosmology Lectures [Amsterdam Cosmology group webpage. Available at: cosmology.amsterdam/education/advanced-cosmology/], 2016.

BAUMANN, D. TASI lectures on Primordial Cosmology. [hep-th/1807.03098], 2018.

BENNETT, C. L.; BANDAY, A. J.; GORSKI, K. M.; HINSHAW, G.; JACKSON, P.; KEEGSTRA, P.; KOGUT, A.; SMOOT, G. F.; Wilkinson, D. T.; WRIGHT, E. L. Four-Year COBE DMR Cosmic Microwave Background Observations: Maps and Basic Results. Astrophysical Journal Letters, v.464, p.L1. [DOI:10.1086/310075], 1996.

BENNETT, C. L.; HILL, R. S.; HINSHAW, G.; NOLTA, M. R.; ODEGARD, N.; PAGE, L.; SPERGEL, D. N.; WEILAND, J. L.; WRIGHT, E. L.; HALPERN, M.; JAROSIK, N.; KOGUT,

A.; LIMON, M.; MEYER, S. S.; TUCKER, G. S.; WOLLACK, E. First-year Wilkinson Microwave Anisotropy Probe (WMAP) observations: foreground emission. Astrophysical Journal Supplement Series, v. 148, p. 97–117, 2003.

BENNETT, C. L.; LARSON, D.; WEILAND, J. L.; JAROSIK, N.; HINSHAW, G.; ODEGARD, N.; SMITH, K. M.; HILL, R. S.; GOLD, B.; HALPERN, M.; KOMATSU, E.; NOLTA, M. R.; PAGE, L.; SPERGEL, D. N.; WOLLACK, E.; DUNKLEY, J.; KOGUT, A.; LIMON, M.; MEYER, S. S.; TUCKER, G. S.; WRIGHT, E. L. Nine-year Wilkinson Microwave Anisotropy Probe (WMAP) observations: Final maps and results. Astrophysical Journal, Supplement, v. 208, p. 20. [astro-ph.CO/1212.5225], 2013.

BERNUI, A.; REBOUÇAS, M. J. Searching for non-Gaussianity in the WMAP data. Physical Review D: Particles, Fields, Gravitation & Cosmology, v. 79, n. 6, p. 063528. [astro-ph/0806.3758], 2009.

BERNUI, A.; REBOUÇAS, M. J. Non-gaussianity in the foreground-reduced CMB maps, Phys.Rev. D81. 063533. [astro-ph/0912.0269], 2010.

BERNUI, A.; REBOUÇAS, M. J. Mapping the large-angle deviation from Gaussianity in simulated CMB maps, Phys.Rev. D85. 023522. [astro-ph/1109.6086], 2012.

BERNUI, A.; OLIVEIRA, A. F.; PEREIRA, T. S. North-south non-gaussian asymmetry in planck CMB maps. Journal of Cosmology and Astroparticle Physics, v. 10, p. 41. [astro-ph.CO/1404.2936], 2014.

BERSANELLI, M.; MAINO, D.; MENNELLA, A. Anisotropies of the cosmic microwave background. Nuovo Cimento Rivista Serie, v. 25, n. 9, p. 1–82. [astro-ph/0209215], 2002.

CARDOSO, J-F.; MARTIN, M.; DELABROUILLE, J.; BETOULE, M.; PATANCHON, G. Component separation with flexible models. Application to the separation of astrophysical emissions. [astro-ph/0803.1814], 2008.

CARLSTROM, J. E.; Ade, P. A. R.; Aird, K. A.; Benson, B. A.; Bleem, L. E.; Busetti, S.; Chang, C. L.; Chauvin, E.; Cho, H.-M.; Crawford, T. M.; Crites, A. T.; Dobbs, M. A.; Halverson, N. W.; Heimsath, S.; Holzapfel, W. L.; Hrubes, J. D.; Joy, M.; Keisler, R.; Lanting, T. M.; Lee, A. T.; Leitch, E. M.; Leong, J.; Lu, W.; Lueker, M.; Luong-Van, D.; McMahon, J. J.; Mehl, J.; Meyer, S. S.; Mohr, J. J.; Montroy, T. E.; Padin, S.; Plagge, T.; Pryke, C.; Ruhl, J. E.; Schaffer, K. K.; Schwan, D.; Shirokoff, E.; Spieler, H. G.; Staniszewski, Z.; Stark, A. A.; Tucker, C.; Vanderlinde, K.; Vieira, J. D.; Williamson, R. The 10 Meter South Pole Telescope. The Astronomical Society of the Pacific, v. 123, p. 568-581. [DOI: 10.1086/659879] 2011.

CHEN, X. Primordial non-gaussianities from inflation models. Advances in Astronomy, v. 2010, p. 72. [astro-ph.CO/1002.1416], 2010.

COLES, P.; LUCCHIN, F. Cosmology: The origin and evolution of cosmic structure. England: Wiley-VCH. Second Edition, by Peter Coles, Francesco Lucchin, pp. 512. [ISBN 0-471-48909-3], 2002.

DAVIES, R. D.; WILKINSON, A. Synchrotron Emission from the Galaxy. [astro-ph/9804208], 1998.

DODELSON, S. Modern Cosmology. Amsterdam (Netherlands): Academic Press. [ISBN: 0-12-219141-2], 2003.

DRAINE, B. T.; LAZARIAN, A. Diffuse Galactic Emission from Spinning Dust Grains. The Astrophysical Journal, v. 494, p. L19–L22, [astro-ph/9710152], 1998.

DRAINE, B. T.; LAZARIAN, A. Eletric Dipole Radiation from Spinning Dust Grains. The Astrophysical Journal, v. 508, p. 157-179, [astro-ph/9802239]. 1998.

DRAINE, B. T. Physics of the Interstellar and Intergalactic Medium. Princeton University Press, [ISBN: 978-0-691-12214-4] 2011.

DUNKLEY, J.; Komatsu, E.; Nolta, M. R.; Spergel, D. N.; Larson, D.; Hinshaw, G.; Page, L.; Bennett, C. L.; Gold, B.; Jarosik, N.; Weiland, J. L.; Halpern, M.; Hill, R. S.; Kogut, A.; Limon, M.; Meyer, S. S.; Tucker, G. S.; Wollack, E.; Wright, E. L. The Astrophysical Journal Supplement, v. 180, i. 2, pp. 306-329. [astro-ph/0803.0586], 2008.

DURRER, R. The cosmic microwave background. Published by Cambridge University Press, Cambridge, UK, [ISBN 978-0-521-84704-9], 2008.

ERIKSEN, H. K.; NOVIKOV, D. I.; LILJE, P. B.; BANDAY, A. J.; GÓRSKI, K. M. Testing for non-Gaussianity in the Wilkinson Microwave Anisotropy Probe data: Minkowski functionals and the length of the skeleton. The Astrophysical Journal, v. 612, p. 64–80. [astro-ph/0401276], 2004.

ERIKSEN, H. K.; Jewell, J. B.; Dickinson, C.; Banday, A. J.; Górski, K. M.; Lawrence, C. R. Joint Bayesian Component Separation and CMB Power Spectrum Estimation. The Astrophysical Journal, v. 676, p. 10-32. [arxiv: 0709.1058], 2008.

FOWLER, J. W.; Niemack, M. D.; Dicker, S. R.; Aboobaker, A. M.; Ade, P. A. R.; Battistelli, E. S.; Devlin, M. J.; Fisher, R. P.; Halpern, M.; Hargrave, P. C.; Hincks, A. D.; Kaul, M.; Klein, J.; Lau, J. M.; Limon, M.; Marriage, T. A.; Mauskopf, P. D.; Page, L.; Staggs, S. T.; Swetz, D. S.; Switzer, E. R.; Thornton, R. J.; Tucker, C. E. Optical Design of the Atacama Cosmology Telescope and the Millimeter Bolometric Array Camera. Applied Optics, v. 46, p 17. [astro-ph/0701020] 2007

GAWISER, E.; SILK, J. The cosmic microwave background radiation. Physics Reports, v. 333, p. 245–267, ago. [astro-ph/0002044], 2000.

GÓRSKI, K. M.; HIVON, E.; BANDAY, A. J.; WANDELT, B. D.; HANSEN, F. K.; REINECKE, M.; BARTELMANN, M. Healpix: A framework for high-resolution discretization and fast analysis of data distributed on the sphere. The Astrophysical Journal, v. 622, p. 759–771. [astro-ph/0409513], 2005.

GUTH, A. H. Inflationary universe: A possible solution to the horizon and flatness problems.

Physical Review D, v. 23, p. 347–356, jan, 1981.

HINSHAW, G.; LARSON, D.; KOMATSU, E.; SPERGEL, D. N.; BENNETT, C. L.; DUNKLEY, J.; NOLTA, M. R.; HALPERN, M.; HILL, R. S.; ODEGARD, N.; PAGE, L.; SMITH, K. M.; WEILAND, J. L.; GOLD, B.; JAROSIK, N.; KOGUT, A.; LIMON, M.; MEYER, S. S.; TUCKER, G. S.; WOLLACK, E.; WRIGHT, E. L. Nine-Year Wilkinson Microwave Anisotropy Probe (WMAP) Observations: Cosmological Parameter Results. [arxiv: 1212.5226], 2013.

HU, W.; WHITE, M. Acoustic Signatures in the Cosmic Microwave Background. Astrophysics Journals. v. 471, p 30-51. [astro-ph/9602019], 1996.

HU, W.; SUGIYAMA, N.; SILK, J. The physics of microwave background anisotropies. Nature, v. 386, p. 37–43, mar.[astro-ph/9504057], 1997.

HU, W. Weak Lensing of the CMB: A Harmonic Approach. Phys. Rev. D62, 043007. [arxiv: 0001303], 2000.

HU, W.; DODELSON, S. Cosmic microwave background anisotropies. Annual Review of Astronomy & Astrophysics, v. 40, p. 171–216. [astro-ph/0110414], 2002a.

HU, W.; HEDMAN, M. M.; ZALDARRIAGA, M. Benchmark Parameters for CMB Polarization Experiments. Phys. Rev. D, v. 67. [astro-ph/0210096v1], 2002b.

HU, W. Lecture notes on CMB theory: From nucleosynthesis to recombination. [astro-ph/0802.3688], 2008.

ICHIKI, K. CMB foreground: A concise review. Prog. Theor. Exp. Phys., v. 06. [06B109], 2014.

KINNEY, W. H. TASI lectures on inflation. [astro-ph/0902.1529], 2009.

KOGUT, A.; DUNKLEY, J.; BENNETT, C. L.; DORÉ, O.; GOLD, B.; HALPERN, M.; HINSHAW, G.; JAROSIK, N.; KOMATSU, E.; NOLTA, M. R.; ODEGARD, N.; PAGE, L.; SPERGEL, D. N.; TUCKER, G. S.; WEILAND, J. L.; WOLLACK, E.; WRIGHT, E. L. Three-year Wilkinson Microwave Anisotropy Probe (WMAP) observations: Foreground polarization. The Astrophysical Journal, v. 665, p. 355–362, ago. [astro-ph/0704.3991], 2007.

KOLB, E. W.; TURNER, M. S. The early universe. New York: Addson-Wesley. Front. Phys., Vol. 69,, 1988.

KOMATSU, E.; SPERGEL, D. N. The cosmic microwave background bispectrum as a test of the physics of inflation and probe of the astrophysics of the low-redshift universe, [astro-ph/0012197]. 2000.

KOMATSU, E. The Pursuit of Non-Gaussian Fluctuations in the Cosmic Microwave Background. [astro-ph/0206039], 2002.

KOMATSU, E.; KOGUT, A.; NOLTA, M. R.; BENNETT, C. L.; HALPERN, M.; HINSHAW, G.; JAROSIK, N.; LIMON, M.; MEYER, S. S.; PAGE, L.; SPERGEL, D. N.;

TUCKER, G. S.; VERDE, L.; WOLLACK, E.; WRIGHT, E. L. First-year Wilkinson Microwave Anisotropy Probe (WMAP) observations: Tests of Gaussianity. The Astrophysical Journal Supplement Series, v. 148, p. 119–134. [astro-ph/0302223], 2003.

KOMATSU et al. Non-Gaussianity as a Probe of the Physics of the Primordial Universe and the Astrophysics of the Low Redshift Universe. [arxiv: 0902.4759] 2009a.

KOMATSU, E.; Dunkley, J.; Nolta, M. R.; Bennett, C. L.; Gold, B.; Hinshaw, G.; Jarosik, N.; Larson, D.; Limon, M.; Page, L.; Spergel, D. N.; Halpern, M.; Hill, R. S.; Kogut, A.; Meyer, S. S.; Tucker, G. S.; Weiland, J. L.; Wollack, E.; Wright, E. L. Five-Year Wilkinson Microwave Anisotropy Probe (WMAP) Observations: Cosmological Interpretation. The Astrophysical Journal Supplement, Volume 180, Issue 2, pp. 330-376. [arxiv: 0803.0547], 2009b.

LEACH, S. M.; Cardoso, J.-F.; Baccigalupi, C.; Barreiro, R. B.; Betoule, M.; Bobin, J.; Bonaldi, A.; Delabrouille, J.; de Zotti, G.; Dickinson, C.; Eriksen, H. K.; González-Nuevo, J.; Hansen, F. K.; Herranz, D.; Le Jeune, M.; López-Caniego, M.; Martínez-González, E.; Massardi, M.; Melin, J.-B.; Miville-Deschênes, M.-A.; Patanchon, G.; Prunet, S.; Ricciardi, S.; Salerno, E.; Sanz, J. L.; Starck, J.-L.; Stivoli, F.; Stolyarov, V.; Stompor, R.; Vielva, P. Component separation methods for the PLANCK mission. Astronomy and Astrophysics, v. 491, 2, pp.597-615. [DOI:10.1051/0004-6361:200810116], 2008.

LEITCH, E. M.; READHEAD, A. C. R. Anomalous Microwave Emission: Theory, Modeling, and Observations. Adv. Astro., v. 2013, p. 6. [DOI: 10.1155/2013/134979], 2013.

LESGOURGUES, J. TASI Lectures on Cosmological Perturbations. [arxov: 1302.4640], 2013

LIGUORI, M.; SEFUSATTI, E.; FERGUSSON, J. R.; SHELLARD, E.P.S. Primoridal non-Gaussianity and Bispectrum Measurements in the Cosmic Microwave Background and Large-Scale Structure. [arxiv: 1001.4707] 2010.

LIDDLE, A. R.; LYTH, D. H. Cosmological Inflation and Large-Scale Structure. Cambridge, United Kingdom: Cambridge University Press. [ISBN 052166022X], 2000.

LINDE, A. Particle Physics and Inflationary Cosmology. Contemp. Concepts Phys. v. 5, p. 1-362. [hep-th/0503203], 2005.

LINDE, A. Inflationary Cosmology. Lect. Notes Phys., v. 738, p. 1-54, [arxiv: 0705.0164], 2007.

LUE, A.; WANG, L.; KAMIONKOWSKI, M. Cosmological Signature of New Parity-Violating Interactions. Phys.Rev.Lett. v. 83, pp. 1506-1509. [astro-ph/9812088], 1999.

MACELLARI, N; PIERPAOLI, E; DICKINSON, C.; VAILLANCOURT, J. E. Galactic foreground contributions to the 5-year Wilkinson Microwave Anisotropy Probe maps. Monthly Notices of the Royal Astronomical Society. v, 418. i, 2. [DOI: 10.1111/j.1365-2966.2011.19542.x], 2011.

MACTAVISH, C. J.; ADE, P.A.; BOCK, J. J.; BOND, J. R.; BORRILL, J.; BOSCALERI, A.; CABELLA, P.; CONTALDI, C. R.; CRILL, B. P.; de BERNARDIS, P.; de GASPERIS, G.; de OLIVEIRA-COSTALL, A.; de TROIA, G.; di STEFANO, G.; HIVON, E.; JAFFE, A. H.; JONES, W. C.; KISNER, T. S.; LANGEL, A. E.; LEWIS, A. M.; MASIL, S.; MAUSKOPF, P.D.; MELCHIORRIL, A.; MONTROY, T. E.; NATOLI, P.; NETTERFIELD, C. B.; PASCALE, E.; PIACENTINI, F.; POGOSYAN, D.; POLENTA.; PRUNET, S.; RICCIARDI, S.; ROMEO, G.; RUHL, J. E.; SANTINI, P.; TEGMARK, M.; VENEZIANI, M.; VITTORIO, N. Cosmological Parameters from the 2003 Flight of BOOMERANG. The Astrophysical Society, v. 647, n. 2, [doi: 10.1086/505558] 2005

MATHER, J. C.; CHENG, E. S.; COTTINGHAM, D. A.; EPLEE, R. E., Jr.; FIXSEN, D. J.; HEWAGAMA, T.; ISAACMAN, R. B.; JENSEN, K. A.; MEYER, S. S.; NOERDLINGER, P. D.; READ, S. M.; ROSEN, L. P.; SHAFER, R. A.; WRIGHT, E. L.; BENNETT, C. L.; BOGGESS, N. W.; HAUSER, M. G.; KELSALL, T.; MOSELEY, S. H., Jr.; SILVERBERG, R. F.; SMOOT, G. F.; WEISS, R.; WILKINSON, D. T. Measurement of the cosmic microwave background spectrum by the COBE FIRAS instrument. Astrophys. J., 420, 439. [ISSN 0004-637X], 1994.

MEMARI, Y. Polarization of the Cosmic Microwave Background Radiation. Dissertation (Ph.D.), 2007.

MINKOWSKI, H. Volumen und oberfläche. Mathematische Annalen, v. 57, p. 447–495, 1903. Available at: <http://eudml.org/doc/158108>

NASA. The Planck Mission: Education and Public Outreach. [Caltech webpage], 2013.

NASA. Legacy Archive for Microwave Background Data Analysis (LAMBDA). [LAMBDA], 2018.

NOVAES, C. P.; BERNUI, A.; FERREIRA, I. S.; WUENSCHE, C. A. A neural-network based estimator to search for primordial non-Gaussianity in planck CMB maps. [astro-ph.CO/1409.3876], 2014a.

NOVAES, C. P.; Bernui, A.; Marques, G. A.; Ferreira, I. S. Local analyses of Planck maps with Minkowski Functionals. MNRAS, v. 461, i. 2, pp. 1363-1373. [arxiv: 1606.04075], 2014b.

NOVIKOV, D.; FELDMAN, H. A.; SHANDARIN, S. F. Minkowski functionals and cluster analysis for CMB maps. International Journal of Modern Physics D, v. 8, p. 291–306. [astro-ph/9809238], 1999.

NOVIKOV, D; SCHMALZING, J; MUKHANOV, V. M. On non-Gaussianity in the Cosmic Microwave Background. [astro-ph/0006097], 2000.

NOVIKOV, D; COLOMBI, S; DORE, O. Skeleton as a probe of the cosmic web the 2D case. Mon.Not.Roy.Astron.Soc. v. 366, p. 1201-1216. [astro-ph/0307003], 2006.

PENZIAS, A. A.; WILSON, R. W. Measurement of excess antenna temperature at 4080 mc/s. The Astrophysical Journal, p. 142–419. [DOI:10.1086/148307], 1965.

PETER P.; UZAN J.-P. Primordial Cosmology. Oxford University Press. [ISBN: 9780199665150], 2013.

Planck Collaboration. Planck early results. v. The Low Frequency Instrument data processing. A&A. v, 536. [DOI: 10.1051/0004-6361/201116484], 2011a.

Planck Collaboration. Planck early results. vi. The High Frequency Instrument data processing. A&A. v, 536. [DOI: 10.1051/0004-6361/201116462], 2011b.

Planck Collaboration. Planck early results. xix. All-sky temperature and dust optical depth from Planck and IRAS. Constraints on the "dark gas" in our Galaxy. A&A. v, 536. [doi: 10.1051/0004-6361/201116479], 2011.

Planck Collaboration. Planck 2013 results. i. overview of products and scientific results. Astronomy & Astrophysics, v. 571, p. A1. [arxiv: 1303.5062], 2013a.

Planck Collaboration. Planck 2013 Results. xxiv. Constraints on primordial non-Gaussianity. Astronomy & Astrophysics, v. 571, p. A1. [arxiv: 1303.5084], 2013b.

Planck Collaboration. Planck 2013 results. xxx. Cosmic infrared background measurements and implications for star formation. Astronomy & Astrophysics, v. 571, p. A1. [arxiv: 1309.0382], 2013c.

Planck Collaboration. Planck 2015 results. i. Overview of products and scientific results. Astronomy & Astrophysics. [arxiv: 1502.01582], 2015a.

Planck Collaboration. Planck 2015 results. iii. LFI systematic uncertainties. Astronomy & Astrophysics. [arxiv: 1507.08853], 2015b.

Planck Collaboration. Planck 2015 results. ix. Diffuse component separation: CMB maps. Astronomy & Astrophysics, v. 594. [arxiv: 1502.05956], 2015c.

Planck Collaboration. Planck 2015 results. x. Diffuse component separation: Foreground maps. Astronomy & Astrophysics, v. 594. [arxiv: 1502.01588], 2016a.

Planck Collaboration. Planck 2015 results. xvi. Isotropy and statistics of the CMB. Astronomy & Astrophysics, v. 594. [astro-ph/1506.07135], 2016f.

Planck Collaboration. Planck 2015 results. xvii. Constraints on primordial non-Gaussianity. Astronomy & Astrophysics, v. 594. [arxiv: 1502.01592], 2016b.

Planck Collaboration. Planck 2015 results. xx. Constrains on Inflation. [arxiv: 1502.02114], 2016c.

Planck Collaboration. Planck 2015 results. xxv. Diffuse Low-Frequency Galactic Foreground. Astronomy & Astrophysics, v. 594, A25. [arxiv: 1506.06660] 2016d.

Planck Collaboration. Planck intermediate results. XLIX. Parity-violation constraints from polarization data. [arxiv: 1605.08633] 2016e

Planck Collaboration. Planck 2018 results i. Overview, and the cosmological legacy of

Planck. [arxiv: 1807.06205], 2018a.

Planck Collaboration. Planck 2018 results. iv. Diffuse component separation. [arxiv: 1807.06208], 2018e.

Planck Collaboration. Planck 2018 results vi. Cosmological Parameters. [arvix: 1807.06209], 2018b.

Planck Collaboration. Planck 2018 results x. Constrains on inflation. [arxiv: 1807.06211], 2018c.

Planck Collaboration. Planck 2018 results. xii. Galactic astrophysics using polarized dust emission. [arxiv: 1807.06212], 2018d.

Planck Collaboration. Planck pre-launch status. Planck Mission. Astronomy & Astrophysics 520, A1 [DOI: 10.1051/0004-6361/200912983], 2009.

PLANCK MISSION. ESA webpage, 2018.

PLANCK MISSION. NASA webpage, 2018.

REICHARDT, L. C; ADE, A. R. P; BOCK, J. J; BOND, R. J; BREVIK, A. J; CONTALDI, R. C; DAUB, D. M; DEMPSEY, T. J; GOLDSTEIN, H. J; HOLZAPFEL, L. W; KUO, L. C; LANGE, E. A; LUEKER, M; NEWCOMB, M; PETERSON, B. J; RUHL, J; RUNYAN, C. M; STANISZEWSKI, Z. High resolution CMB power spectrum from the complete ACBAR data set. [arxiv: 0801.1491], 2009.

RIOTTO, A. Inflation and the theory of cosmological perturbations. [hep-ph/0210162], 2002.

RYBICKI, G. B.; LIGHTMAN, A. P. Radiative processes in astrophysics. Wiley-VCH. [ISBN 0-471-82759-2], 1985.

SACHS, R. K.; WOLFE, A. M. Perturbations of a cosmological model and angular variations of the microwave background. The Astrophysical Journal, v. 147, p. 73, jan. [DOI:10.1086/148982], 1967.

SEHGAL, N.; Bode, P.; Das, S.; Hernandez-Monteagudo, C.; Huffenberger, K.; Lin, Y.; Ostriker, J. P.; Trac, H. The Astrophysical Journal, v. 709, i. 2, pp. 920-936. [astro-ph/0908.0540], 2009.

SIEVERS, J. L.; HLOZEK, R. A.; NOLTA, M. R.; ACQUAVIVA, V.; ADDISON, G. E.; ADE, P. A. R.; AGUIRRE, P.; AMIRI, M.; APPEL, J. W.; BARRIENTOS, L. F.; BATTISTELLI, E. S.; BATTAGLIA, N.; BOND, J. R.; BROWN, B.; BURGER, B.; CALABRESE, E.; CHERVENAK, J.; CRICHTON, D.; DAS, S.; DEVLIN, M. J.; DICKER, S. R.; DORIESE, W. B.; DUNKLEY, J.; DÜNNER, R.; ESSINGER-HILEMAN, T.; FABER, D.; FISHER, R. P.; FOWLER, J. W.; GALLARDO, P.; GORDON, M. S.; GRALLA, M. B.; HAJIAN, A.; HALPERN, M.; HASSELFIELD, M.; HERNÁNDEZ-MONTEAGUDO, C.; HILL, J. C.; HILTON, G. C.; HILTON, M.; HINCKS, A. D.; HOLTZ, D.; HUFFENBERGER, K. M.; HUGHES, D. H.; HUGHES, J. P.; INFANTE, L.; IRWIN, K. D.; JACOBSON, D. R.;

JOHNSTONE, B.; JUIN, J. B.; KAUL, M.; KLEIN, J.; KOSOWSKY, A.; LAU, J. M.; LIMON, M.; LIN, Y.-T.; LOUIS, T.; LUPTON, R. H.; MARRIAGE, T. A.; MARSDEN, D.; MARTOCCI, K.; MAUSKOPF, P.; MCLAREN, M.; MENANTEAU, F.; MOODLEY, K.; MOSELEY, H.; NETTERFIELD, C. B.; NIEMACK, M. D.; PAGE, L. A.; PAGE, W. A.; PARKER, L.; PARTRIDGE, B.; PLIMPTON, R.; QUINTANA, H.; REESE, E. D.; REID, B.; ROJAS, F.; SEHGAL, N.; SHERWIN, B. D.; SCHMITT, B. L.; SPERGEL, D. N.; STAGGS, S. T.; STRYZAK, O.; SWETZ, D. S.; SWITZER, E. R.; THORNTON, R.; TRAC, H.; TUCKER, C.; UEHARA, M.; VISNJIC, K.; WARNE, R.; WILSON, G.; WOLLACK, E.; ZHAO, Y.; ZUNCKEL, C. The Atacama Cosmology Telescope: Cosmological parameters from three seasons of data. [arxiv: 1301.0824], 2013.

SILK, J. Cosmic Black-Body Radiation and Galaxy Formation. Astrophysical Journal, vol. 151, p.459. [DOI 10.1086/149449], 1968.

SMOOT, G. F.; BENNETT, C. L.; KOGUT, A.; WRIGHT, E. L.; AYMON, J.; BOGGESS, N. W.; CHENG, E. S.; AMICI, G. de; GULKIS, S.; HAUSER, M. G.; HINSHAW, G.; JACKSON, P. D.; JANSSEN, M.; KAITA, E.; KELSALL, T.; KEEGSTRA, P.; LINEWEAVER, C.; LOEWENSTEIN, K.; LUBIN, P.; MATHER, J.; MEYER, S. S.; MOSELEY, S. H.; MURDOCK, T.; ROKKE, L.; SILVERBERG, R. F.; TENORIO, L.; WEISS, R.; WILKINSON, D. T. COBE differential microwave radiometers: instrument design and implementation. The Astrophsyical Journal, p. S360–685. [DOI:10.1086/169154], 1990.

SMOOT, G. F.; BENNETT, C. L.; KOGUT, A.; WRIGHT, E. L.; AYMON, J.; BOGGESS, N. W.; CHENG, E. S.; AMICI, G. de; GULKIS, S.; HAUSER, M. G.; HINSHAW, G.; JACKSON, P. D.; JANSSEN, M.; KAITA, E.; KELSALL, T.; KEEGSTRA, P.; LINEWEAVER, C.; LOEWENSTEIN, K.; LUBIN, P.; MATHER, J.; MEYER, S. S.; MOSELEY, S. H.; MURDOCK, T.; ROKKE, L.; SILVERBERG, R. F.; TENORIO, L.; WEISS, R.; WILKINSON, D. T. Structure in the COBE differential microwave radiometer first-year maps. [DOI:10.1086/186504] 1992

SMOOT, G. F. The cosmic microwave background spectrum. [astro-ph/9705101], 1997.

STRUKOV, I. A.; SKULACHEV, D. P. Deep-space measurements of the microwave background anisotropy - first results of the relikt experiment. Soviet Astronomy Letters, vol. 10 p. 1-4, 1984.

SU, M.; YADAV, A. P.S.; SHIMON, M.; KEATING, B. G. Impact of intrumental Systematics on the CMB Bispectrum. [arxiv: 1010.1957], 2010.

TELLO, C.; Villela, T.; Torres, S.; Bersanelli, M.; Smoot, G. F.; Ferreira, I. S.; Cingoz, A.; Lamb, J.; Barbosa, D.; Perez-Becker, D.; Ricciardi, S.; Currivan, J. A.; Platania, P.; Maino, D.. The 2.3 GHz continuum survey of the GEM project. A & A, v. 556. [arxiv: 0712.3141], 2013.

TRISTRAM, M.; GANGA, K. Data analysis methods for the cosmic microwave background. Reports on Progress in Physics, v. 70, p. 899–946. [arxiv: 0708.1429], 2007.

TRODDEN, M.; CARROLL, S. M. TASI Lectures: Introduction to Cosmology.

[astro-ph/0401547], 2004.

TUCKER, R. S. Characterization of Detectors and Instrument Systematics for the SPIDER CMB Polarimeter. Dissertation (Ph.D.), California Institute of Technology. 2014.

YADAV, A. P. S.; WANDELT, B. D. Primordial Non-Gaussianity in the Cosmic Microwave Background. Advances in Astronomy, v. 2010, p. 27, [arxiv: 1006.0275]. 2010.

ZALDARRIAGA, M. Fluctuations in the Cosmic Microwave Background. [astro-ph/9806122], 1998.